![LUT University logo]

THE DISSIMILAR WELD BETWEEN CAST STEEL AND UHSS, AND LOCAL GEOMETRY OPTIMIZATION OF THE WELD DETAIL

ABSTRACT

Lappeenranta–Lahti University of Technology LUT
LUT School of Energy Systems
Mechanical Engineering

Juho Havia

The dissimilar weld between cast steel and UHSS, and local geometry optimization of the weld detail

Master's thesis

2023

81 pages, 46 figures, 16 tables and 12 appendices

Examiners: Professor Timo Björk
            Matti Randelin, M.Sc. (Tech.)

Keywords: UHSS, cast steel, welded dissimilar joints, fatigue

In recent years, the use of ultra-high-strength structural steels has been studied much and by utilizing these steels effectively, energy can be saved, and thus emissions, but only fossil-free steel can lead into an emission-free future. It has been found that by using UHSS, significantly lighter structures can be made, without compromising load-bearing capacity or safety. However, it has been found that UHSSs are generally more sensitive to manufacturing parameters and the production quality must be good in order to fully utilize the properties of the steels (Skriko, 2018, pp. 116–121).

However, the dissimilar weld between cast steels and UHSS has not been scientifically studied, even though there are large differences in the requirements of the materials for a successful weld, e.g. the limits of heat input. Also, the welded joint with permanent root backing and the effect of the initial defect caused by it on the fatigue strength of UHSS steels has not been investigated.

In this thesis, the quality of the welded joint in the previously mentioned dissimilar joint and the effect of the initial defect of the weld root equipped with a permanent root backing on the fatigue strength of UHSS are investigated with an experimental study. In the welding of the dissimilar joint, the importance of the quality required from the process used was observed and compromises must be made at the expense of the mechanical properties of the materials in order to make the welding successful. In addition, the results showed a better fatigue strength for the investigated welded detail than the current design guidelines recommend.

TIIVISTELMÄ

Lappeenrannan–Lahden teknillinen yliopisto LUT
LUT-Energiajärjestelmät
Konetekniikka

Juho Havia

Eripari hitsausliitos valuteräksen ja UHSS välillä, ja paikallisen geometrian optimointi hitsaus detaljissa.

Diplomityö

2023

81 sivua, 46 kuvaa, 16 taulukkoa ja 12 liitettä

Tarkastajat: Professori Timo Björk
　　　　　　DI Matti Randelin

Avainsanat: UHSS, valuteräs, hitsatut eripariliitokset, väsyminen

Viime vuosina ultralujien rakenneteräksien käyttöä on tutkittu paljon ja hyödyntämällä näitä teräksiä tehokkaasti energiaa voidaan säästää, ja siten päästöjäkin, mutta vasta fossiilivapaasti valmistetulla teräksellä päästään kohti päästöttömyyttä. On havaittu, että käyttämällä UHSS teräksiä, voidaan tehdä huomattavasti kevyempiä rakenteita, kuormankantokyvystä tai turvallisuudesta tinkimättä. On kuitenkin havaittu, että UHSS teräkset ovat yleisesti herkempiä valmistusparametreille ja tuotanto laadun on oltava hyvä, jotta teräksien ominaisuuksia voidaan hyödyntää (Skriko, 2018, pp. 116–121).

Valuteräksien ja UHSS teräksien eripariliitosta ei kuitenkaan ole tieteellisesti tutkittu, vaikka materiaalien vaatimuksissa onnistuneelle hitsille on suuria eroja mm. lämmöntuonnin rajoissa. Myös hitsausliitos kiinteällä juurituella ja sen aiheuttaman alkuvian vaikutus UHSS teräksien väsymiskestävyyteen on jäänyt tutkimatta.

Tässä työssä tutkitaan hitsaus liitoksen laatua edellä mainitussa eripariliitoksessa ja kiinteällä juurituella varustellun hitsin juuren alkuvian vaikutusta UHSS teräksen väsymiskestävyyteen kokeellisella tutkimuksella. Eripariliitoksen hitsauksessa havaittiin prosessilta vaaditun laadun tärkeys ja kompromisseja on tehtävä materiaalien mekaanisten ominaisuuksien kustannuksilla, jotta hitsaus saadaan onnistumaan. Lisäksi tuloksista havaittiin tutkitulle hitsausdetaljille parempi väsymiskestävyys, kuin nykyiset suunnitteluohjeet suosittelevat.

ACKNOWLEDGEMENTS

SYMBOLS AND ABBREVIATIONS

Latin alphabet

A	Percentage elongation after fracture	[%]
A_g	Percentage non-proportional elongation at maximum force	[%]
a_i	Initial crack size	[mm]
a_f	Final or critical crack size	[mm]
C	The crack propagation coefficient	[mm/cycle]
CE_{IIW}	Carbon equivalent according to IIW	-
CET	Carbon equivalent according to Thyssen	-
d	Distance	[mm]
e	Eccentricity of the joint	[mm]
F	Force	[N]
F_2	Shape factor for heat flow in calculation $t_{8/5}$ 2D case	[-]
F_3	Shape factor for heat flow in calculation $t_{8/5}$ 3D case	[-]
FAT	Fatigue class, fatigue strength corresponding to $2 \cdot 10^6$ cycles	[MPa]
f_u	Tensile strength	[MPa]
f_y	Yield strength	[MPa]
$\Delta K(a)$	SIF range as function of the crack length	[MPa√mm]
h	Height	[mm]
I	Current	[A]
KV	Impact strength	[J]
K_f	Fatigue stress concentration factor	-
K_s	Structural stress concentration factor	-
K_t	Elastic notch stress concentration factor	-
k	Thermal efficiency of the welding process	-
m	Slope of S-N curve	-
m_p	Slope of Paris' law	-
Q	Heat input	[kJ/mm]
N_f	Fatigue life estimation	-
R	Stress ratio	-
r	Radius	[mm]
T_0	Initial temperature	[°C]

$t_{8/5}$	The cooling time from 800°C to 500°C	[s]
t	Material thickness	[mm]
U	Voltage	[V]
v	Welding speed	[mm/s]
v_{wire}	Wire feed speed	[m/min]
w	Width	[mm]

Greek alphabet

ρ_f	Fictitious notch radius	[mm]
σ	Stress	[MPa]
σ_f	Fatigue strength	[MPa]
σ_k	Maximum notch stress	[MPa]
σ_s	Structural stress	[MPa]

Abbreviations

AW	As welded
CO_2e	Carbon dioxide equivalent
CE	Equivalent carbon content
DIC	Digital image correlation
DOB	Degree of bending
DQ	Direct quenched
DQ+T	Direct quenched and tempered
EDS	Energy-dispersive X-ray spectroscopy
ENS	Effective notch stress
FEM	Finite element method
FF(U)HSS	Fossil-free (ultra)-high-strength steel
GMAW	Gas metal arc welding process
HAZ	Heat affected zone
HFMI	High-frequency impact treatment
LEFM	Linear elastic fracture mechanics
QT	Quenched and tempered
N	Normalized
SCF	Stress concentration factor

SEM	Scanning Electron microscope
SIF	Stress intensity factor
TMCP	Thermo-mechanical control process
UHSS	Ultra-high-strength steel
WPS	Welding procedure specification

Indices

avg	Average
b	Bending
m	Membrane
n	Notch
nom	Nominal

Table of contents

1 Introduction

This thesis was made for Hiab, part of Cargotec Corporation, as part of the Fossil-free Steel Application project, which aims to the commercialization of a fossil-free (ultra)-high-strength steels (FF(U)HSS). A carbon-neutral world is a mega trend to which several communities and individual countries have committed themselves. These new FF(U)HSSs could be one path that helps to achieve these carbon-free objectives. However, fossil-free steel, that reduces steel production emissions, is not enough alone and steel structures must also be more energy efficient, safe and the lifetime of the structures should be accurately estimated. This means that new structural solutions are needed, and many old products must be redesigned to use the material more efficiently and utilization of stronger grade steels are necessarily needed to achieve these goals and at the same time stay competitive. (Björk, 2022.)

The topic of this thesis was chosen from Hiab's Multilift product line to study fatigue in the welds in the steel structure of the Multilift hooklift. Steel structure of the hooklift has remained almost unchanged since 2006 and fierce competition and new environmental standards encourages the development of an efficient structure and the use of modern metallic materials. This thesis focuses on fatigue in welded dissimilar joints, when thick plates in the original steel structure are replaced with a significantly thinner ultra-high-strength steel (UHSS) plates, that still have the same load carrying capacity.

In the initial settings of the study, it was assumed that an unwelded initial crack remains on top of the permanent root backing at the weld root. This work studies whether the fatigue strength of the weld root can be improved with numerically calculated geometrical modification and what the fatigue strength of permanent root backing in single-bevel groove weld between cast steel and UHSS. In addition, welding of the dissimilar joint will be briefly investigated with a few different UHSS grades and two different cast steels.

1.1 Background of the thesis

In recent years, the UHSS has gained popularity in many applications. Usually, the UHSS definition refers steels that have minimum 690 MPa nominal yield strength (Amraei et al., 2020, p. 1). What makes these steels so attractive, is their high strength/weight ratio. This mechanical property makes possible to design lighter structures, enables the use of new types of efficient structure designs and decreases use of the steel overall. This is especially emphasized in mobile structures, such as automotive industry, because lighter structure decreases energy consumption, allows more payload and can increase crashworthiness of the structure. (Amraei et al., 2016, p. 227.) In Figure 1 can be seen possible weight savings when conventional structural steel plate is changed into higher-strength steel plate. In the bending beams, the weight saving may be even greater.
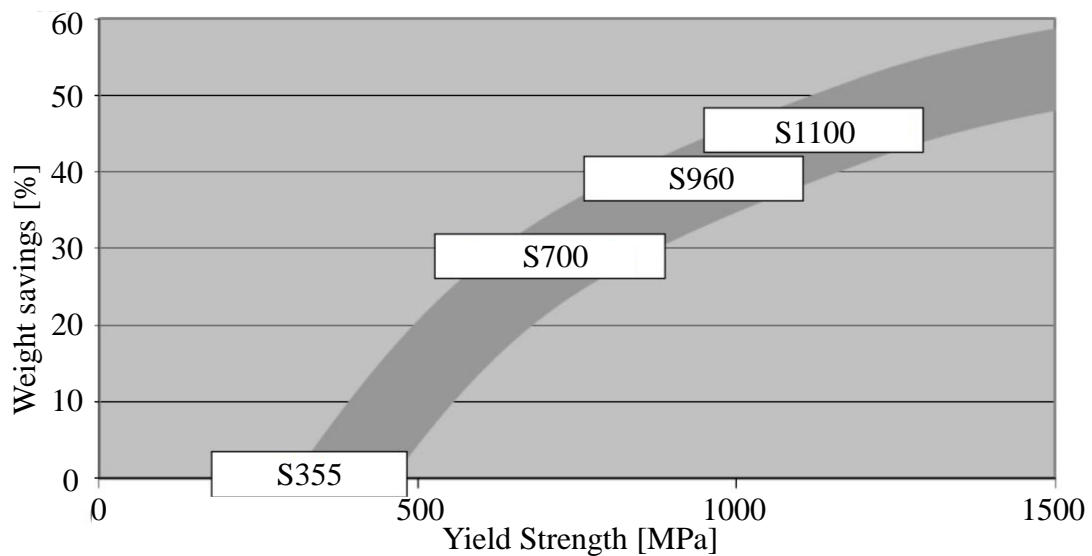
Figure 1. Possible weight savings by using structural steel plates with a higher nominal yield strength (Mod. Mikkonen et al., 2017, p. 27).

Another point of view, that drives into higher use UHSS is environmental aspects and carbon-neutrality. Producing 1 kg of traditional mild structural steel produces the emissions of about 2 kg of carbon dioxide equivalent (CO_2e) (Sperle, 2012, p. 3). In individual and modern production facilities, CO2e may be low as 1.6-1.7 kg per 1 kg of steel. CO2e emissions may also increase slightly when the nominal yield strength of the steel is increased, depending on the manufacturing method. However, the benefits of the reduction

in the required amount of steel in the structures and reduced lifetime emissions outweigh the possible small additional environmental impact of stronger steel. (Sperle, 2012, p. 10.) A new fossil-free steel production methods for iron reduction virtually eliminates carbon dioxide emissions in steelmaking. One of the many methods is an iron reduction process is called as HYBRIT process and on this process a traditional coal and coke are replaced with hydrogen and fossil-free electricity. Even though new fossil-free steels are produced, used processes after iron reduction remain the same than before, and only difference is that all used electricity and other fuels are fossil-free. This guarantees that the quality and properties of fossil-free steels will not change, and the properties can also be improved in the future. (SSAB, 2022, p. 15.)

There has been a known lack of knowledge, about UHSS. But in recent years there have been an increasing number of publications that have studied UHSS. The trend of published articles, conference papers and books, which deal with UHSS, has been growing and total amount of publications are 1907 between the years, 2000-2022. This analysis was made with Scopus and documents published per year can be seen in Figure 2. (Scopus, 2023.)
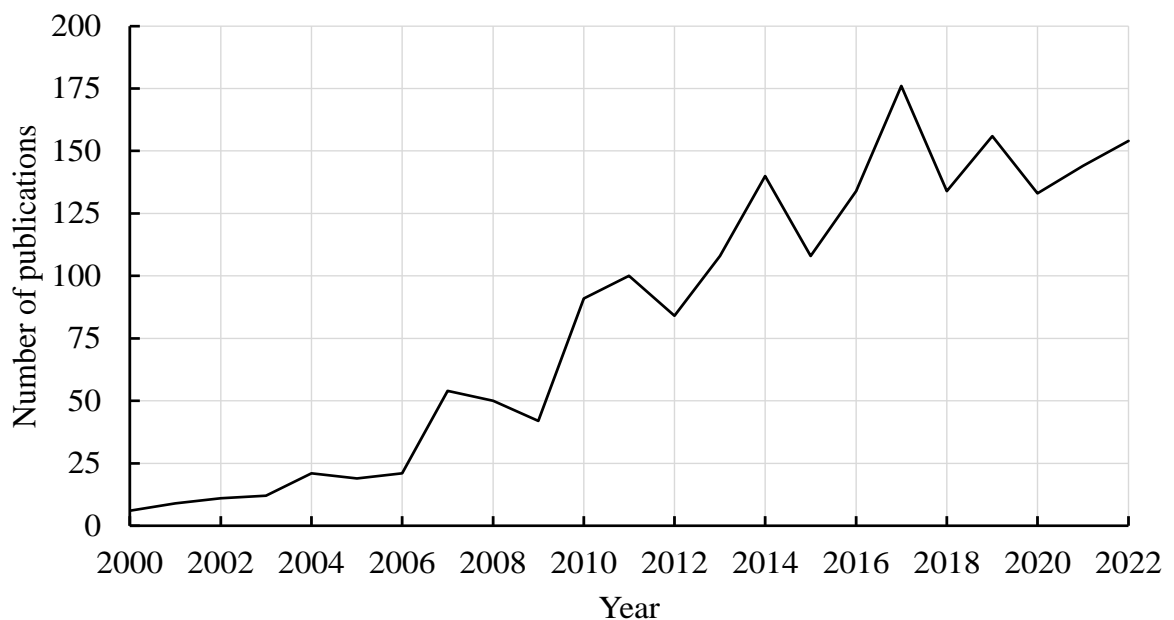
Figure 2. The amount of published articles, conference papers and books per year, that are related to search sentence "Ultra-high-strength steel" (Scopus, 2023).

UHSS materials have gradually become familiar with each scientific publication, but in many real-life applications there is a need to combine UHSS with different materials and

parts. For example, in many structures, cast steel is used in structural parts, connection points and joints in booms. Currently, there is very little if at all research on the UHSS and cast steel welding joint.

2 Welding of UHSS

Until now, all the welds in the researched structure have been manually welded with a gas metal arc welding (GMAW) process and used structural steels were between S355 and S550 grades. A brief literature review was conducted where was examined how changing the structural steel grade to UHSS affects welding and what things needs to be considered.

Many studies have shown that good structural design and manufacturing quality are required at every stage of production, to effectively utilize the potential capacity of UHSS. Although this thesis focuses on welding, other stages of manufacturing must also be considered in the actual steel structure, which could be e.g., cold forming, cutting and possible coatings. (Afkhami et al., 2019, p. 97; Lipiäinen et al., 2022, pp. 67–74; Skriko, 2018, pp. 119–121.)

Modern ultra-high-strength structural steels are mainly low-carbon micro-alloyed steels. The strength of these steels is based on fine grain structure, which is made with a thermo-mechanical controlled processing (TMCP) combined with optimal alloying and direct quenching (DQ) or traditional quenching and tempering (QT) process. Some steels grades are tempered after direct quenching (DQ+T). It has been observed that the used hardening method influences how welding affects the mechanical properties of UHSS, but the matter has not been investigated in more detail. The reason may be the higher alloying degree of QT steels.

The most common difficulties in welding of UHSSs are caused by heat management during the welding procedure and the effects are commonly manifested as the deterioration of material properties or as the occurrence of cold cracking. Deterioration of material properties depends a lot on the steel production method (DQ or QT), but in general the following phenomena can be identified: a softened region in the heat-affected zone (HAZ), reduced impact toughness, lack of ductility and reduced yielding and tensile strength. However, it is usually possible to reduce the aforementioned phenomena by adjusting parameters that affect the cooling rate of the weld or by using a welding process that is more suitable for the situation. (Afkhami et al., 2019, pp. 86–87; Skriko, 2018, p. 109.)

2.1 Cold cracking

The hardness of the HAZ is directly related to the hydrogen or cold cracking phenomenon because the hydrogen induced crack requires a simultaneous presence of the three primary factors that are stress, hydrogen and microstructural factors.

The stress factor is caused by an external load or a multiaxial tensile residual stress due the shrinkage of the weld, which occurs when the weld cools down. The hydrogen factor consists of hydrogen that is diffused into the weld and residual hydrogen that is trapped in the weld. The microstructure factor is hard and brittle microstructures, such as martensite whose hardness is determined by the alloying elements and especially the amount of carbon, with weak deformation ability, which are formed as a result of rapid cooling.

Risk of hydrogen cracking is eliminated when one of the three factors is removed and the most common methods used to control hydrogen cracking are the use of low-hydrogen consumables, an elevated welding temperature and post-weld heat treatments. Purpose of low-hydrogen content consumables is to directly reduce the amount of hydrogen in the weld. Use of the elevated welding temperature increases cooling time from 800°C to 500°C ($t_{8/5}$), which impedes the formation of hard microstructures such as martensite and gives additional time for the hydrogen to leave the weld. Post weld heat treatment or hydrogen release treatments can be performed right after welding to release hydrogen from weld and/or relief residual stresses from weld. (Lukkari et al., 2016, pp. 7–21.)

2.2 Deterioration of the material properties

The deterioration of the material properties in the HAZ are related to changes in the microstructure caused by the heat input of the welding process. The severity of the microstructural changes depends on the steel production method, chemical composition, microstructure and amount of heat input. (Javidan et al., 2016, pp. 16–17.)

In recent years, the properties of S700, S960 and S1100 UHSS have been studied a lot, and in all of them, a softened region through-thickness in the HAZ has been observed to varying degrees on both DQ and QT steels. However, the hardness of the microstructure does not directly correlate with the strength of the material, as only S960 has been observed to have a significant decrease in yield and tensile strength values. (Amraei et al., 2019, p. 12; Guo et al., 2017, p. 14.) The elongation before failure, compared to the base material, has also been found to decrease significantly in the HAZ region. The explanation for the phenomenon is a non-homogeneous microstructure in the HAZ, where strains are concentrated locally during tension, causing premature fracture compared to the uniform elongation that occurs in the base material (Guo et al., 2017, pp. 8–9; Tümer et al., 2022, p. 211). It has been recognized, that welding heat input in relation to geometry has major impact on the extent of the softened region in the HAZ, which also affects the elongation capacity of the weld prior to failure (Skriko, 2018, p. 109).

A decrease in impact toughness and ductility, compared to the base material, has been observed in welded UHSS joints, both in the weld metal and in the HAZ. This happens especially in QT steels due to the higher amount of alloying elements than in DQ steels. The location of the greatest decrease in impact toughness has been observed to be in the HAZ close to the fusion line and in the weld metal. The mechanism for the decrease in impact toughness is the rapid cooling which promotes the formation of the unfavourable microstructures such as coarse-grained partially untempered martensite. These unfavourable microstructures are generally very hard and brittle which poorly absorb impact energy, but the impact toughness is also lower in the softened HAZ region than in the base material due to the increased grain size. (Guo et al., 2017, p. 12; Tümer et al., 2022, pp. 212–213.)

Based on the aforementioned phenomena, it has been observed that the heat input window is much narrower in the welding of UHSS. Both excessive and very low heat inputs cause deterioration of material properties, depending on steel type. This has increased interest in low heat input welding processes, such as beam welding processes, for UHSS applications. The biggest advantages of beam welding processes are high energy density, narrow HAZ and much lower total heat input compared to arc welding processes. Figure 3 shows the welded cross-sections of an 8 mm thick UHSS plate using an electron beam, laser, laser-

GMAW hybrid and traditional GMAW welding processes, where the differences in the width of the HAZ are very noticeable. (Tümer et al., 2022, pp. 206–208.)
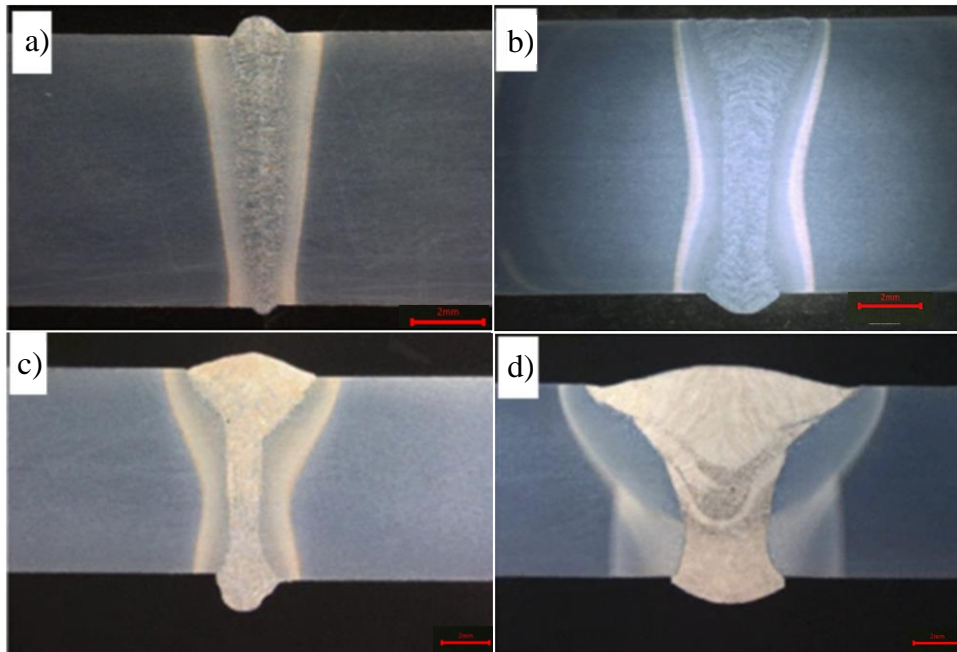

Figure 3. Cross sections of welds in the UHSS with different welding processes, a) Electron beam welding, b) laser welding, c) laser-GMAW hybrid and d) GMAW (Mod. Tümer et al., 2022, p. 208).

According to studies, the softened region in the HAZ cannot be avoided, but its width can be reduced with low heat input and/or using low heat input welding process such as a laser or laser-GMAW hybrid process. In DQ, the low heat input usually does not cause the formation of hard microstructures due to the low degree of alloying, in which case impact toughness is not an issue. Because of this, laser welding has been found to be very suitable for DQ steels. However, in QT steels a very low heat input is a compromise, because it causes cooling time to be very short, which regardless of the welding process causes poor impact toughness. (Guo et al., 2017, pp. 11–12; Skriko, 2018, pp. 109–111; Tümer et al., 2022, pp. 206–224.) The use of an under matching consumables has been found to significantly increase the impact toughness and ductility of the welded joint (Siltanen et al., 2016, p. 6).

The fatigue phenomenon in the UHSS welds has been examined separately in the butt welds and in the load-bearing longitudinal welds. The fatigue strength of the butt-welded joints

with different welding processes has been reported to be close IIW-recommendation FAT100 ($m = 3$), based on structural hot spot stress, although the fatigue resistance of the laser welded joints was slightly higher than with other welding processes. (Skriko, 2018, p. 112) Different opinions have also been published about the fatigue resistance of the butt joints welded with the GMAW process. Fatigue strength value FAT300 ($m = 5$) has been proposed for the GMAW butt joint, but reason for the superior fatigue strength has not been explained. For other welding processes, there were no differing opinions about fatigue strength. (Steimbreger et al., 2022, p. 20.) For longitudinal load carrying welds characteristic design curve FAT140 ($m = 3$) is proposed for both single- and double-sided welds with partial penetration, but the requirement is automated welding process and the starting and starting and ending positions is not allowed for the length of the weld. It has also been observed that the single sided fillet weld in load bearing longitudinal welds has an exceptionally good fatigue strength in I- and box-beams with insufficient penetration. (Skriko, 2018, p. 115; Skriko et al., 2021, pp. 6–8.) In the fatigue studies of UHSS, S960 class steels have been used almost without exception.

3 Numerical methods

Numerical methods were used in the design and analysis of the stress relief groove of the welded joint. The intention was to use the effective notch stress (ENS) method and linear fracture mechanics, where the analyses of stress concentrations and stress intensity factors are concluded using the finite element method.

3.1 Finite element modelling in effective notch stress method

ENS approach is method for estimating fatigue life, based on S-N curve, that allows the effect of the local weld geometry to be directly included in the stress and takes both structural stress and notch effect into account. The ENS method is based on an idea of averaging the notch stress by using an enlarged fictitious radius ρ_f on the notch. Usually, numerical methods are used to solve the notch stress and a finite element method (FEM) is the most likely used method today. Some parametric formulae are published that can be used on standard cases. Figure 4 has an illustrative image about application of the fictitious radii and some varieties of modelling the fictitious radius at the weld toe or root. (Fricke, 2010, pp. 3–8.)
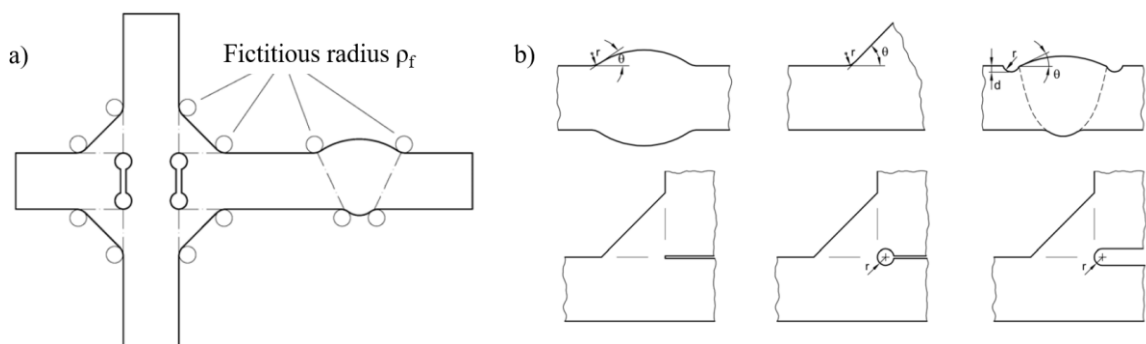

Figure 4. a) Examples of fictitious notch rounding and b) application of fictitious rounding to butt and fillet welds at the weld toe and different options for non-penetrating weld root modelling (Mod. Fricke, 2010, p. 4,9).

The position of the fictitious radius and used modelling technique may substantially affect the stress concentration factor (SCF) and thereby affect fatigue strength assessments. Using a keyhole type fictitious radius, as mentioned the design guidelines and recommendations, causes reduction of the net plate thickness and in relative thin plates the fatigue life assessment may underestimate the fatigue capacity of the joint and be too conservative. A fillet types of the fictitious radii make transition between the weld and the base material smoother and thus decreasing SCF. In some cases of root failures, this method has been found to be a more accurate method for assessing the effective notch stress, but more research is needed. These both methods of modelling the fictitious radius on the root side are illustrated in Figure 5. (Ahola et al., 2021, p. 9.)
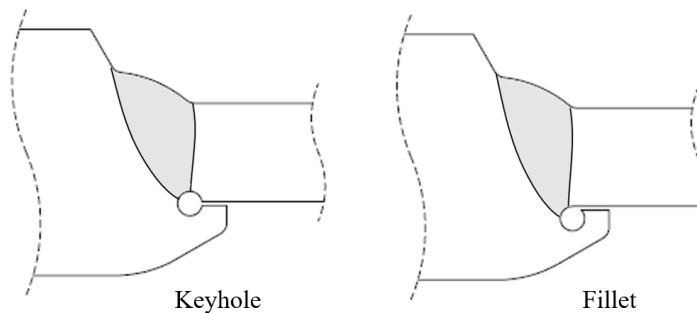

Keyhole   Fillet

Figure 5. The keyhole and fillet modelling techniques applied on the fictitious radius for the weld root.

The elements used on FEM model can be a quadrilateral or a triangular in the 2D model and a hexahedral or a tetrahedral in the 3D case and elements can have a linear or quadratic shape function.

In 2D models it is recommended to use quadrilateral elements with quadratic shape function and an aspect ratio of elements should be 2 or 3, around the fictitious radius. In 3D model, hexahedron elements should be used with the aspect ratio as 3. Number of elements over 360° circumference should be at least 24, but 50 or more is recommended so that the result converges accurately. Table 1 shows some recommendations from literature. (Baumgartner & Bruder, 2013, pp. 142–145.)

Table 1. Recommendations for elements from various literature sources for the fictitious radius (Mod. Baumgartner & Bruder, 2013, p. 138).

Author	No. of elements over 360°	No. of rings	Shape function of elements	Estimated error
Fricke	24	3	Quadratic	few %
	40	>3	Linear	few %
Gorsitzke et al.	72	6	Quadratic	< 2%
Eibl et al.	32	6	Quadratic	-/-
Kranz & Sonsino	125	-/-	Linear	-/-

In general, mesh should be relatively coarse globally and improved in scrutinized details, to decrease the needed number of elements and thus decreasing computation time. Mesh refinement should be concluded gradually to avoid large steps in element size and excessive element distortion. Examples of element refinement around the fictitious radius can be seen in Figure 6. (Fricke, 2010, p. 11.)
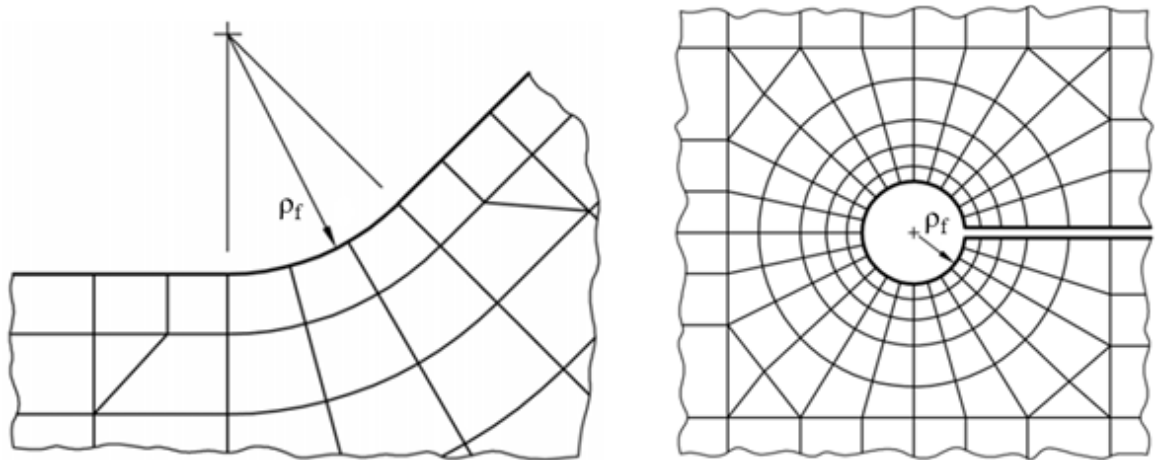

Figure 6. Typical meshes for the weld toe and root with keyhole variation (Mod. Fricke, 2010, pp. 11–12).

A recommended size of the fictitious radius for weld is $\rho_f = 1$ mm, but other radii can also be used. For example, $\rho_f = 0.05$ mm is recommended for plates under 5 mm thickness, but there has been studies which have found that, it also works well for thicker materials (Fricke, 2013, p. 763). Different sized fictitious radii have always corresponding S-N curve, that is based on experimental data and is fixed at two million cycles. For welded joints, usually slope exponent of $m = 3$ is used, but in some cases, such for base material, $m = 5$ may be more suitable. This curve is also material and stress criteria specific. On Table 2, can be seen

two alternative ENS fatigue classes (*FAT*) for steel and some comparisons about different fictitious radius size and used stress criteria. *FAT* has "build-in" internal survival probability of 97,7%. (Fricke, 2010, p. 17.)

Table 2. *FAT* classes for steel with both principal and Von Mises stress criteria and two different fictitious radius (Mod. Lindqvist & Nilsson, 2016, p. 20).

Fictitious radius	Principal stress criteria	Von Mises stress criteria
$\rho_f = 1$ mm	*FAT* 225	*FAT* 200
$\rho_f = 0.05$ mm	*FAT* 630	*FAT* 560

Recommendation for obtaining stress concentration factors from FEM model is that major principal stress criteria should be used. Von Mises stress criteria can also be used, but it needs more elements and finer mesh to converge accurate result, than major principal stress criteria. (Baumgartner & Bruder, 2013, pp. 142–145.)

3.1.1 ENS calculation

Fatigue life estimation (N_f) with the ENS method is calculated with following equation:

$$N_f = \left(\frac{FAT_{ENS}}{\Delta\sigma_{ENS}} \right)^m \cdot 2 \cdot 10^6, \tag{1}$$

where N_f is the estimated fatigue life, FAT_{ENS} is fatigue class, $\Delta\sigma_{ENS}$ is the effective notch stress range and m is the slope of the S-N curve. When the effective notch stress is calculated, the fatigue stress concentration factor K_f is used which can be calculated from the elastic stress concentration factor K_t. In the ENS method it can be assumed that $K_f \approx K_t$ ($\rho_f = 1$ mm) and thus K_t can be used when the effective notch stress is calculated with following equation:

$$\sigma_{ENS} = K_{t,m}\sigma_m + K_{t,b}\sigma_b, \tag{2}$$

where $K_{t,\mathrm{m}}$ is the elastic notch stress concentration factor for membrane and $K_{t,\mathrm{b}}$ for bending loads, and σ_m is the membrane and σ_b bending stress from real structure or structural stresses from FEM model, that has loadings that correspond real structure.

The elastic notch stress concentration factor K_t used in ENS, is a ratio between the notch and structural stress, which are in this thesis read from the FEM analysis. When FEM analyses are concluded with unit membrane and bending loads, applied nominal stress can be used instead of the structural stress. K_t stress and a maximum notch stress that can be read from FEM model and can be calculated with equation (Radaj et al., 2006, p. 107):

$$K_t = \frac{\sigma_k}{\sigma_\mathrm{s}},\qquad(3)$$

where σ_s is the structural stress and σ_k is the maximum notch stress. SCFs can be converted into a nominal fatigue strength $\sigma_{f,\mathrm{nom}}$ using equation:

$$\sigma_{f,\mathrm{nom}} = \frac{FAT_{ENS}}{K_t K_s},\qquad(4)$$

where K_s is structural stress concentration factor. The reason for the conversion is to make possible to comparison between estimated fatigue lives with different calculation methods or different sizes of fictitious radius.

3.2 Linear elastic fracture mechanics

Linear elastic fracture mechanics (LEFM) can be used to estimate the fatigue life of the specimen by means of the crack growth. Fatigue failure consist of three phases that are crack initiation, crack propagation and crack failure. In welded structures or details the crack initiation phase can usually be assumed to be really short, because welded components behave like severely notched specimens and thus crack propagation can be considered as dominant phenomenon. The fatigue life estimation on the crack propagation phase can be calculated with Paris' law using numerical integration (Jonsson et al., 2016, pp. 17–18):

$$N_{f,\text{LEFM}} = \int_{a_i}^{a_f} \frac{1}{C \cdot \Delta K(a)^{m_p}} \cdot da, \tag{5}$$

where, $N_{f,\text{LEFM}}$ is the estimated fatigue life, a_i is the initial crack length, a_f is the final crack length, C is the crack propagation coefficient, $\Delta K(a)$ is the stress intensity factor (SIF) range as function of the crack length and m_p is the slope of Paris' law. For crack propagation coefficient values, IIW recommendations propose $C = 5.21 \cdot 10^{-13}$ mm/cycle (Hobbacher, 2016, p. 73). SIF values can be calculated analytically, but in this thesis those values were determined by using a LEFM FEM program. To get fatigue life estimation comparable with the ENS method, nominal fatigue strength can be calculated with following equation:

$$\sigma_{f,\text{nom}} = \left(\frac{N_{f,\text{LEFM}}}{2 \cdot 10^6} \right)^{\frac{1}{m}} \cdot \Delta \sigma, \tag{6}$$

where $N_{f,\text{LEFM}}$ is the estimated fatigue life calculated with Paris' law, m is the slope of the S-N curve and $\Delta \sigma$ is the stress range corresponding with $N_{f,\text{LEFM}}$.

3.3 The weld root geometry optimization with numerical methods

The investigated structure has a permanent root backing in the cast piece, which leaves an initial crack at the weld root after welding. The purpose was to use FEM calculations to modify the cast geometry to minimize the SCF at the weld root and to guide the stresses away from the weld root. FEM modelling and analysis were performed using Femap 2022.2 by Siemens PLM Software Inc. and LEFM analyses using Franc2D v.4 by Cornell Fracture Group.

All models were made by using quadrilateral plane strain elements with quadratic shape function and at least 50 elements around 360° on a fictitious rounding at the weld root and toes were used. Linear analysis was used and SCFs from FEM were read by using maximum principal stress criteria. Used calculation methods on LEFM were maximum principal stress theory, on the crack growth, and SIFs were calculated with J-integral approach. The LEFM models were prepared in Femap and imported into Franc2D. LEFM models were modified from the ENS models, where a fictitious radius was replaced with an equal length geometrical crack, and on the tip of this the initial crack was applied. The size of the initial crack on every model was $a_i = 0.01$ mm and three elements were applied along its length. The growth of the crack was executed in small increments at the beginning and increased step by step. The crack growth was continued until crack length was over half from the thickness of the material.

Although the focus of the FEM analyses was improving the fatigue strength of the initial crack caused by permanent root backing, it was also necessary to solve how the replacement of the thick steel plate with a much thinner UHSS plate should be concluded. The joint without any misalignment was analysed first and an illustrative image from this weld detail with dimensions can be seen in Figure 7, where applied boundary conditions and loads on FEM are also marked. FEM models on this case were fixed from the left edge and the load was applied into right edge. Every model was analysed with membrane and bending unit loads, and separate SCF were collected from the model with each load case.
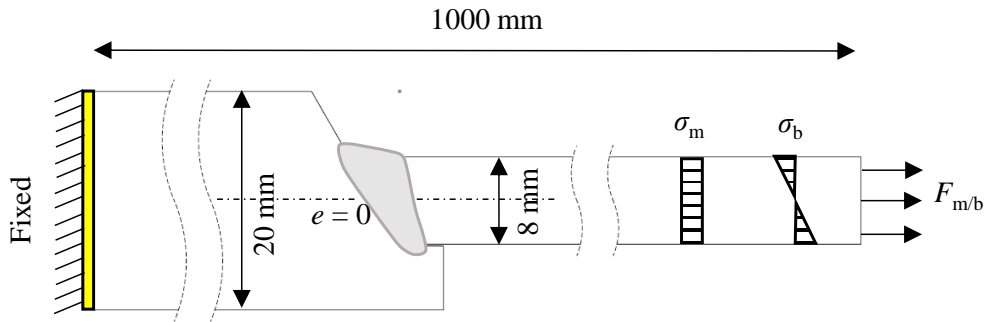
Figure 7. The first inspected weld detail between cast steel part and UHSS plate with dimensions, boundary conditions and loadings. Eccentricity $e = 0$.

The first analyses were concluded without any geometry modifications to get reference values to which the improved geometries can be compared. These models were made in FEM with every fictitious radius technique and on LEFM with both horizontal and vertical initial cracks. Results from these five models were converted into nominal fatigue strengths ($K_s = 1$) and compared in order to see how much of a difference there is between the techniques and which techniques should be applied in future calculations. In Figure 8, can be seen these previously mentioned modelling techniques at the root crack and on Table 3 are these converted $\sigma_{f,\text{nom}}$ values calculated with membrane unit load. Based on these results, it was decided to perform the future analyses with only these three FEM methods, because the LEFM results were very close to the results of the keyhole modelling technique.
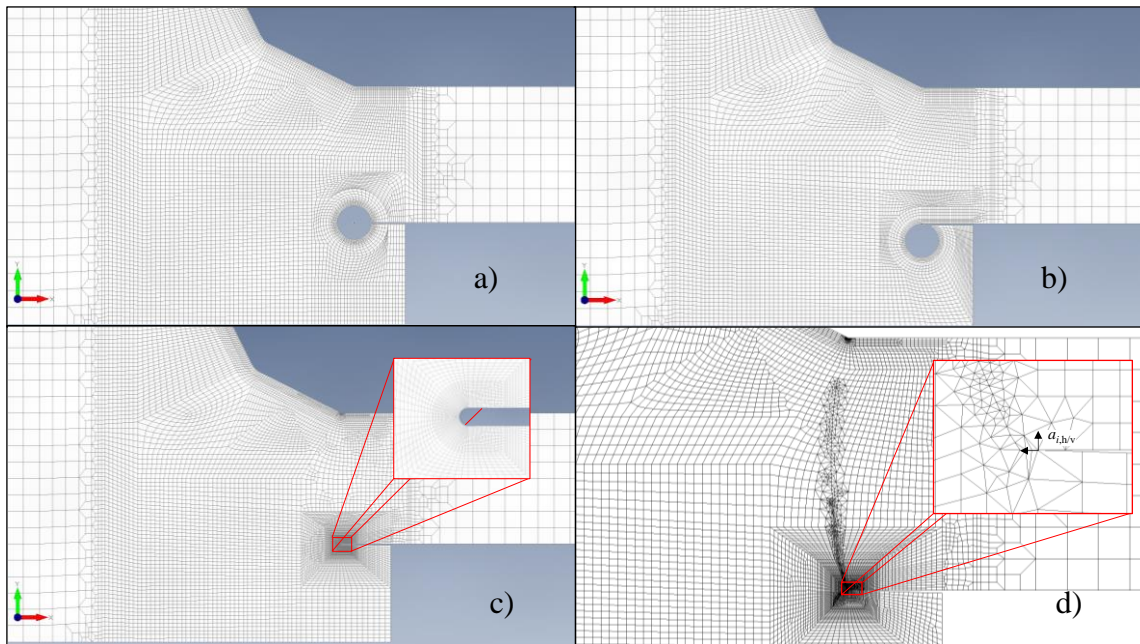
Figure 8. Different modelling techniques used for root geometry optimization, a) keyhole $\rho_f = 1$ mm, b) fillet $\rho_f = 1$ mm, c) U-notch $\rho_f = 0.05$ mm and d) LEFM with a big geometrical crack and tip of that $a_i = 0.01$ mm on horizontal or vertical direction.

Table 3. The fatigue capacity estimations of the same joint calculated with three different FEM modelling techniques and with two perpendicular initial cracks with LEFM, converted into nominal fatigue strength values.

Model	$\sigma_{f,\text{nom}}$
ENS, Keyhole $\rho_{f=}$ 1 mm	63
ENS, Fillet $\rho_{f=}$ 1 mm	103
ENS, U-notch $\rho_{f=}$ 0.05 mm	88
LEFM, Horizontal $a_i = 0.01$ mm	57
LEFM, Vertical $a_i = 0.01$ mm	56

A rough optimization was made by adding a U-notch type groove with 1 mm rounding, to the root side of the weld in the base material of the cast steel. The position of the groove tip in relation to the initial root defect was systematically varied and SCFs were collected from the fictitious rounding at the weld root with both membrane and bending unit loads and from the bottom of the groove only with membrane unit load. This process was executed with all previously mentioned fictitious radius modelling techniques.

When the rough optimization was completed, it was found that for production reasons a joint where the plate and cast at the weld surface side are aligned would be more interesting and will be used in the experimental study. An illustrative image from this weld detail with dimensions can be seen in Figure 9, boundary conditions and loads were the same as used previous joint analyses. Only difference was a positioning of the UHSS plate. This model was only analysed with $\rho_f = 0.05$ mm U-notch, because according Table 3, it appears to be a good middle ground between keyhole and fillet modelling techniques. A rough optimization was made the same way as the previous case and the model was at first analysed without any modifications to get base values to which improved results can be compared.
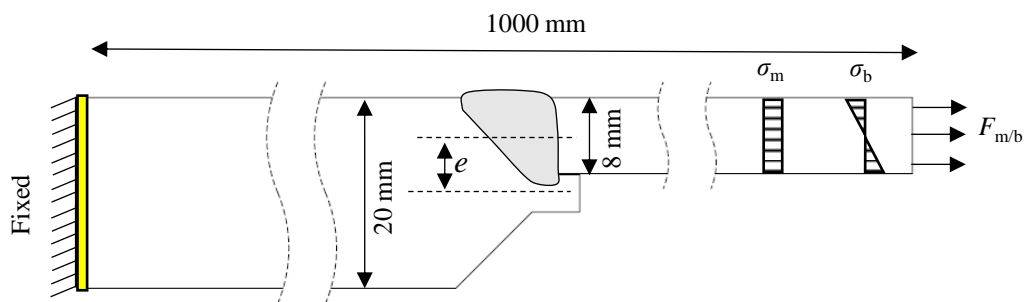

Figure 9. The second inspected weld detail between cast steel part and UHSS plate with dimensions, boundary conditions and loadings. Eccentricity, marked as *e,* of the joint causing secondary bending stress.

From the results of the rough systematic U-groove position variation, the best compromise was chosen for further development. The chosen variation was one, where SCFs at the weld root were significantly decreased from the reference model and the fatigue failure should be equally critical at the weld root and at the base of the applied groove. In further development, the geometry of the groove was smoothened and a few different radii for the groove were examined. In addition, the efficiency of the groove was compared with initial cracks of different lengths.

When the groove geometry was optimized for the welding joint of 20 mm thick cast steel and 8 mm thick UHSS plate, with the surfaces of the sides of the weld aligned, it was stated that an experimental study will be conducted with a 6 mm thick UHSS plate. This change was investigated using the groove geometry optimized for 8 mm thick plate and the plate

thickness was reduced from 8 mm to 6 mm. It was found that the optimized geometry also works in a 6 mm thick UHSS plate.

4 Experimental research

Experimental research was carried out to assess numerically analysed groove geometry modification and fatigue strength of the joint. This chapter introduces the preparation and measurements of the fatigue test specimens. In addition, the weld between cast steel and various UHSS combinations was briefly investigated in relation to the welding.

4.1 Materials

Steels used in this thesis can be found from Table 4, along with the steel number, the material standard and nominal mechanical properties to the according material standard. Heat-treated G26CrMo4 cast steel was used in the experimental study. The weld combination with it was tested with three different grades of UHSS plates: S700, S960 and S1100. S355 was taken as the control group. An additional singular test was concluded with different cast steel, G20Mn5.

Table 4. Steels used in research and their nominal mechanical properties (SFS-EN 10025-2, 2019, pp. 26–30; SFS-EN 10149-2, 2013, p. 18; SFS-EN 10293, 2015, pp. 17–18).

Steel grade	Steel No.	Material standard	f_y [MPa]	f_u [MPa]	A [%]	KV [J]	KV [°C]
G20MN5	1.6220	EN 10293	300	500 – 650	22	27	-40
G26CrMo4 QT2	1.7221	EN 10293	550	700 – 850	10	18	20
S355J2 N	1.0577	EN 10025-2	345	470 – 630	21	27	-20
S700 DQ+T	1.8974	EN 10149-2	700	750 – 950	12	40	-60
S960 DQ	1.8799	EN 10149-2	960	980 – 1250	7	27	-40
S1100 QT	-/-	-/-	1100	1250 – 1450	7	27	-40

The welding additives were chosen as matching the steel plate and from the same manufacturer to limit the variables. The commercial names, standard designation and mechanical properties of these filler wires can be seen on Table 5.

Table 5. Filler wires in research and their nominal mechanical properties.

Commercial name for filler wire	Standard designation	f_y [MPa]	f_u [MPa]	A [%]	KV [J/-40°C]
OK Autorod 12.63	EN ISO 14341-A : G 46 4 M 4Si1	490	590	29	90
OK Aristorod 69	EN ISO 16834-A : G 69 4 M Mn3Ni1CrMo	730	800	19	73
OK Aristorod 89	EN ISO 16834-A : G 89 4 M Mn4Ni2CrMo	920	940	18	47

Carbon equivalent content (CE) is commonly used to estimate weldability of the steels and it is mainly used to assess the risk of cold cracking. The chemical composition of the steel directly affects the risk of cold or hydrogen cracking phenomenon, due alloying elements that affect the hardening of steel. There are multiple equations for calculating CE, which is used to assess the risk of cold cracking based on the chemical composition of the material, but the two most common methods are: CE_{IIW} that is mainly for carbon manganese type steels and CET that is mainly for low-alloy high-strength-steels. Both these methods are based on extensive experience and data. CE_{IIW} and CET can be calculated with the following equations (Lukkari et al., 2016, pp. 7–21; SFS-EN 1011-2, 2001, p. 25,59):

$$CE_{IIW} = C + \frac{Mn}{6} + \frac{Cr + Mo + V}{5} + \frac{Ni + Cu}{15} \tag{7}$$

$$CET = C + \frac{Mn + Mo}{10} + \frac{Cr + Cu}{20} + \frac{Ni}{40} \tag{8}$$

In equations (7) and (8), amounts of elements are in mass percentages (w-%).

When CE_{IIW} is more than 0.45 weldability starts to deteriorate depending on structure and material thickness. This causes preheating, low hydrogen-content welding consumables and post-weld heat treatments to start to become relevant. Because solid wire additives were used on experimental research and those have very low hydrogen content, this thesis does not go deeper into hydrogen cracking mechanisms or how it can be mitigated. There is no clear limit for the CET value when you should worry about the quality of the welding, but there are several formulas for calculating the need for preheating. CE is still used to roughly

evaluate the weldability of steels used in experimental research. (Lukkari et al., 2016, pp. 7–21).

Chemical composition of G20Mn5 and G26CrMo4 cast steels were analysed with optical spectrometer (Appendix I & Appendix II). Plates came with material certificates that included chemical composition. Element amounts that are needed on previous CE equations are presented on Table 6 and CE values are presented on Table 7.

Table 6. Chemical composition of the steels used on research and element composition needed on *CE$_{IIW}$* and *CET* calculations.

Steel	C [w-%]	Mn [w-%]	V [w-%]	Cu [w-%]	Cr [w-%]	Ni [w-%]	Mo [w-%]
G20Mn5	0.180	1.191	<0.0050	0.014	0.077	0.029	0.024
G26CrMo4	0.261	0.828	0.0056	0.013	0.946	0.023	0.177
S355	0.152	1.42	0.008	0.017	0.07	0.05	0.005
S700	0.055	1.81	0.012	0.014	0.05	0.04	0.003
S960	0.086	1.08	0.009	0.009	1.12	0.06	0.126
S1100	0.129	1.48	-	0.439	1.29	0.99	0.371

Table 7. Calculated *CE$_{IIW}$* and *CET* values for steels used in research.

Steel	*CE$_{IIW}$*	*CET*
G20Mn5	0.40	0.31
G26CrMo4	0.63	0.41
S355	0.41	0.30
S700	0.37	0.24
S960	0.52	0.26
S1100	0.80	0.43

According to calculated CE values some steels should need at least preheating and additionally, standard SFS-EN 10293: Steel casting for general engineering uses, instructs to using 150-300 °C pre-heating and post weld heat treatment for G26CrMo4 cast steel (SFS-EN 10293, 2015, p. 28). On this research from these instructions were deviated and no elevated welding temperature or post-weld heat treatment were used. The main reason was UHSS plates, which are quite delicate to heat input, and another was to enhance productivity, by skipping quite time-consuming heating procedures. The goal was to achieve a good

compromise between the sufficient quality and strength of the weld by adjusting heat input used on welding.

Heat input (Q) differs from the arc energy by the thermal efficiency of the used welding process and is the amount of heat energy that is deposited to the base material during welding. Heat input strongly affects the cooling rate of the weld and thus the microstructures in the vicinity of the weld and can be calculated with equation (SFS-EN 1011-2, 2001, p. 78):

$$Q = \frac{k \cdot U \cdot I}{v \cdot 1000},$$ (9)

where k is the thermal efficiency of the welding process and for GMAW it is 0.8, U is the welding voltage, I is the welding current and v is the welding speed.

Cooling time from 800°C to 500°C is commonly used to measure cooling rate at the weld. The cooling rate of the weld is affected by the thickness of the materials, the type of joint and the heat input during welding. There are two equations that are used to estimate heat flow and cooling on the weld. One is made for 2D case, which uses material thickness parameter, where it is assumed that the heat is dissipated in only two directions. Other is used for 3D cases, where the thickness of the material is assumed to be thick enough that it is numerically stabile and no longer affects the heat flow calculation and heat can dissipate freely in every direction. On 2D and 3D cases, $t_{8/5}$ can be calculated with following equations (SFS-EN 1011-2, 2001, pp. 78–79):

$$t_{8/5,2D} = (4300 - 4.3T_0) \cdot 10^5 \cdot \frac{Q^2}{t^2} \cdot \left(\frac{1}{(500 - T_0)^2} - \frac{1}{(800 - T_0)^2} \right) \cdot F_2$$ (10)

$$t_{8/5,3D} = (6700 - 5T_0) \cdot Q \cdot \left(\frac{1}{500 - T_0} - \frac{1}{800 - T_0} \right) \cdot F_3,$$ (11)

where T_0 is the initial plate temperature, t is the thickness of the plate and F_2/F_3 are shape factors for 2D and 3D heat flows, which is 0.9 on both cases with single-bevel-groove butt weld (SFS-EN 1011-2, 2001, p. 79).

The recommended heat inputs and $t_{8/5}$ times of the steel plates were searched from steel manufacturer's welding instruction documents and using their welding calculator app, Table 8.

Table 8. Recommended heat inputs and $t_{8/5}$ times for used steel plates according by manufacturer.

Steel	Q [kJ/mm]	$t_{8/5}$ [s]
S355	1.05 - 2.25	1 - 20
S700	0.21 - 1.12	1 - 20
S960	0.19 - 0.73	1 - 15
S1100	0.19 - 0.59	5 - 20

According to standard SFS-EN ISO 15614-1, "Specification and qualification of welding procedures for metallic materials. Welding procedure test. Part 1: Arc and gas welding of steels and arc welding of nickel and nickel alloys.", the maximum allowable hardness values for QT steels without heat treatment after welding is 450 HV10. The same standard has been applied also to DQ steels in this thesis. (SFS-EN ISO 15614-1 + A1, 2019, p. 20.)

4.2 Test specimens

Test specimens were designed very early of this research, because it was known that delivery and production of cast steel pieces takes a lot of time. This caused test specimens to be big enough to be suitable for many testing equipment and it is easier to remove material than add. Cast steel material used on all test specimens was 20 mm thick and all geometries and surfaces were machined. S355 plate that was used as control was 20 mm thick and on higher grade steels, plate thickness was decreased so that the capacity of the plate remained close at the S355 level. All plates, regardless of thickness, were cut with a fiber laser using nitrogen as cutting gas. All used material thicknesses can be seen on Table 9.

Table 9. Thicknesses of used steels and used cutting methods.

Steel	t [mm]	Cutting method
G20Mn5	20	Machined
G26CrMo4	20	Machined
S355	20	Fiber laser, N_2
S700	8	Fiber laser, N_2
S960	6	Fiber laser, N_2
S1100	6	Fiber laser, N_2

The cast steel was 20 mm thick on every test specimen and thickness of steel plate varied. The narrowed area in the middle of the specimen had wings that had starting and the ending points of the weld. Wings were cut after welding and macro graphs were made from these cross sections for hardness and microstructural examination. Sides of the narrowed area were machined and grinded before any testing to have uniform width and as flawless a surface as possible. The final width of the fatigue test specimen was 50 mm and on tensile test specimens 40 mm. Schematics of the finalized test specimens can be seen in Figure 10.
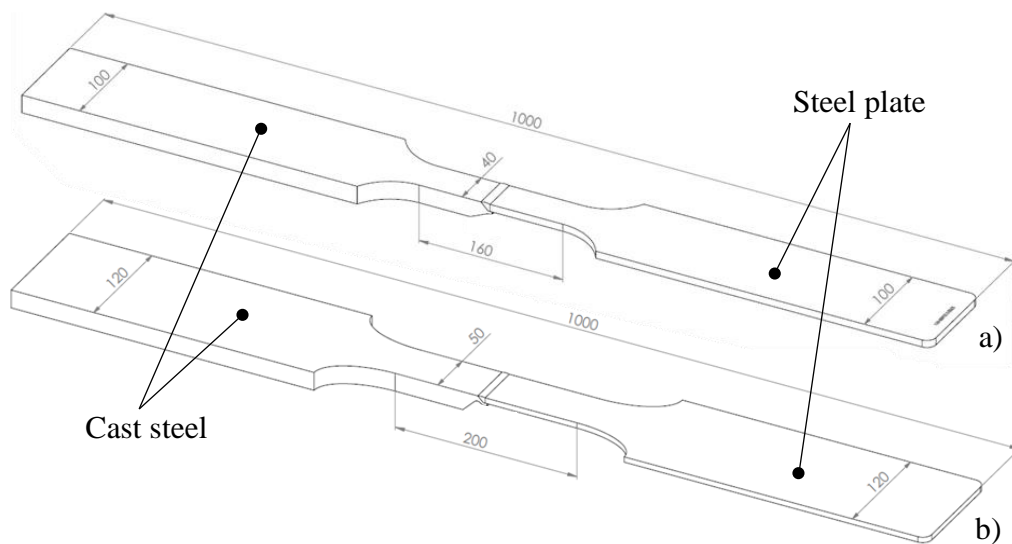

Figure 10. Dimensions of the finished test specimens, a) a test specimen for the quasi-static test and b) a test specimen for the fatigue test.

At first tensile test specimens were made and tested. Testing included tensile test and hardness measurements, which were made to test and proof welds between G26CrMo4 cast steel and all three researched UHSS grades along with S355 as control. An additional

singular test was executed with G20Mn5 cast steel combined with S700 plate. In Table 10 is presented a test matrix for tensile tests. The amount of test specimens was one actual test specimen and two spare specimens per dissimilar joint. Spare specimens were made in case technical problems appeared on the tensile test procedure or unexpected results needed to be verified.

Table 10. Test matrix for tensile test.

ID.	Plate	Cast steel	Number of test specimens
35G26_S1-3	S355	G26CrMo4	1 + (2)
70G20_S1-3	S700	G20Mn5	1 + (2)
70G26_S1-3	S700	G26CrMo4	1 + (2)
96G26_S1-3	S960	G26CrMo4	1 + (2)
11G26_S1-3	S1100	G26CrMo4	1 + (2)

For fatigue tests, material pair used on tensile test 96G26_S was chosen. Four fatigue test series were completed, three of which are related to root geometry modification, and one is a control series from S355. Geometry modifications were performed with FEM and more on geometry optimization is presented in Chapter 5.1 , final optimized geometry used on FA series can be seen on Appendix VIII. The test matrix for fatigue specimens can be seen on Table 11. Root geometry test series have six test specimens and control series four specimens. Every fatigue test series has two spare specimens. Differences on fatigue series are: FA series has the calculated groove on cast steel root, FB series has even more aggressive groove and this series is split into two, the first tested part as welded (AW) condition (specimens 96G26_FB1-3) and the rest (specimens 96G26_FB3-8) are high-frequency impact treated (HFMI), and FC series has the same geometry than tensile test specimens. The control series specimens also have the exact same geometry as the tensile test specimen.

Table 11. Test matrix for fatigue tests. Material combinations were same than with 35G26_S and 96G26_S tensile test series.

ID	Variation	Number of test specimens
96G26_FA1-8	Grooved	6 + (2)
96G26_FB1-8	Aggressive groove + HFMI	3 +3 + (2)
96G26_FC1-8	Tensile test geometry	6 + (2)
35G26_FD1-6	Control	4 + (2)

4.2.1 Welding of the test specimens

The weld between cast steel and steel plate was designed as single-bevel-groove, where the bevel was machined into the cast steel piece along the permanent root backing. Edge of the plate was left as cut. The surfaces two pieces were aligned on the same level which caused axial misalignment with UHSS to cast steel connections, except 20 mm thick S355. In Figure 11, can be seen schematic of weld with 20 mm cast steel and 8 mm plate. Dimensions of the root backing, 2 mm "air gap" at root and bevel angle remained unchanged in each different data set. The welding procedure specifications (WPS) were performed with tensile test specimens and even thought fatigue specimens had divergent weld root geometries, the same WPS' were used.
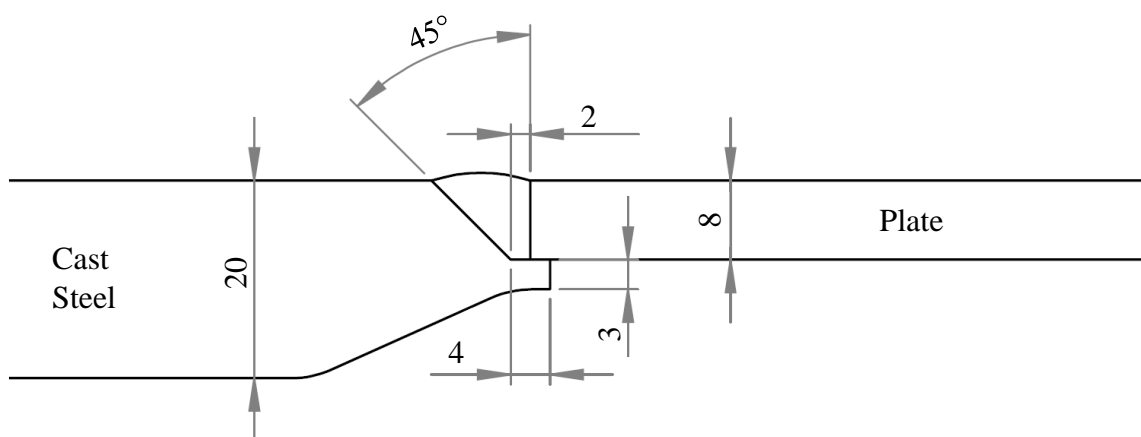

Figure 11. The dimensions of the designed weld at tensile test specimens, where permanent root backing and single-bevel-groove were machined on cast steel and plate was left as cut. Dimensions at mm.

Test specimens were welded using GMAW process with mixed welding gas (8% CO_2 + Ar) and welding was executed with a robot on PA position. Welded steels were cleaned on a citric acid bath and were clamped into the welding jig before welding. Welding setup can be seen in Figure 12.
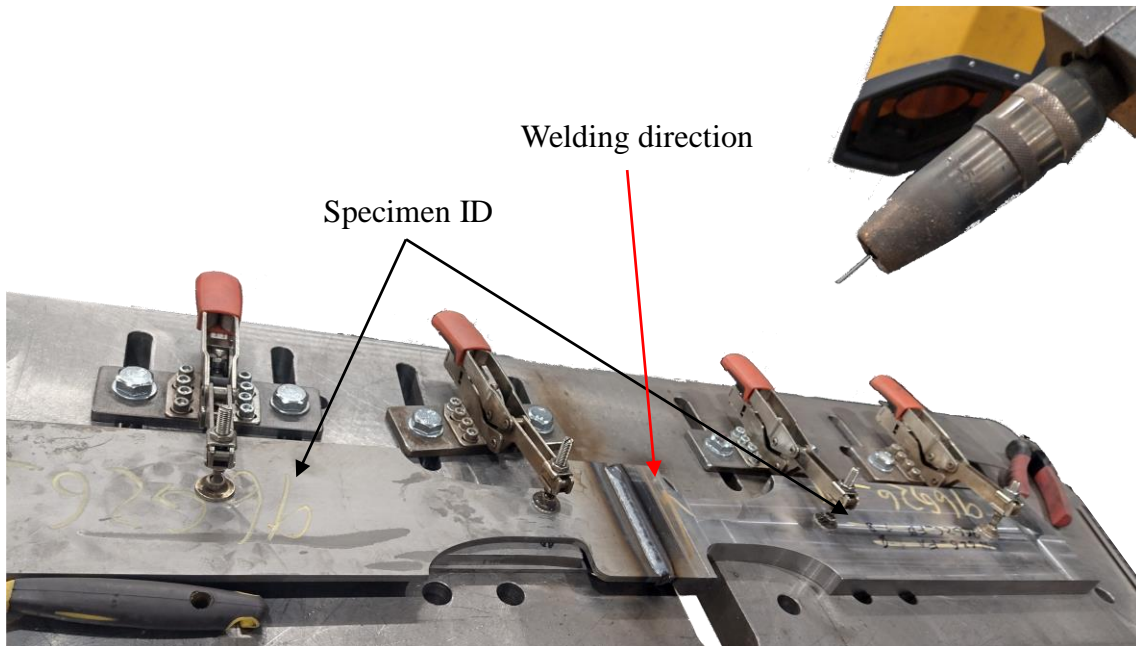

Figure 12. Welding setup and markings on specimens. On this image, wings that have welding start and stop points, can be seen.

At the beginning of WPS development, the welding parameters were chosen based on calculated $t_{8/5}$ times and collective experience from similar joint type and materials. Welding was performed into welding trial samples that had real joint geometry and materials, but in the smaller scale. After that a polished macro graph was made from the weld cross section and hardness was measured from cast steel base material to weld. Based on geometrical and hardness information from the weld, the welding parameters were adjusted, until weld geometry, root penetration and hardness were acceptable.

Figure 13 presents macro graph of the first test weld between G26CrMo4 and S960. Welding was executed with two pass which both had the same welding parameters, where $Q = 0.59$ kJ/mm, interpass temperature 50 °C and the torch was targeted into a lower corner of the plate with 30° angle. Many voids and cracks were found from macro graph. The whole cast steel base material was full of small 40-50 µm diameter voids. It seemed like those voids were combined into cracks in the HAZ and at lower part of the cross section.
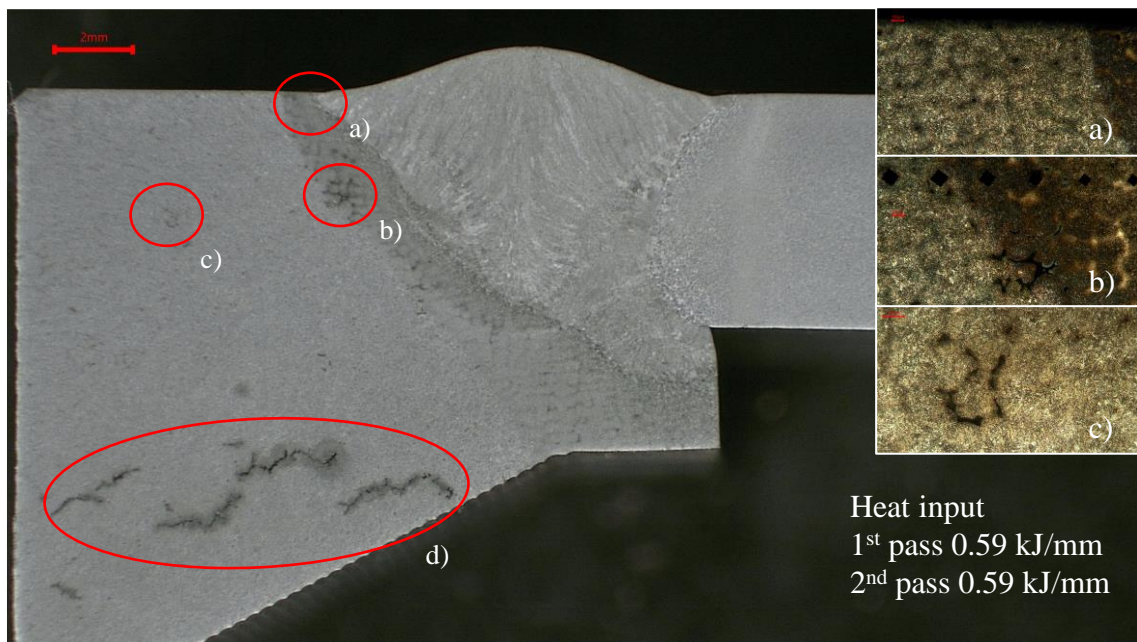
Figure 13. The first weld between G26CrMo4 (t = 20 mm) and S960 (t = 6 mm). Cracks and voids were found from HAZ and the base material on cast steel a) small voids (40-50 µm) on HAZ, b) voids that are connected into bigger cracks on HAZ, c) small voids everywhere on base material, some are connected, d) bigger cracks at base material.

Hardness measurements in this thesis were performed using automatic measurement device that used Vickers hardness measurement method with 5 kg force. In this specimen, a straight measurement line that was about 1.75 mm below the surface of the plate, on weld toe side, 17 measurements points were made. The hardness curve is presented in Figure 14, and from that can be seen that casts steel hardens strongly and very hard microstructures (540 HV5) can be observed HAZ close to fusion line. Like previously mentioned standard allows the maximum hardness of 450 HV10 on QT steels.
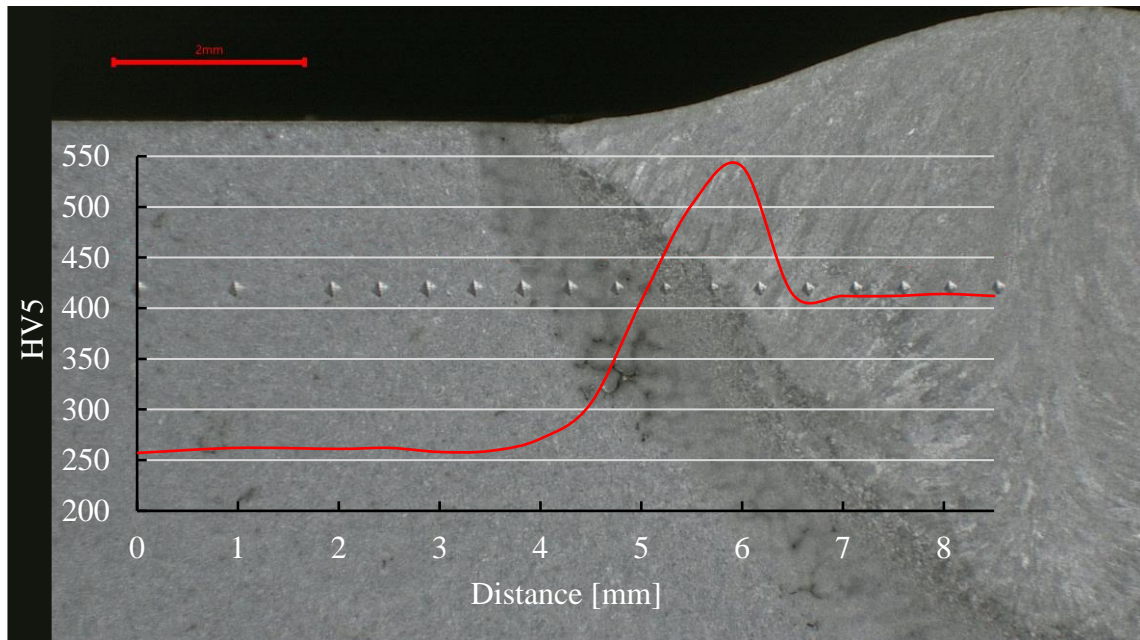
Figure 14. Hardness curve from same weld than in Figure 13 from cast steel base material into the weld.

Additional inspection for the welded test specimen that was presented in Figure 13 and Figure 14 was performed with an electron scanning microscope (SEM) and an energy-dispersive X-ray spectroscopy (EDS), to find possible reasons why and how cracks were formed and what is this darker mesh structure on HAZ (cast steel side). Expertise of university's researchers were used to analyse results.

The preliminary investigation of the welded joints indicated star-shaped cracks and such crack morphologies are not typical among HAZ cracks directly caused by welding. Because cracks were apparent even in numerous areas of the base material, which supports an idea that the natural origin of the cracks cannot be attributed solely to the welding procedure. However, the shapes of the defects, either in the base metal or in the HAZ, resemble the defects caused by sulfide embrittlement or sulfide liquefaction at high temperatures, Figure 15. (Afkhami, 2022.)
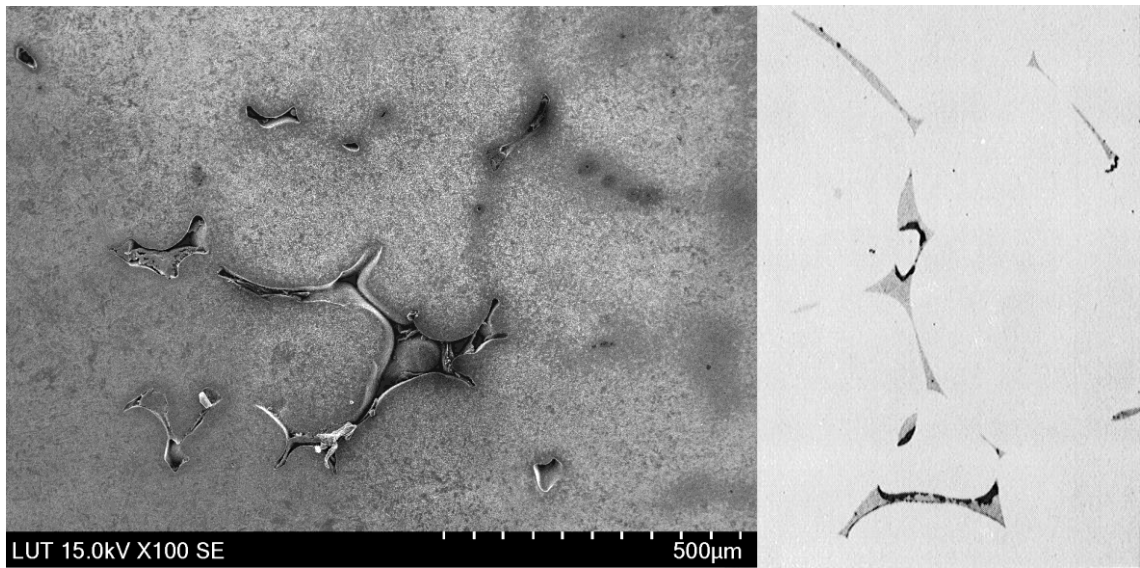
Figure 15. On left a SEM image from Figure 13b) crack and on right image from literature about an intergranular sulfide distribution and transformation to sulfide liquid at high temperature in steel (Van Vlack et al., 1958).

Many precipitates as large as 20 μm were found from base material and EDS was used to confirm the composition of these precipitates, Figure 16. EDS confirmed these to be sulfur-manganese compounds, and micro-voids and micro-cracks were found in the vicinity of some of them. (Afkhami, 2022.)
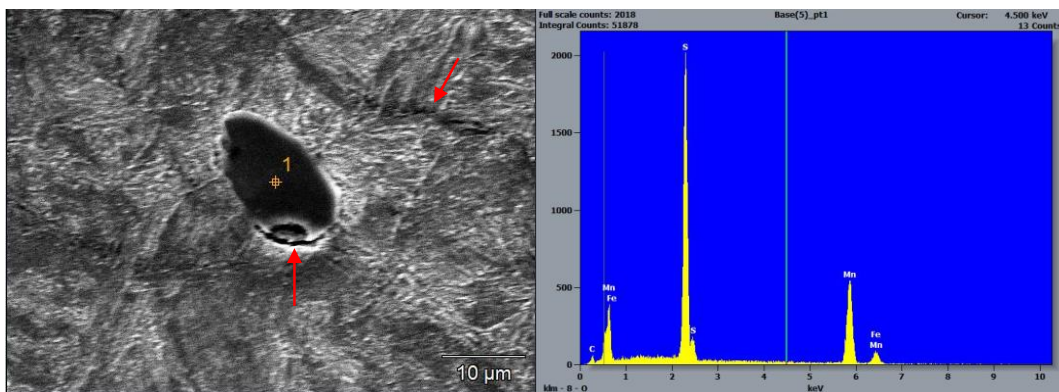

Figure 16. EDS analysis confirmed found precipitates to be sulfur-based impurities. Some sulfur-based precipitates were even accompanied by micro-voids and micro-cracks.

A darker mesh-like pattern on HAZ was found to be locally more compact martensitic networks, Figure 17, which indicates local fluctuations on base material's response to welding heat input and its subsequent cooling stage. Such localized responses can point to segregation and lack of chemical homogeneity in the base material. Fluctuations in carbon

contents would also explain different martensitic features in the HAZ zones that experienced similar thermal gradients. (Afkhami, 2022.)
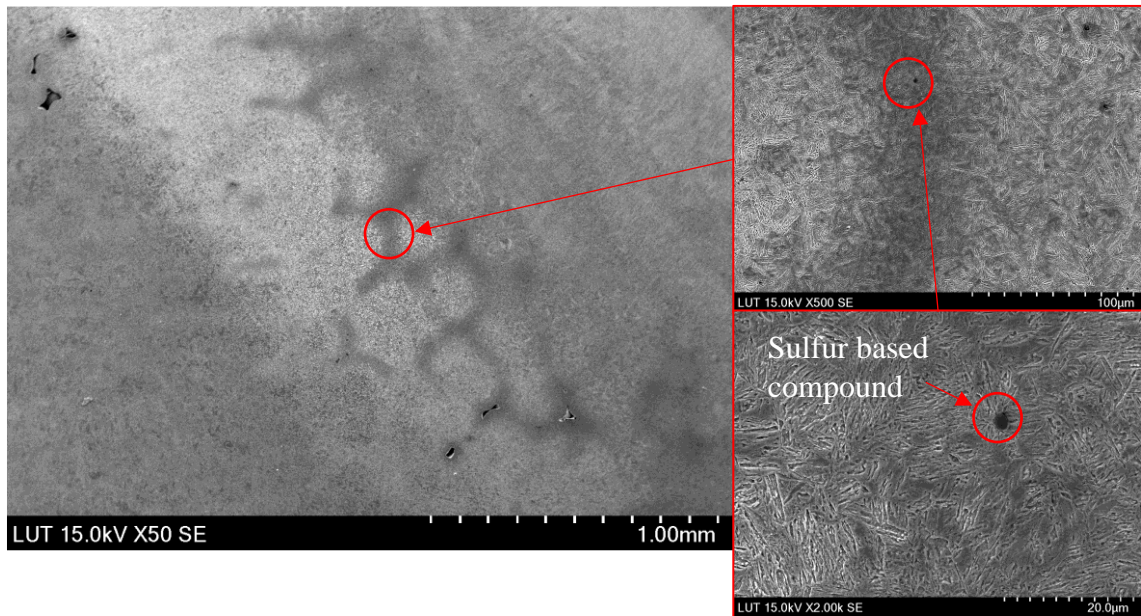

Figure 17. Mesh like pattern in the HAZ, was observed to be locally compact martensitic networks. Sulfur-based impurities were also found from there.

Although the general chemical composition (Appendix I) of the base metal does not indicate any unfavourable feature in the results, previously mentioned segregation can lead to the sporadic presence of sulfur-based impurities, even though the general sulfur content might seem normal according to spectroscopy. (Afkhami, 2022.) The assumption was made that cast steel behaves in the same way in all welds, so no other welds were analysed with SEM or EDS.

Based on SEM and EDS results, the one major issue for internal defects in cast steel seems to be quality of the cast steel, and it was not possible to obtain new cast steel material for this thesis. Based on these results, hypothesis was formed, that increase on heat input may help, but the trade-off was that some UHSS grades may soften, which leads into decreased load bearing capacity. An idea behind increased heat input was longer $t_{8/5}$ time which should retard the formation of hard microstructures and additional heat may heat treat previous passes. Increased heat input on the root pass led into situation that the weld burned through the root backing, and it was noticed that about 0.65 kJ/mm was a limit which backing still

survived without melting. There were still some individual cases, where root backing didn't sustain the heat, but it was probably due to the quality of the casting.

The welding torch position was change from a lower edge of the plate into 1 mm away from edge and the torch angle was decreased from 30° into 25° on the root pass, to get a similar unmelted longitudinal crack into the weld root on every material combination. In Figure 18 can be seen an ideal root pass, which has a good penetration without burning through the permanent root backing and still having a short-unmelted crack at the top of the root backing.
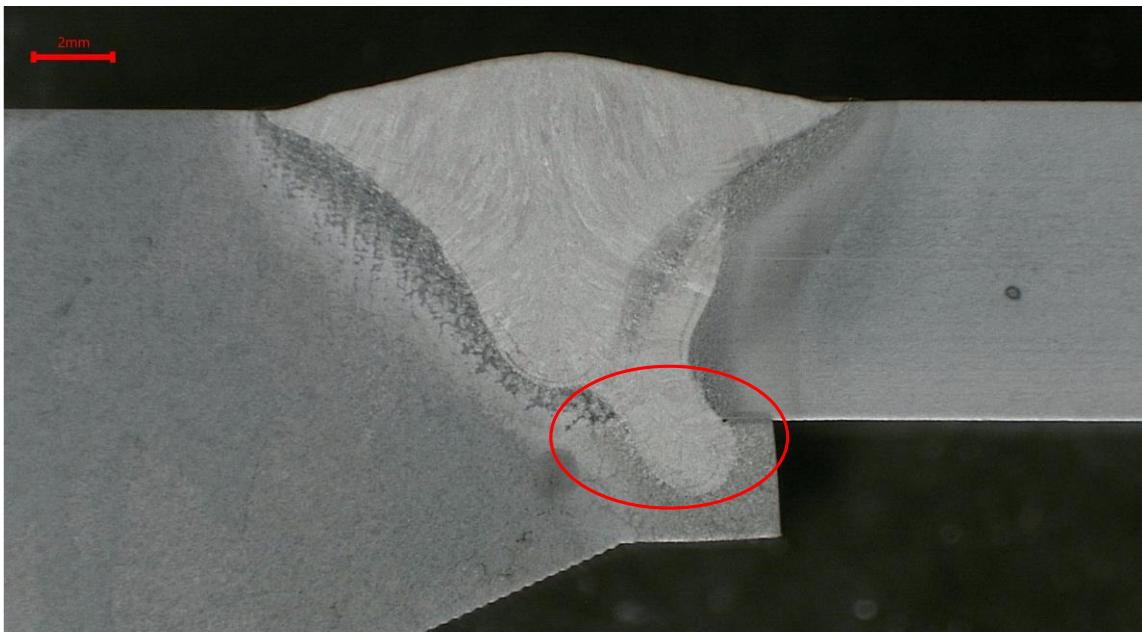

Figure 18. The weld between S700 and G26CrMo4 steels with adjusted welding parameters and torch positioning. These changes resulted a good penetration for the root pass with a desired short unwelded section which worked as the initial crack.

The final welding parameters that were used can be seen on Table 12 and full WPSs can be found from Appendix III. These welding parameters were made by using a tensile test specimen root geometries and the thickness of the steel plate was used on $t_{8/5,2D}$ calculation, although two plates had different thicknesses.

Table 12. Welding parameters used on all welds and $t_{8/5}$ estimations. S960 and S1100 plates were welded with same WPS. Material thickness used on $t_{8/5,2D}$ calculation was a thickness of the thinner material of the joint.

WPS	Pass No.	U [V]	I [A]	v_{wire} [m/min]	v [mm/s]	T_0 [°C]	Q_{avg} [kJ/mm]	$t_{8/5,2D}$ [s]	$t_{8/5,3D}$ [s]
S355	1.	24.3	220-225	10.0	7.0	20	0.62	1.1	3.1
	2.	25.4	255-265	11.5	3.0	100	1.86	11.4	10.5
	3.	25.4	250-260	11.5	2.7	100	1.92	13.5	11.5
	4.-6.	25.4	220-230	11.5	3.8	100	1.20	5.3	7.2
S700	1.	25.3	270-280	11.5	8.5	20	0.65	6.8	3.1
	2.	25.6	270-275	12.0	5.0	50	1.12	22.8	5.8
S960/S1100	1.	24.0	230-240	10.0	7.3	20	0.62	10.9	3.0
	2.	25.8	255-260	12.0	6.5	50	0.82	21.7	4.2

High-frequency impact treatment was performed in three passes into the groove of the 96G26_FB4-8 specimens. The purpose of the HFMI treatment is to obtain compressive residual stress into the treated surface. In this case, the treatment was executed with the biggest tool available, with radius of 2.5 mm. Because radius of the groove was 4.5 mm, treatment was concluded in three passes, the last of which was made at the bottom of the groove. In Figure 19, schematic from treatment can be seen.
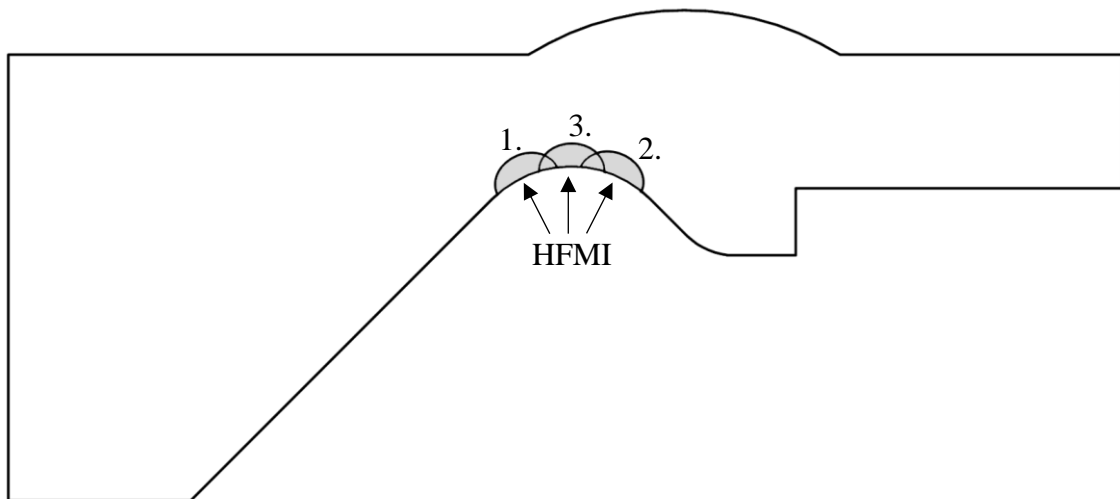

Figure 19. The HFMI treatment was performed in three passes, where the sides of the groove were treated first and then the bottom of the groove.

Strain gauges were used to measure structural stress and degree of bending (DOB) on each fatigue specimen. The strain gauge was glued to each fatigue test specimen at $0.4t$ distance from the weld toe. The recommended maximum size of the strain gauge grid is determined by the thickness of the measured material, which is $0.2t$ (Hobbacher, 2016, p. 25). In this thesis with a 6 mm thick plate, a strain gauge with the grid size of 0.6 mm was used and on a 20 mm thick plate the used strain gauge had the grid size of 3 mm. One strain gauge was glued on each fatigue test specimen. An additional strain gauge was added into one test specimen per test series the opposite side of the plate, to verify the results of the first gauge. In Figure 20 position of the strain gauges and a terminal can be seen. Very thin wires of the strain gauge are soldered to the terminal, which is connected to measurement device with longer and thicker wires.
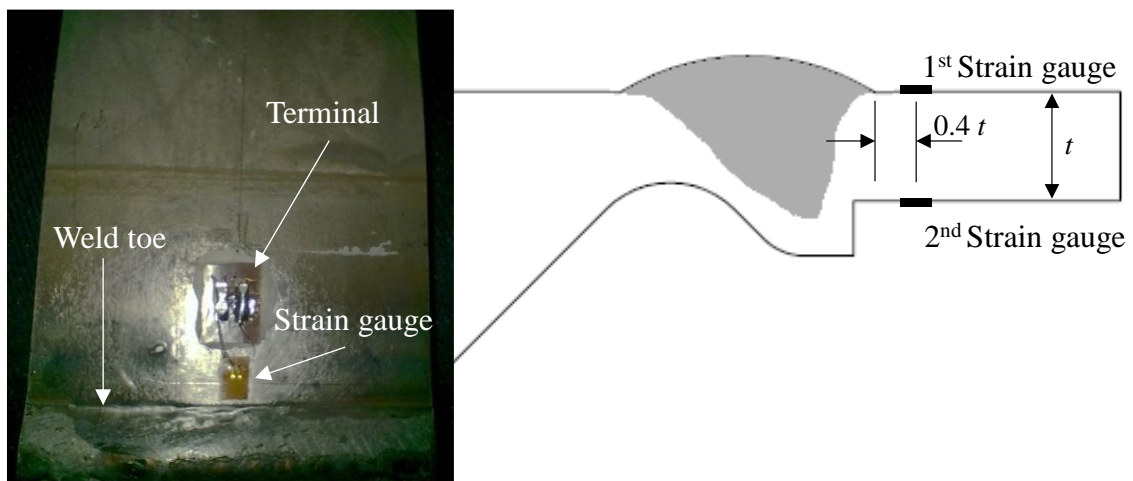

Figure 20. Strain gauge positions, each fatigue test specimen had strain gauge at the first position and a one specimen per series had gauge also on the second position. The strain gauge was glued at $0.4t$ distance from the weld toe and the terminal to which the wires were soldered was glued after that.

4.2.2 Test specimen measurements

Hardness measurements were performed from every tensile test specimen and one test specimen was measured from one specimen of each fatigue test series. Two measurement lines were made into a macro graph of the weld at 1 mm under surface and 1 mm above root backing. Both lines go over the weld from base material to base material.

On G20Mn5 cast steel cases maximum hardness was found from the surface side of cast steel HAZ, where measured maximum hardness was 330 HV5. G26CrMo4 cast steel had a noticeable higher hardenability than G20Mn5. This could be seen on every specimen where G26CrMo4 was used. The maximum hardness was found from close to the surface of cast steel in HAZ, where the measured maximum hardness was generally a little bit over 450 HV5, which is above permitted limit according standard. In this study, the hardness values were interpreted to be within quite reasonable limits. 35G26_S1 specimen was exception, and hardness jumped over 600 HV5. Reason for this was probably the last pass that was welded to the casting side with too low interpass temperature (100°C). On other side of the weld in steel plate HAZ, considerable softening is observed in both the S700 and S960 plates. Softening was on S700 steel about 10-15 % and on S960 about 30% from base material hardness value. All results and graphs can be found from Appendix IV & Appendix V.

In the inspection of the hardness measurement cross-section, a few samples with welding defects were detected. The detected defect was on each case lack of the penetration. In Figure 21 are two images from test specimen 96G26_FB2 where lack of penetration was detected on the hardness measurement sample, but the fracture sample that was taken from the middle of the test specimen had impeccable penetration. The lack of penetration was probably due to too short weld start wing, which is why the start of the weld still could affect the quality of the weld.
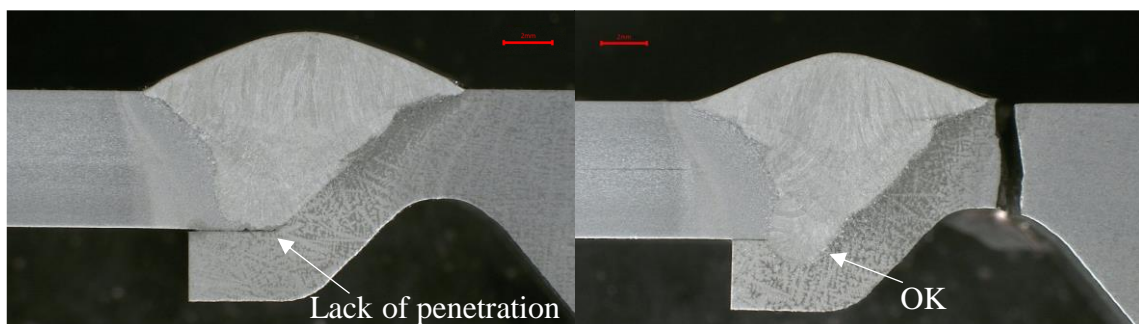

Figure 21. Weld penetration on 96G26_FB2 test specimen. Sample on the left is taken from removed weld start wing and a sample at the right is taken middle of the specimen after fatigue test.

From each fatigue test series, one specimen from was 3D scanned and the residual stresses were measured from the surface of the plate. In addition, from the FB series, both measurements were performed in the specimen with and without HFMI treatment, and an additional residual stress measurement was made on the root groove. On following measurements specimen 96G26_FB5 is HFMI treated and 96G26_FB3 is without treatment.

The scanned area was a strip approximately 60 mm wide where the weld was located in the middle of the area, and both the weld and root surfaces were scanned. Scanning was performed with HP-L-20.8 Laser Scanner which was attached to ROMER Absolute Arm. Three cross-sections were cut from the surface model formed after scanning, from which geometric measurements were made. Two of these cross-sections were taken at a distance of a few millimetres from the edges of the piece and one from the centre of the piece. In Figure 22 is the scanned surface model from 96G26_FB3 specimen and three cross-section section lines can be seen on image.
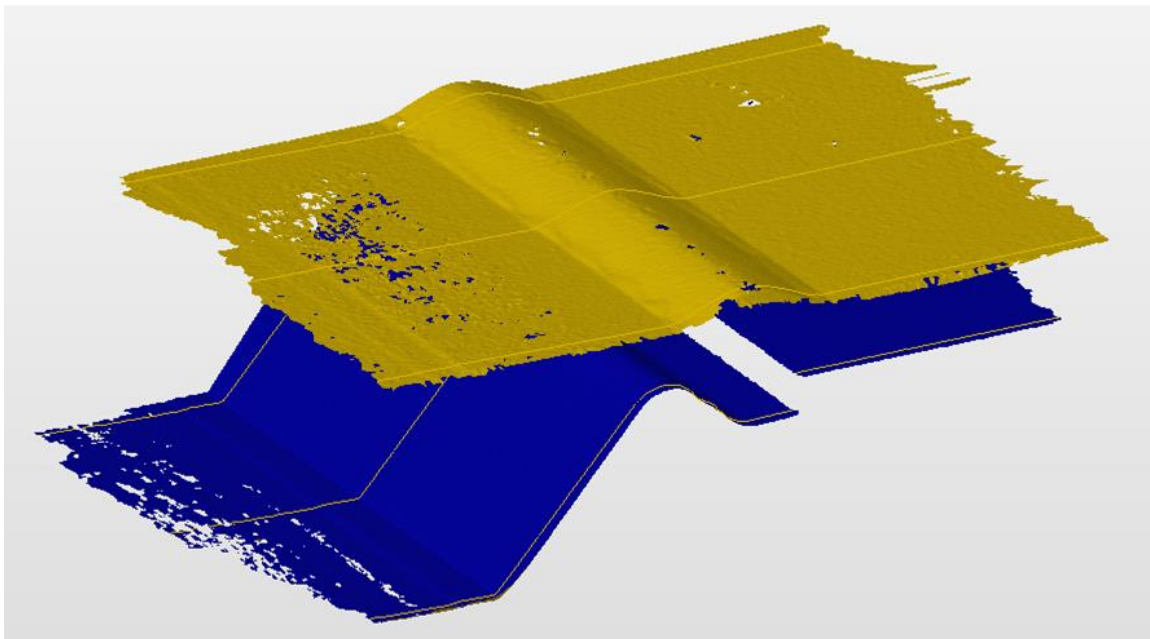

Figure 22. 3D scanned surfaces and three section view lines from which geometry measurements were made.

Geometrical measurements were executed from these three cross-sections on every specimen. Each measured test specimen was really straight and measured angular misalignment was under 0.5° on every specimen, no axial misalignment was detected from

the measured test specimens, which is probably due to the clamping of the pieces against the root backing and welding table, during welding. In Figure 23 is shown measured dimensions from each test specimen series and values can be found from Table 13. Measured dimensions were material thickness in the groove, radius of the groove r, location of the groove d and the weld dimensions width w and height h. The presented results are the calculated average of three cross-sections, and the variation between these three cross-sections is added after each result. In the drawings (Appendix VIII), the notch dimensions were defined as $t = 6.0$ mm, $r = 5.0$ mm and $d = 10.24$ mm for specimens 96G26_FA1-8 and $t = 4.5$ mm, $r = 4.0$ mm and $d = 11.39$ mm for specimens 96G26_FB1-8.
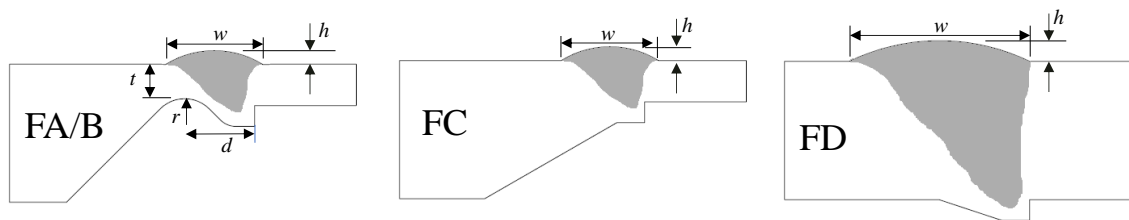

Figure 23. Measurements taken on scanned cross-sections.

Table 13. The calculated averages of three cross-sections from 3D data, and the variation between these three cross-sections.

Specimen ID.	w [mm]	h [mm]	t [mm]	r [mm]	d [mm]
96G26_FA1	14.3 ± 0.2	1.99 ± 0.02	6.09 ± 0.03	4.4 ± 0.15	10.25 ± 0.02
96G26_FB3	13.7 ± 0.25	1.99 ± 0.02	4.59 ± 0.02	3.39 ± 0.05	11.25 ± 0.01
96G26_FB5	13.8 ± 0.15	1.89 ± 0.03	4.68 ± 0.15	3.48 ± 0.1	11.53 ± 0.04
96G26_FC1	13.6 ± 0.2	2.19 ± 0.04	-/-	-/-	-/-
35G26_FD1	27.7 ± 0.2	1.91 ± 0.05	-/-	-/-	-/-

The residual stresses were measured with X-Ray diffractometer: Stresstech XSTRESS 3000 which was equipped with G3-goniometer. In Figure 24 are images from the measurement setup. The measurements were made from surface of the plate starting from the weld toe with 1 mm increments. Additional measurements were taken from one point bottom of the notch groove at 96G26_B3 and 96G26_B5 specimens to measure the effect of the HFMI treatment.

Figure 24. X-Ray diffractometer setup on residual stress measurements.

In Figure 25 is presented residual stress curves from every measured specimen. The residual stresses measured are relatively in accurate, but trend and order of magnitude can be measured and in this case the margin of error in the stress value was approximately ±50 MPa.
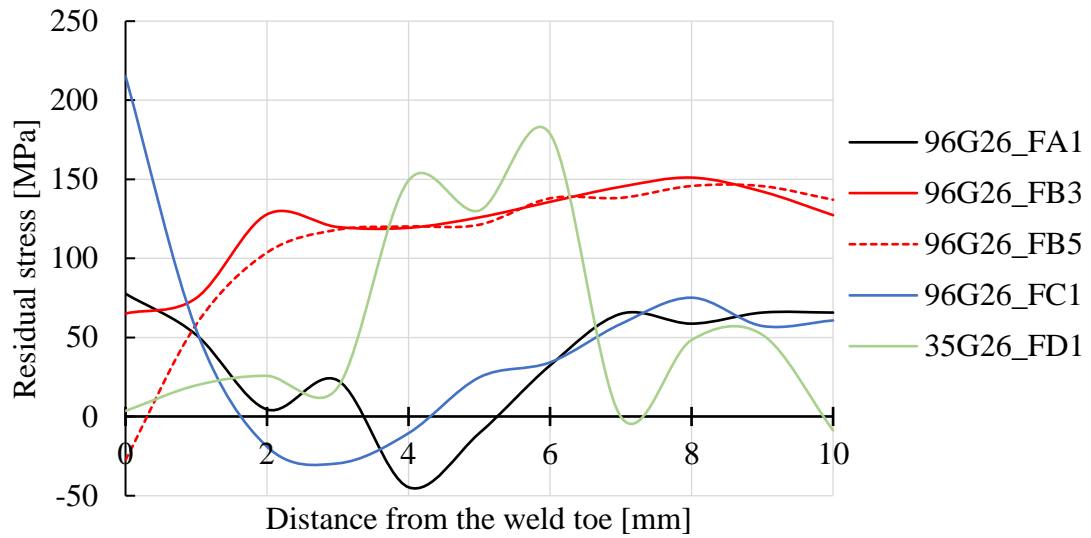
Figure 25. Residual stresses on the plate, measured from the weld toe.

The measured residual stress on the groove without HFMI treatment was about -80 MPa with a margin of error approximately ±50 MPa. Compressive residual stress is likely due to machining that is known to leave residual stresses, or the machining has redistributed internal residual stresses in the material. On the HFMI treated specimen measured residual stress was about -450 MPa and a margin of error approximately ±100 MPa. The purpose of HFMI is to leave a strong compression residual stress which can be as large as the yield strength of the treated material.

4.3 Quasi-static tensile tests

Quasi-static tests were performed by Gardabini Quasar 600 tensile test machine, which is driven by electro-mechanical gears and a screw system. Elongation is measured from the machine and with Aramis digital image correlation (DIC) system, because an extension meter was not available. DIC makes it possible to measure the deformations of solids without contact. In short, a speckle pattern is painted on the surface to be measured, from which images are taken during the deformation and the deformations on the measured surface are calculated from the images. Calculation is conducted by applying facets on speckle pattern and by tracking speckles in the facet, the deformation of the facet is calculated from each image and compared into the reference image. Strain calculation is common post-processing step, where strains are computed from the displacements. (LePage, 2022.)

During the tensile test, Aramis setup had two 12-megapixel cameras with 75 mm lenses were used with 24.8° angle to each other, both of which had an 85×65 mm capturing area. Both cameras were calibrated into the same point on the measured surface and images were taken with 6 Hz frequency during the test. Needed speckle pattern was painted into one side of the test specimen by painting area with white and then applying black paint droplets in the area. The applied facet size on analysis was 19 pixels and overlap between facets was 16 pixels. The force data during the test was read about force sensor of the tensile test machine and signal was sent into Aramis computer. After strain computation, a 50 mm long extension meter was applied over the weld and that was used to measure elongation. In Figure 26 can be seen the test setup with cameras and the applied extension meter on the computed surface.
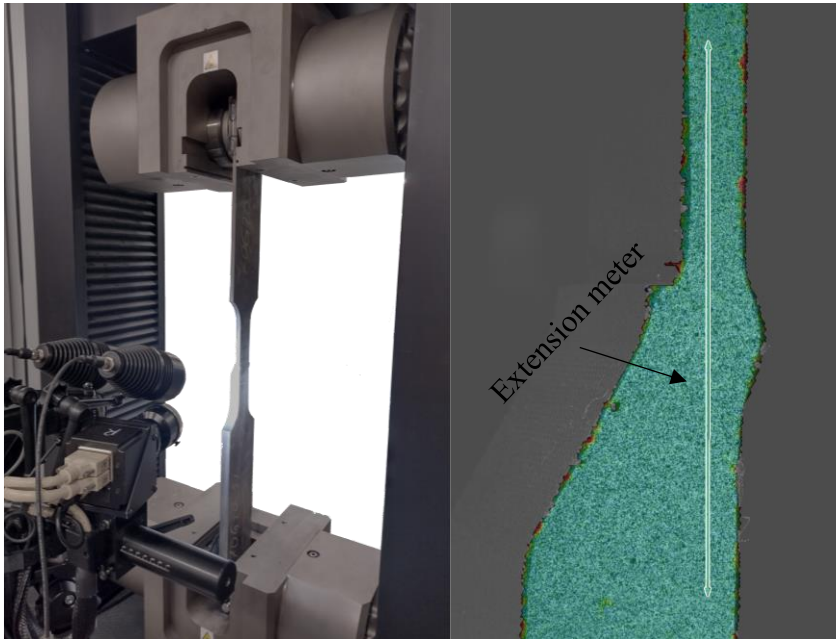
Figure 26. Quasi-static test setup, with Aramis digital image correlation cameras on the left. And on the right the applied 50 mm long extension meter over the weld.

From the tensile tests, 35G26_S1 and 11G26_S1 specimens broke from the base material of the plate and outside the capturing range of Aramis cameras, all other failures were captured. 70G20_S1-3 series was very brittle and one spare specimen was used to verify results. Otherwise, no errors were observed in the test arrangement. Tensile test results can be seen on Table 14. Yield strength at 0.2% elongation $f_{y,0.2}$ was solved graphically from measured data and because the extension meter was set over weld, the cast steel affected measured yielding strength. Other values that were extracted from the data were f_u ultimate or tensile strength, A_g elongation during maximum load without elastic region and A total elongation at failure.

Table 14. Tensile test results and, in parentheses, the nominal tensile strengths of the base material where the failure occurred.

Specimen ID.	f_y [MPa]	f_u [MPa]	A_g [%]	A [%]
35G26_S1	384	569 (500 – 650)	4.204	5.629
70G20_S1	626	671 (750 – 950)	0.505	0.715
70G20_S2	563	576 (750 – 950)	0.282	0.490
70G26_S1	708	815 (750 – 950)	3.395	3.684
96G26_S1	770	960 (980 – 1250)	1.456	3.120
11G26_S1	953	1156 (1250 – 1450)	2.618	4.074

Stress-strain curves from the tensile test can be seen in Figure 27 and from the curves can be observed that all the other specimens had ductile behaviour except specimens with S700 plate. G20Mn5 cast steel is on the graph with dashed lines.
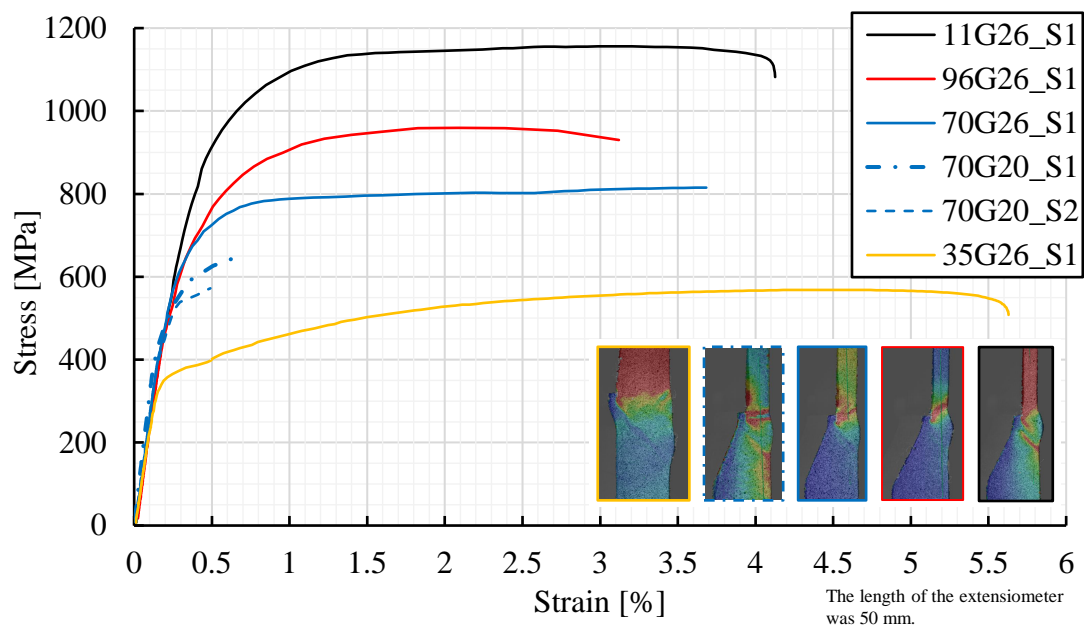

Figure 27. Stress-strain curve of the tensile test specimens. Solid lines are specimens with G26CrMo4 cast steel and dash lines with G20Mn5. At the right low corner can be seen small images about strains on the weld during maximum load.

35G26_S1 specimen had a ductile fracture on S355 plate base material and like previously mentioned, the failure happened outside of capturing area. The specimen and the weld withstood the load, which was expected of materials used. In the weld itself, only a small region with higher strain can be detected on the weld root and very small region on the weld

toe. In Figure 28 can be seen an image from the fracture surface, the position of the failure and the DIC image at the moment of maximum load.

Figure 28. The ductile fracture at 35G26_S1 specimen. Failure happened at S355 base material outside DIC capturing area and no high strain regions can be detected in weld area from DIC image.

Both 70G20_S1 and S2 specimens had very brittle fractures and had and plastic deformation ability was almost non-existent. Failures occurred way below the yield strength of S700, and this needed an additional test to verify if there was error on the test specimen or measurements. On both specimens, the failure happened on fusion line between the weld and S700 plate. In Figure 29, the fracture surface, the position of the failure and the last DIC image before failure can be seen. Two high strain lines can be detected in this image, one at fusion line where failure happened and other at the outer region of HAZ. Fracture surfaces of both 70G20_S1 and 70G20_S2 specimens can be seen on Appendix VI.
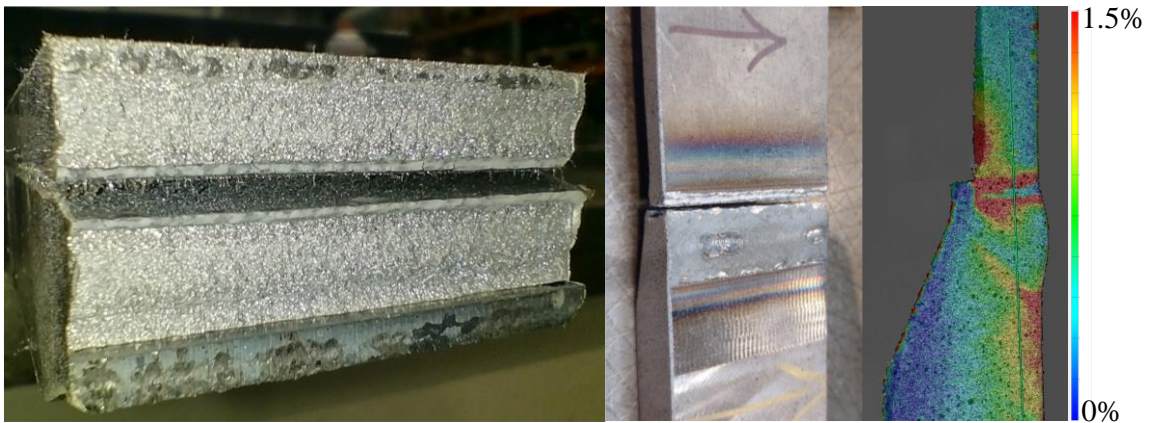
Figure 29. The brittle fracture at 70G20_S1 specimen. Failure happened fusion line between the weld and S700 plate. Two high strain lines can be detected in the weld area, one on fusion line where failure happened and other is at the outer HAZ region.

70G26_S1 specimen had a brittle fracture on S700 HAZ. The specimen and the weld withstood the load, which was expected of used materials. In Figure 30, the fracture surface, the position of the failure and the last DIC image before failure can be seen. On this specimen, the fracture surface is shifted almost into a maximum shear stress plane and the position of the failure can be seen as high strain line on DIC image.

Figure 30. The brittle fracture at 70G26_S1 specimen. Failure happened on S700 HAZ and one high strain line can be detected in failure location.

96G26_S1 specimen had a ductile fracture on a softened HAZ at S960 plate. In Figure 31 can be seen the fracture surface, the position of the failure and the DIC image at the moment of the maximum load. On the DIC image, no higher strains can be detected on the weld but necking and position of the future failure can be seen on high strain line at the softened HAZ.

The location of the failure matches with the softened region that was detected on hardness measurements (Appendix IV).

Figure 31. The ductile fracture at 96G26_S1 specimen. Failure happened in the softened HAZ at S960 plate. Necking and a high strain line can be detected in HAZ where failure happened.

11G26_S1 specimen had a ductile fracture on S1100 plate base material and like previously mentioned, the failure happened outside of capturing area. In Figure 32 can be seen an image from the fracture surface, the position of the failure and the DIC image at the moment of maximum load. On DIC image two higher strain lines can be detected on the weld area. One from the weld root, possibly following the fusion line and other from the weld toe on cast steel HAZ. Based on this tensile test result and hardness measurements (Appendix IV), S1100 is the only UHSS that did not deteriorate during welding.

Figure 32. The ductile fracture at 11G26_S1 specimen. Failure happened at S1100 base material outside DIC capturing area. In DIC image two higher stain regions can be detected, one from the weld root, possibly following the fusion line and other on cast steel HAZ.

Fracture samples were made from 70G20_S1 and 70G26_S1 specimens to compare drastic difference between specimens, that had the same S700 plate, additives, root geometry, welding parameters and welded in succession. In Figure 33 are both fracture samples and unbroken samples that were used on hardness measurements. The failure along the fusion line is usually an anomaly and no welding errors were detected in macro graphs or by visual inspection. Only difference between specimens was the cast steel material and the failure did not even occur on the cast steel side.
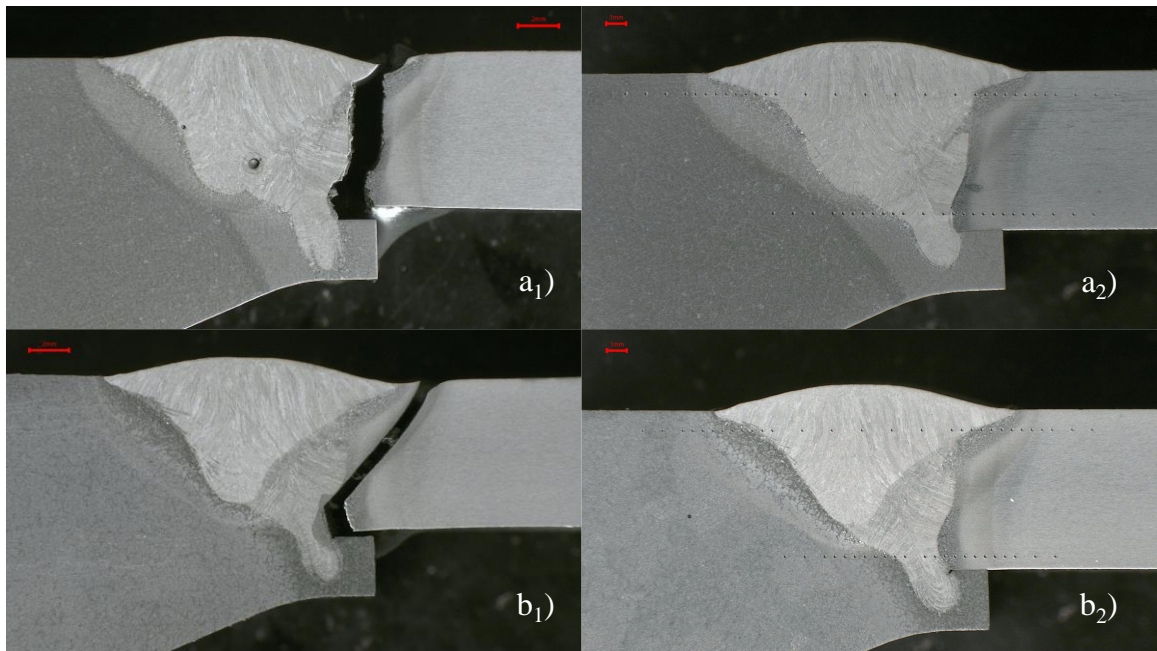
Figure 33. Macro graphs were made from fractures at 70G20_S1 (a_1) and 70G26_S1 (b_1) specimens. Unbroken cross sections of the welds that were used in hardness measurement 70G20_S1 (a_2) and 70G26_S1 (b_2).

5 Results

On this section is presented the results obtained by numerical optimization and experimental research.

5.1 Results of numerical analysis

A rough root geometry optimization on the welded joint between 20 mm thick cast steel with a permanent root backing and 8 mm thick UHSS plate without any misalignment (Figure 7) was analysed with three different fictitious radius modelling techniques, keyhole $\rho_f = 1$ mm, fillet $\rho_f = 1$ mm and U-notch $\rho_f = 0.05$ mm. On this analysis the location of the applied groove was systematically varied and SCFs were read from the fictitious radius of the weld root with a both membrane and bending unit loads and from the applied groove with only membrane load. Total amount of FEM models was 38 which also includes three reference models, one for each modelling technique. All calculated numerical values can be found from Appendix VII.

Figure 34 shows the place of the applied relief groove and how its position was determined during rough optimization. The same coordinate point was used as the origin in each analysis regardless of the root modelling technique. When interpreting the results, it is important to remember that regardless of the root modelling technique, a 1 mm radius was used in the groove from which the SCF was determined at the bottom of the groove.
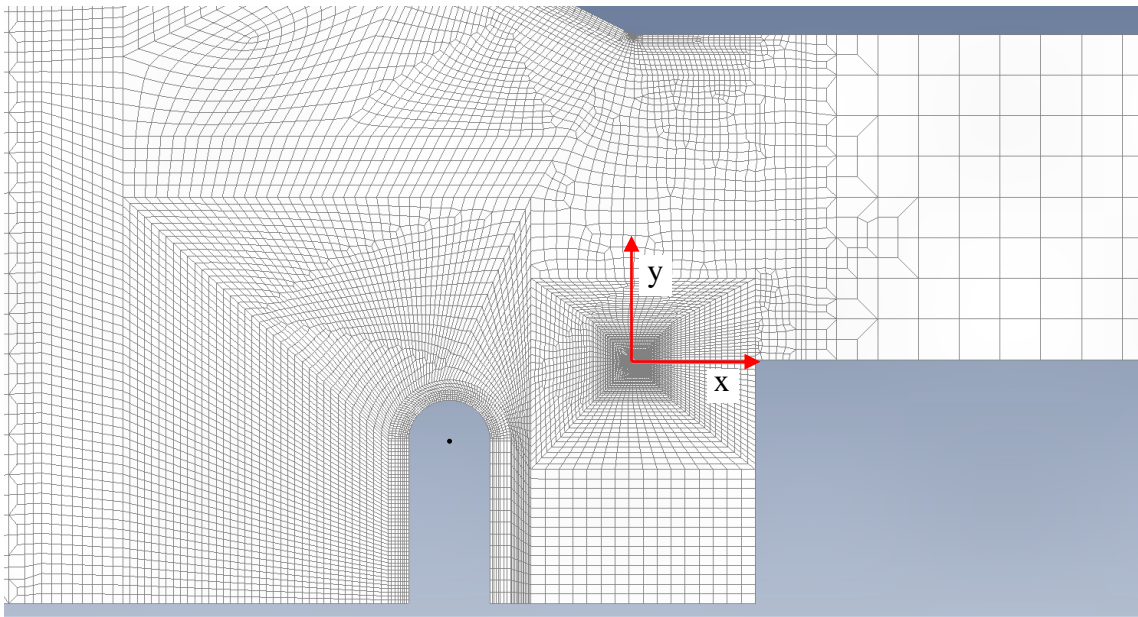
Figure 34. The origin of coordinate system was positioned into the corner of 8 mm plate and centre of the notch radius whose position was varied.

A rough groove location optimization on models with the fillet type fictitious radius, was performed with nine location variations. SCFs from the reference model (Ctrl) and optimizations (F1-F9) are presented in Figure 35 along with the groove position.

Figure 35. SCFs from the ENS model with a fillet type fictitious radius, at applied notch ($K_{t,n}$) and weld root with membrane ($K_{t,m}$) and bending ($K_{t,b}$) unit loads.

A rough groove location optimization on models with a keyhole type fictitious radius, was performed with six location variations. SCFs from the reference model (Ctrl) and optimizations (K1-K9) are presented in Figure 36 along with the groove position.
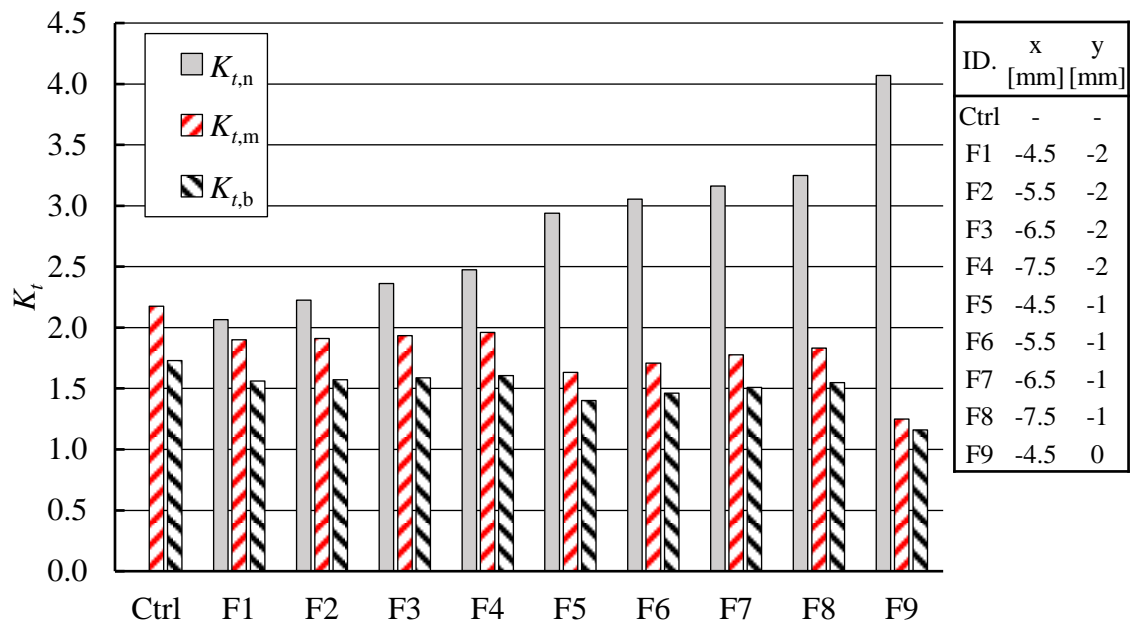

Figure 36. SCFs from the ENS model with a keyhole type fictitious radius, at applied notch ($K_{t,n}$) and weld root with membrane ($K_{t,m}$) and bending ($K_{t,b}$) unit loads.

A rough groove location optimization on models with a U-notch type fictitious radius, was performed with seven location variations. SCFs from the reference model (Ctrl) and optimizations (U1-U9) are presented in Figure 37 along with the groove position.
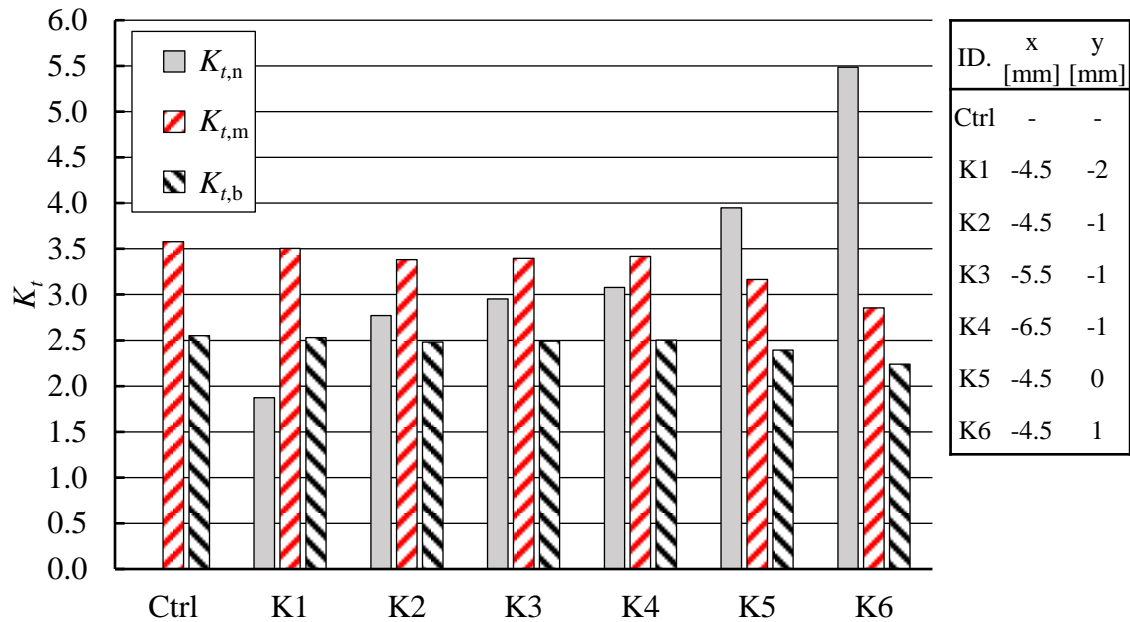
Figure 37. SCFs from the ENS model with a U-notch type fictitious radius, at applied notch ($K_{t,\text{n}}$) and weld root with membrane ($K_{t,\text{m}}$) and bending ($K_{t,\text{b}}$) unit loads.

In the second joint type, where the welded surfaces were aligned, the analysis was performed only with U-notch $\rho_f = 0.05$ mm modelling technique. The structure was analysed with membrane and bending load like on previous cases. In Figure 38 can be seen the applied U-notch groove whose position was varied on the rough optimization and the origin of the used coordinate system.
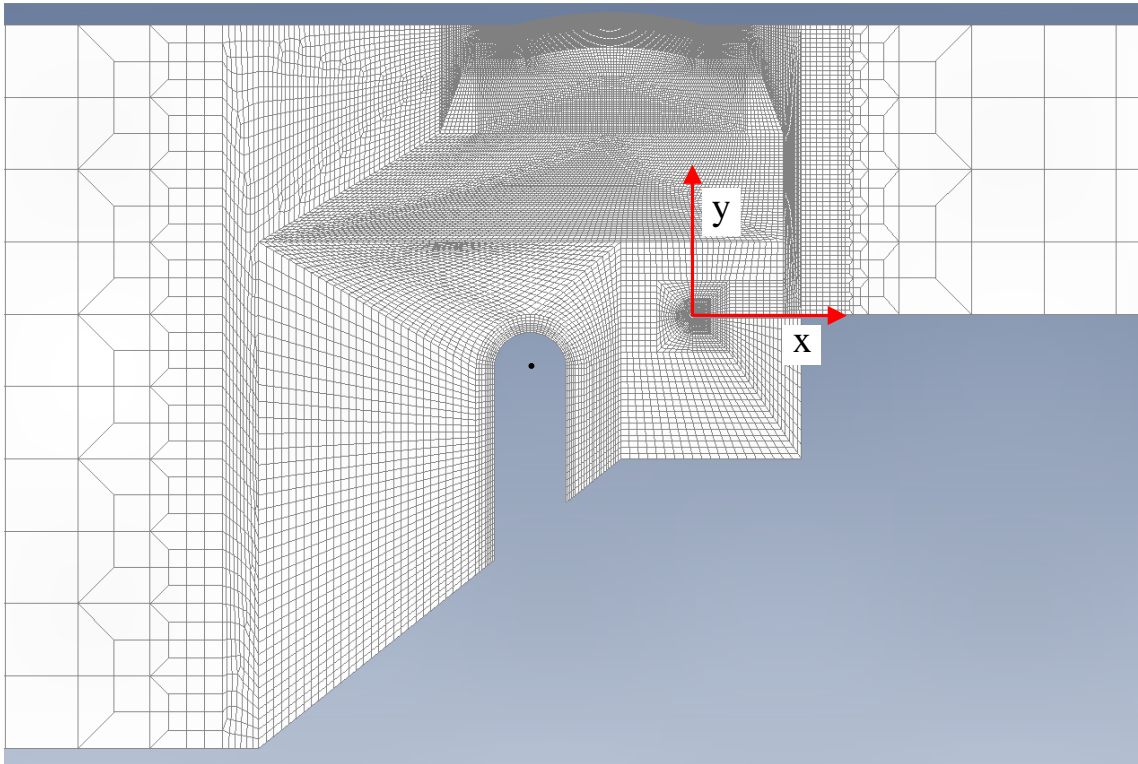
Figure 38. The origin of coordinate system was positioned into the corner of 8 mm plate and centre of the notch radius whose position was varied.

A rough groove location optimization on the joint type, where welded surfaces were aligned with a U-notch type fictitious radius, was performed with seven variations. SCFs from reference model (Ctrl) and optimizations (1-7) are presented in Figure 39. From these results variation no. 5 ($x = -4.0$, $y = -0.1$), was chosen for further development. With that groove geometry, the fatigue strength of the weld root and the added groove was calculated to be almost equal with 50 000 load cycles. Also, improvement in the weld root SCFs in terms of SCF at the applied groove was the best.
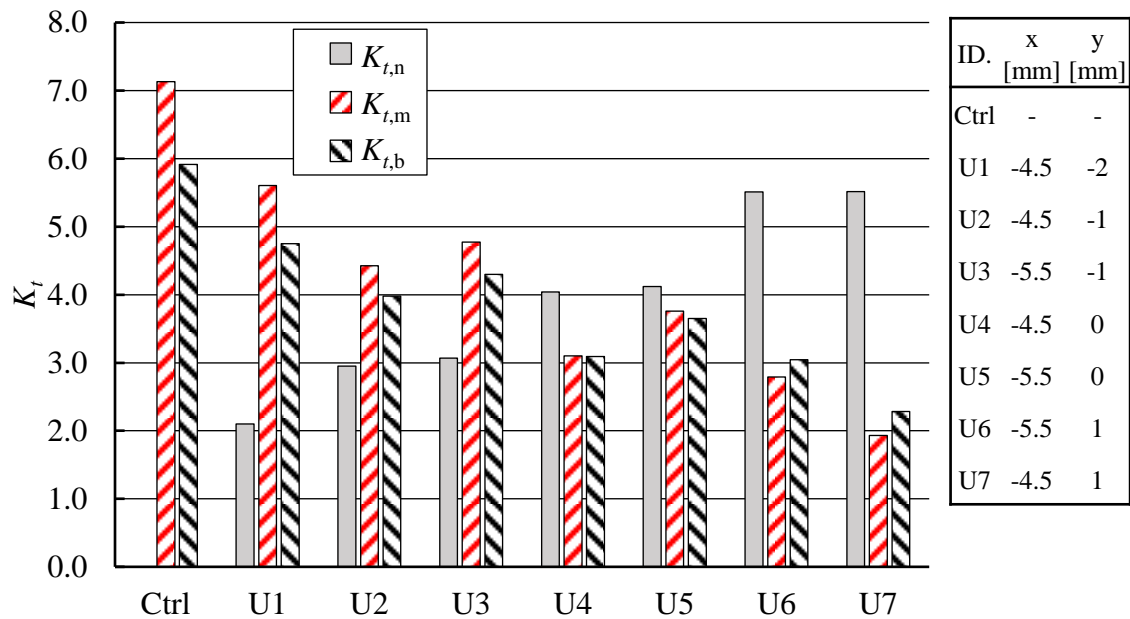
Figure 39. SCFs from the ENS model that has top surfaces aligned with a U-notch type fictitious radius, at applied notch ($K_{t,n}$) and weld root with membrane ($K_{t,m}$) and bending ($K_{t,b}$) unit loads.
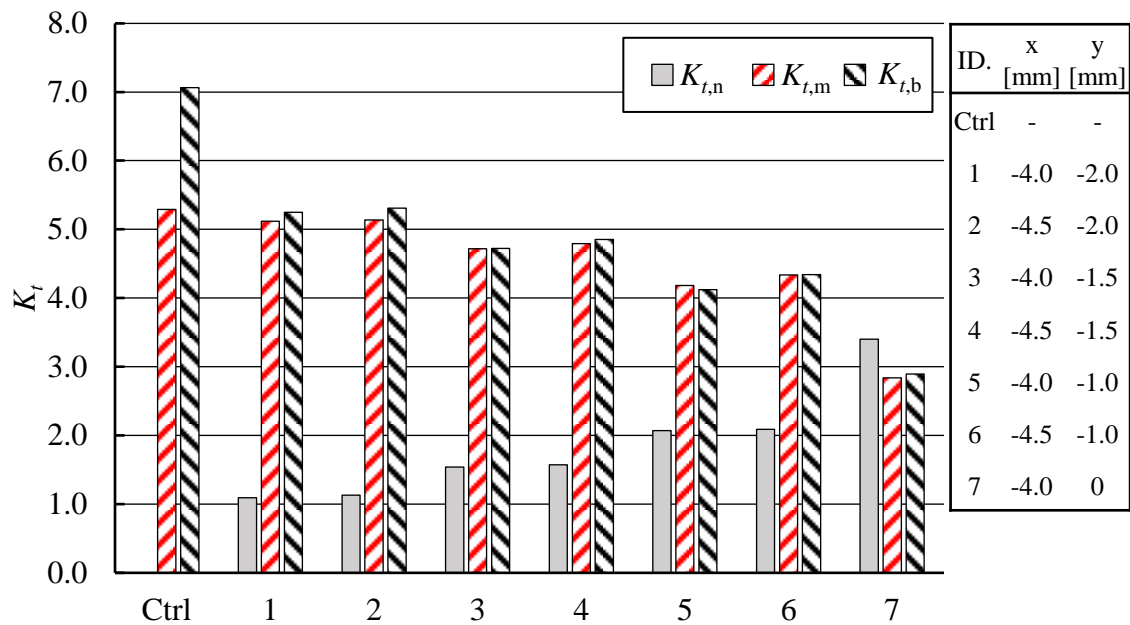
After the most effective position for the groove, based on the rough optimization had been found out, root geometry was smoothened. Due to welding, a 3 mm thick layer of material was left in the area of the weld root in all directions. Figure 40 shows the geometry of the rough optimization and smoothened geometry of the groove, as well as images of a few additional analyses, which tested different choices for the geometry of the groove bottom and the sensitivity of the design in relation to the length of the initial crack. Lastly, the functionality of the developed groove was tested on the welded joint with thinner (6 mm) plate which was used in an experimental study. SCFs from these analyses are presented in Figure 41 and from Appendix VIII, can be found exact dimensions of the designed relief groove.
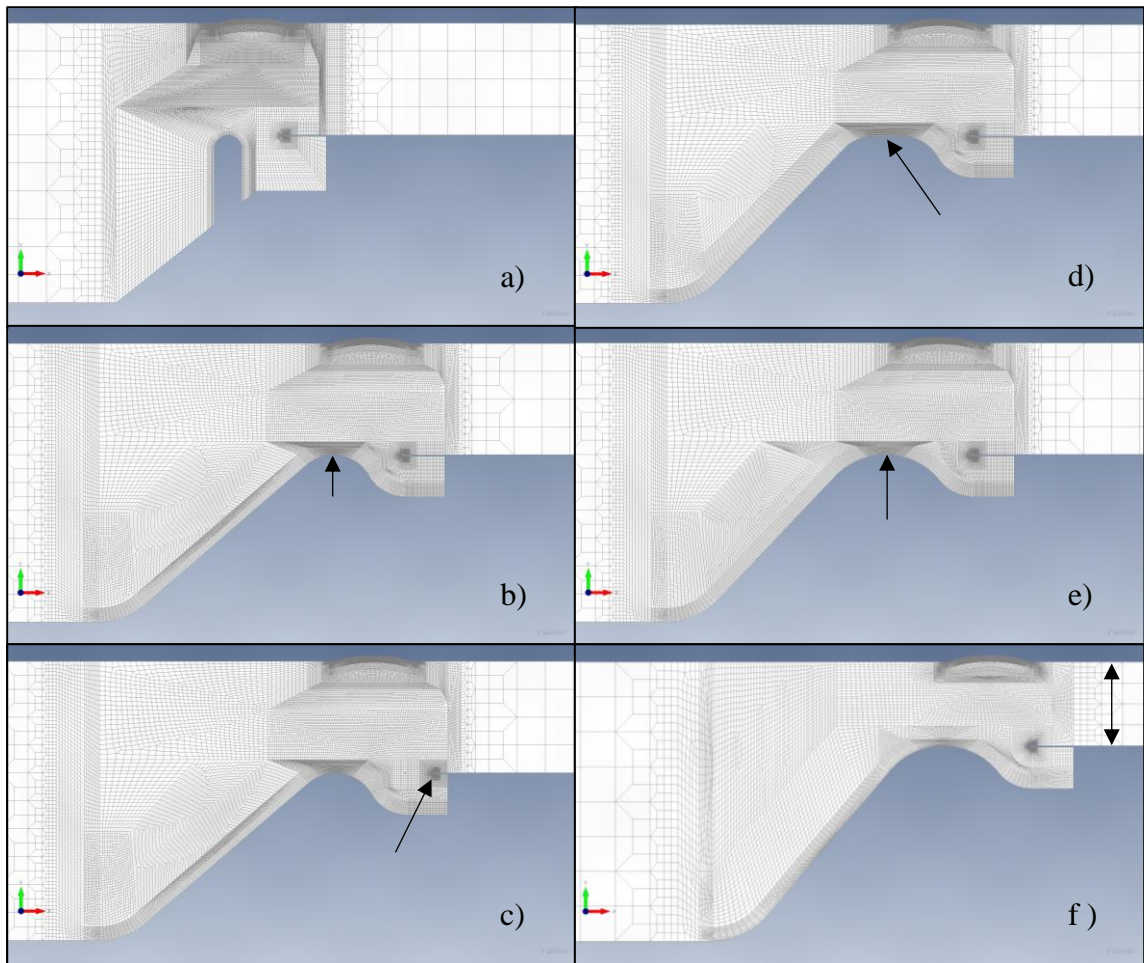
Figure 40. Root groove design based on rough optimization and some additional analyses: a) The result of the rough optimization. b) The U-notch groove was replaced with 3 mm rounding and smoothened shapes. c) Initial crack was shortened by 2 mm. d) The root groove was widened by 2 mm. e) Rounding at the root groove was increased to 5 mm. f) 8 mm thick plate was replaced with 6 mm thick one.
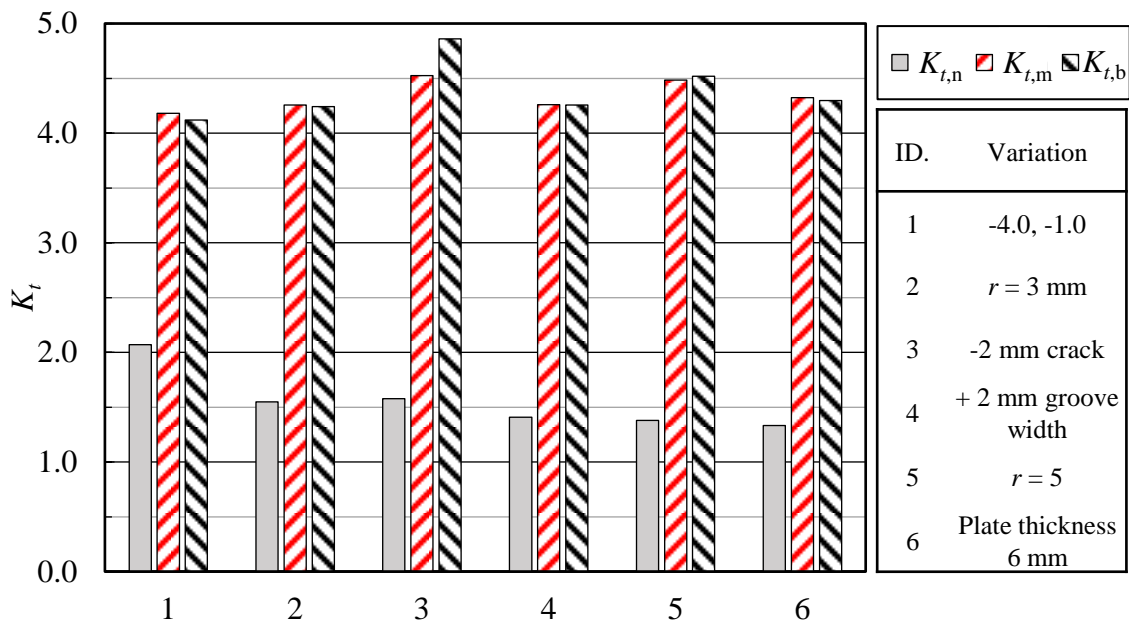
Figure 41. SCFs from a model which was chosen for further development (1.) and some additional analyses which were made to define final root geometry (6.).

5.2 Results of the fatigue tests

The purpose of the fatigue tests was to determine the effectiveness of the relief groove developed in Section 5.1 protecting the weld root from fatigue. Another goal was to develop a design S-N curve for that weld joint with the permanent root backing.

Fatigue tests for test series 96G26_FA, 96G26_FB and 96G26_FC were performed with a 750 kN servo-hydraulic rig designed and manufactured by the steel structure laboratory. The reason for this was the secondary bending stress due to the eccentricity of the joint, which causes lateral support reaction forces to the test rig. The fatigue test for 35G26_FD series was performed with commercial fatigue test rig Rumul Vibroforte 700, whose operating principle is dynamic vibration at the test specimen's characteristic frequency. The biggest advantage to use Rumul was the high fatigue speed compared with the servo-hydraulic test rig and straight pieces without eccentricity enabled the use of this test rig.

A total of 27 fatigue tests were performed and all the extra spare specimens were used after the official tests were completed. Results from 96G26_FA1 specimen were not used on any

analyses because during the test another test rig stopped the test and caused a major overload situation due to the common hydraulic pump, which caused considerable ≈ 340 µm plastic strain to the test piece. The official tests were conducted with stress ratio $R = 0.1$ and the spare specimens by $R = 0.5$. Raw fatigue test data and additional data can be found in Appendix IX. Fracture samples were taken from each test series and macro graphs were made from these samples. Images from these fractures can be seen in Figure 42. All specimens that were tested with servo-hydraulic test rig were fatigued until the specimen broke into two parts and on high frequency rig the test was stopped when characteristic frequency changed enough, and then pulled into two parts with a quasi-static test machine. Images from fracture surfaces can be found from Appendix X.
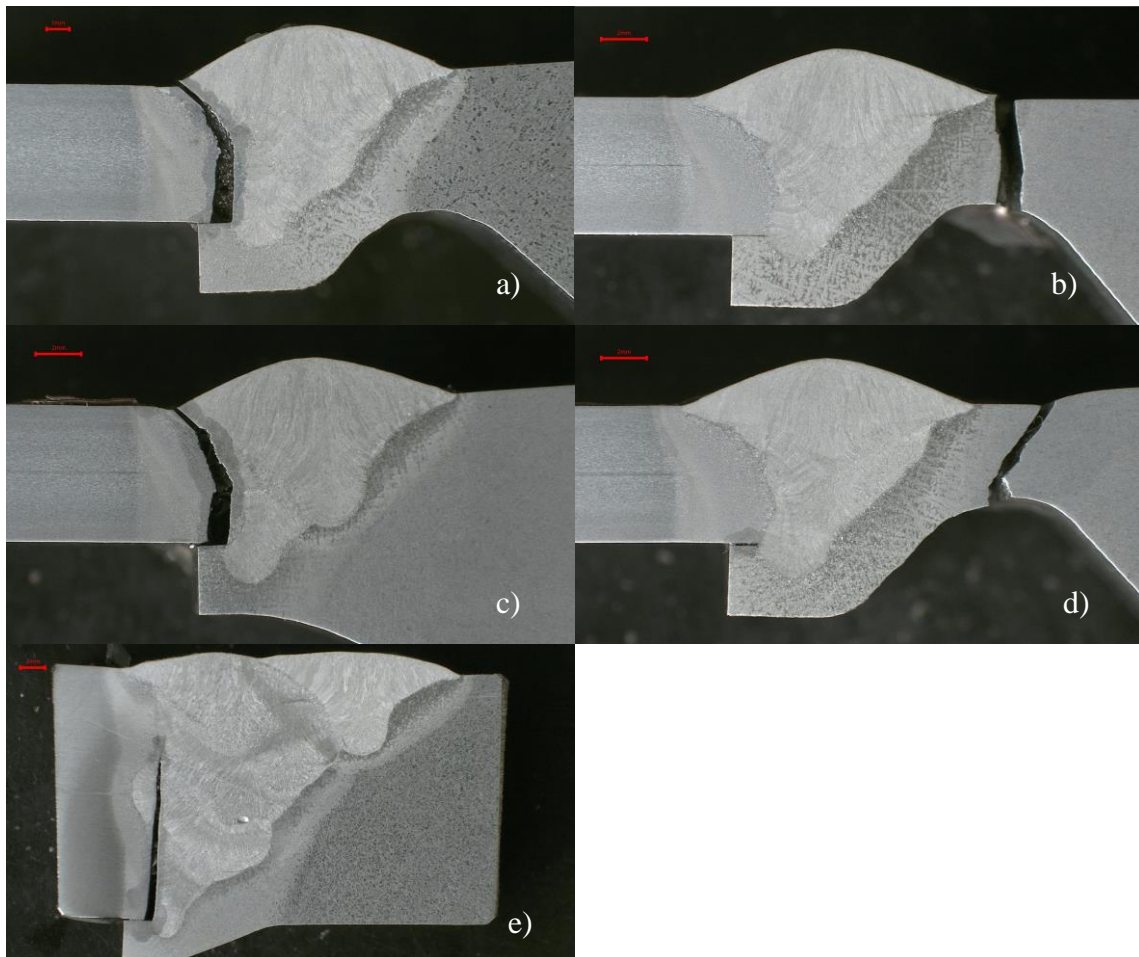

Figure 42. Macro graphs sections were made from fractures from each test series and variations. a) 96G26_FA5, b) 96G26_FB2, c) 96G26_FC5 d) 96G26_FB6 HFMI and e) 35G26_FD1.

In Table 15 are presented fitted S-N curves using the standard method for each test series using data from both $R = 0.1$ and 0.5 test specimens. The curve fitting was made using the nominal stress and a structural stress. The structural stress was calculated from the strain gauge measurements and the known nominal stress, because the boundary conditions of the test rig induced secondary bending stress in the fatigue test specimen with tensile stress, due eccentricity of the joint. The assumption that the bending moment remains the same over the weld was made, so that the structural stress at the bottom of the groove could be determined, with the available measurement data. In this assumption, the membrane stress was linearly and the bending was quadratically proportional over the weld. In the fitting of the curve to the 96G26_FA series, the 96G26_FA8 test specimen was left out, due to the divergent failure location. Graphs of the fitted curves and the results of each individual test series, with structural stress can be seen in Appendix XI.

Table 15. Fitted S-N curves for each test series using data from both $R = 0.1$ and 0.5 test specimens. Fitting was performed with nominal stress and structural stress.

Test series ID.	Number of specimens	m	Nominal stress		Structural stress	
			$\Delta\sigma_{f,50\%}$	$\Delta\sigma_{f,97.70\%}$	$\Delta\sigma_{f,50\%}$	$\Delta\sigma_{f,97.70\%}$
96G26_FA	6	3	64	53	99	80
96G26_FB	3	5	117	104*	171	162*
96G26_FB**	4	5	173	149*	217	207*
96G26_FC	8	3	53	44	96	82
35G26_FD	4	3	99	86*	99	85*

* Small sample size

**HFMI treated

It was noticed that the fatigue strength would be very similar to all specimens broken from the weld root when using structural stress. The S-N curve was fitted using all test specimens that failed at the weld root, the curve and data points are presented in Figure 43. The curve fitting was performed using a standard method using a total of 18 test specimens' data, where structural stress was used with $m = 3$ slope. This resulted in a mean curve with a nominal fatigue strength of 98 MPa and a characteristic curve with a fatigue strength of 84 MPa.
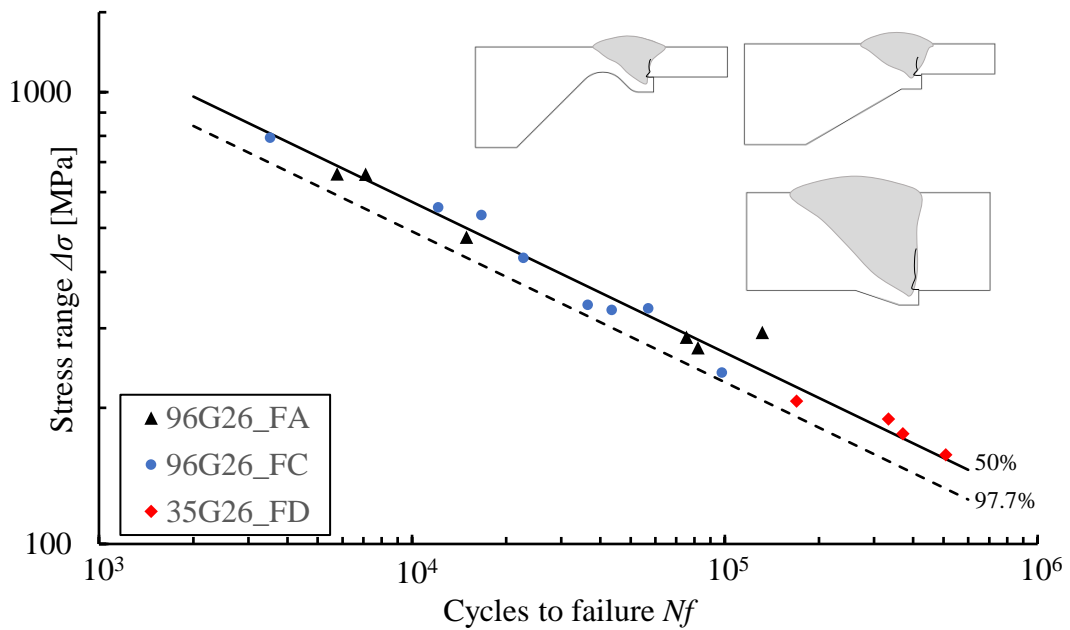
Figure 43. S-N curves ($m = 3$) fitted to data from all test specimens that broke at the weld root, a total of 18 specimens. Fatigue strength of the curves were 98 MPa and 84 MPa.

All specimens that failed from the bottom of the applied groove were also placed in the same graph along with fatigue strength curves from the weld root failure, and mean curves from both variations from 96G26_FB series, Figure 44.
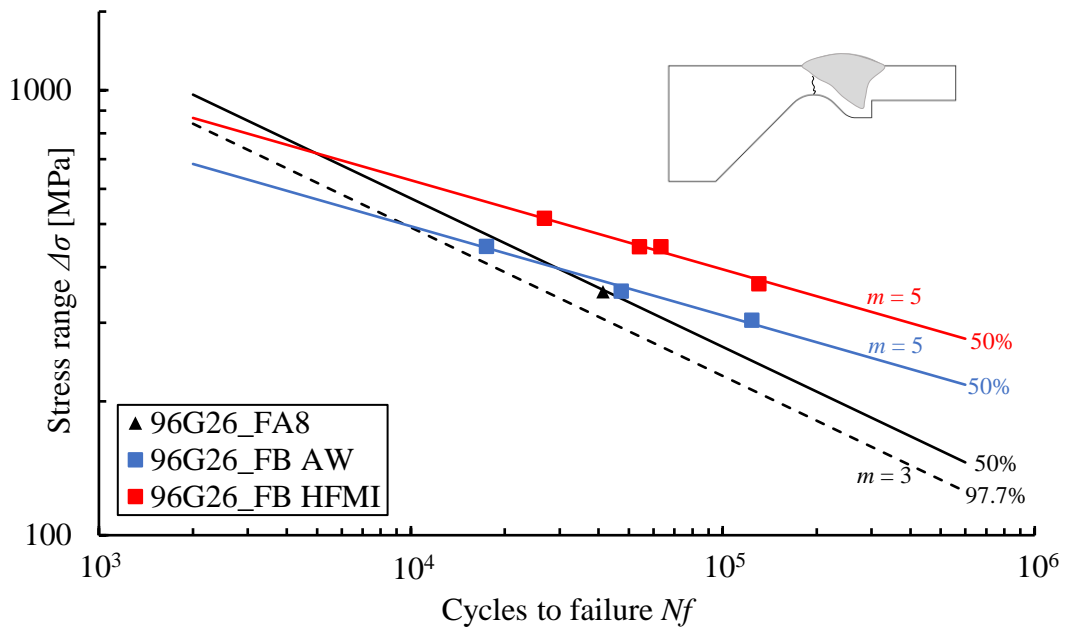
Figure 44. All data points from failures at cast steel base material along with fatigue strength curves 98 MPa and 84 MPa (*m* = 3) and mean fatigue strength curves from both 96G26_FB variations (*m* = 5).

In Appendix XII is presented the previous figure with data from each fatigue test specimen except 96G26_FA1.

6 Discussion

In this thesis, a welded joint between a cast iron part and a UHSS plate was investigated with experimental research and joint geometry optimization with FEM analyses. In the brief literature review, it was found that UHSS requires higher quality in the welding requires and just the right heat input so that the joint has good static strength and impact toughness.

6.1 Welding and material quality

The investigation of welding was not initially the focus of the thesis, because it was assumed that there were no problems with welding. Because of this, the measurements were somewhat lacking.

In the experimental study and in the welding of UHSS, softened HAZ region was observed in S700 and S960 plates, and strong hardening of the microstructure and martensite formation in the HAZ of G26CrMo4 cast steel. The approximately 10-15% softening in hardness was observed in the S700, about 30% in the S960 and insignificant decrease of hardness in S1100 after welding. Similar result has also been observed in other studies with similar heat inputs (Amraei et al., 2020, p. 3). Quasi-static tensile tests proved that S1100 was the only tested UHSS that did not deteriorate during the welding.

The drastic increase in hardness in the cast steel could be explained by the higher carbon content (0.26 %) and a possibly different cooling time than the calculated $t_{8/5}$ times. Different calculated and actual cooling times may be due to the thicker material's ability to absorb heat and act as a heat sink in a dissimilar joint. During welding, a clear difference in cooling times was observed between the different fatigue test pieces due to the applied relief groove in the cast steel, but no scientific measurement was performed. The use of a pyrometer during welding could have provided a lot of valuable information about the cooling time and heat flow in different variations of the welding joint geometry.

The weld joint of G20Mn5 and S700 broke along the fusion line of the weld and UHSS plate and the test was repeated with the same result. In general, failure along the weld's fusion line is an anomaly caused by an internal welding defect. In this case, no welding defects were found and nothing special was observed in the hardness measurements or the macro graphs, but in the quasi-static tensile test the ability to endure deformation was found to be almost non-existent. Additional tests to investigate the cause of the fusion line failure would have required extensive SEM and EDS inspections of the fracture surfaces, for which there was neither resources nor time in this thesis.

Signs of low material quality were observed in the G26CrMo4 cast steel base material. A lot of micro-voids were found in the casting base material, and the examination of the HAZ raised doubts about the lack of homogeneity in the chemical composition. In addition, a few large cavities filled with sand were found during the machining of the bevels and on HFMI treatment, Figure 45.
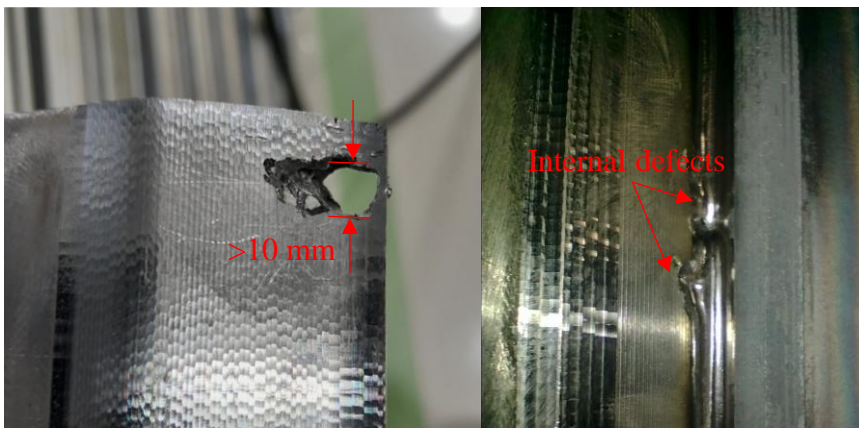
Figure 45. Internal defects detected in machining and HFMI treatment.

Although all test specimens were welded successfully, the sample size was very small with steels other than S960. The welding of these cast steels requires further research and understanding, especially the welding joint between S700 and G20Mn5 steels. There is also reason to doubt the material quality of S700 due fusion line failure. Impact tests could give more insight into the brittle weld joints. In addition, the quality of the casting materials must be monitored and examined because many of the observed defects are not acceptable or safe in the final product.

6.2 Analysis of results

In this thesis, based on the fatigue tests, a design curve was developed for the cast steel and UHSS weld detail, with permanent root backing. The design S-N curve was developed from the data of all the test pieces broken at the weld root of which there were 18 pieces in total, with a characteristic fatigue strength of 84 MPa (m =3). Currently, Eurocode 3 and IIW recommendations both advice to use fatigue class 71 for butt welds with permanent root backing (Hobbacher, 2016, p. 44; SFS-EN 1993-1-9, 2005, p. 24). These do not consider the eccentricity of the weld.

Numerically calculated, the relief groove should work, but the effect of the groove was not detected in the experimental study and all test specimens with the same fatigue failure location landed on the same S-N curve, when a structural stress criteria was used. The most likely reason is that the FEM modelling technique affects the SCF values more than expected and the fictitious radius of 0.05 mm emphasizes the SCF values in the weld root too much. Examining the results of the first weld detail (Figure 7), where was not any axial misalignment in the welded joint, it can be observed that the effect of the relief groove with the keyhole method is very minimal (Figure 36) compared to U-notch (Figure 37). Although the weld detail was different in the aforementioned models, a similar phenomenon may also occur in the experimentally studied geometry.

Instead, it was observed that the fatigue strength for all specimens that failed from the weld root was remarkably similar, Table 15. This led to the hypothesis that the relief groove affected the structural stress composition of the weld detail and reduced the proportion of bending. The same connection can be observed from the calculated DOB values. Average DOB values can be seen on Table 16, from which it can be observed that the DOB decreases when the relief groove is made deeper, HFMI treatment also seemed to affect the DOB values.

Table 16. Calculate average degree of bending from test specimens.

Test series and variation	DOB$_{avg}$
96G26_FA	0.35
96G26_FB AW	0.26
96G26_FB HFMI	0.16
96G26_FC	0.45

In the selection of optimized geometry for further development, the location of the relief groove was chosen so that failure at the weld root and base material failure at the groove would occur at the same time at 50 000 cycles. The failure location of the test specimen 96G26_FA8 was differed from the other specimens in the test series and the fatigue failure occurred in the base material in the relief groove. A macrograph and closer inspection revealed an approximately 1.1 mm long crack at the weld root, Figure 46. The S-N curves, which have been developed according to the failures of the weld root and the bottom of the relief groove, intersect at 30 000 - 50 000 cycle area (Figure 44) and this specimen lasted approximately 41000 cycles. Visual inspection did not reveal any other test specimens with two competing growing cracks.
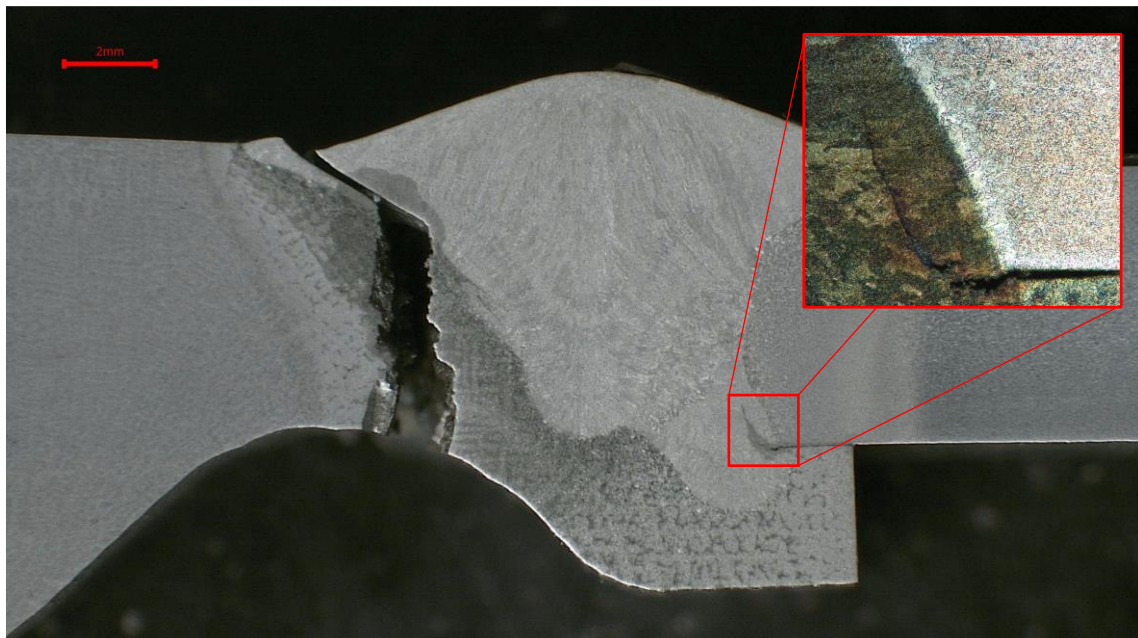

Figure 46. Fracture sample from specimen 96G26_FA8 with a 1.1 mm long crack in the weld root.

By making the designed relief groove even more aggressive, the failure location was transferred from the weld root into the base material of the casting. This made it possible to treat the failure location with HFMI and increase the fatigue life considerably. With this small sample size, mean nominal fatigue strength of the base material increased from 171 MPa to 217 MPa ($m = 5$) with HFMI treatment, which means 3.3 times improvement in fatigue life.

However, the determination of structural stress in the base material failure in cast steel is not very reliable, because the structural stress cannot be reliably calculated with the existing measurement data. The assumption that the bending moment across the weld is constant, was made, and the structural stress was calculated from the stresses on the strain gauge location.

6.3 Summary for the ideal solution

Based on the findings in this study, the best material selection would be G26CrMo4 and S1100. Promising results were also obtained with S960, but the welding parameters or the process still need to be adjusted in order to minimize the softened region of the HAZ. In G26CrMo4, was a lot of micro-voids and a few larger cavities full of sand, but it is mainly a matter of quality control. In addition, considerable hardening was observed in the HAZ, because of which the use of an elevated working temperature only for cast steel should be considered. A G20Mn5 and S700 combination cannot be recommended for use due fusion line brittle fracture and non-existent elongation capacity. Researched S700 plate should also be used with caution because the reason for the brittle fracture in the fusion line has not been clarified.

In terms of welding the permanent root backing should be slightly thicker so a larger heat input can be used, which enables a larger weld volume per pass. In a real structure the welded joint is always part of a larger structure that affects load compositions and boundary conditions. This means that the relief groove might not be relevant, as it affects the amount of secondary bending of the joint. However, in situations where fatigue strength of the weld is an issue and a small decrease in static load-bearing capacity is not crucial, an aggressive relief groove can be utilized by transferring the location of the fatigue failure to the base

material. When the location of the failure is transferred to the base material, a larger *FAT* class and S-N curve with $m = 5$ slope can be utilized, in which case fatigue resistance should increase considerably. In this case, post-treatment of the fatigue critical area is also possible.

In future, more tests are required to examine the mechanism where the location of the fatigue failure is moved away from the weld root and then HFMI treated. Also, the real structural stress in bottom of relief groove should be measured with additional tests.

7 Conclusions

In this thesis was investigated the fatigue of the initial crack, caused by the permanent root backing in cast steel, and the local optimization of the casting geometry with FEM and experimental research in order to improve the fatigue strength of the weld root. In addition, the welding of cast steel and UHSS dissimilar joints was briefly investigated with three different steel grades S700, S960 and S1100. The purpose was to investigate alternatives when traditional structural steels are replaced by significantly thinner UHSS with the same or better load-carrying capacity. Based on fatigue tests, other experiments and measurements done in this thesis, the following conclusions can be drawn:

- Current design recommendations are somewhat conservative for an eccentric butt joint with permanent root backing. The lowest obtained nominal mean fatigue strength for the joint was 96 MPa ($m = 3$) and the characteristic fatigue strength calculated from all specimens that failed from the weld root, was 84 MPa ($m = 3$).

- In the experimental study, it was not found that the optimized relief groove influences SFCs of the weld root. Instead, the location of the fatigue failure was successfully moved from the weld root into base material by aggressive groove. This enabled the new fatigue failure location to be treated with HFMI, which gave promising results for increasing fatigue strength of the welded joint, although the sample size was small.

- Of the studied UHSSs, S1100 and S960 appeared to be the most suitable for this application although S960 welding parameters needs to be developed to achieve maximum static load carrying capacity. Based on these results, the S700 cannot be recommended without further investigation, due the risk of the brittle fracture.

- Effective utilization of the full capacity of UHSS requires higher quality requirements for product design and manufacturing such as in welding. Further research on the subject is needed, especially in welding S700 to G20Mn5 cast steel. This same observation about quality has been made in other studies related to the topic (Lipiäinen et al., 2022, p. 1; Skriko, 2018, pp. 116–121).

- The quality of cast steel can be criticized based on this study, and the use of that steel cannot be recommended due to the safety risks caused by poor material quality. There is also reason to doubt the material quality of S700 due fusion line failure.

References

Afkhami, S. (2022). Information to my thesis [private e-mail].Receivers Juho Havia, Kalle Lipiäinen (cc) Sent 6.10.2022, 11.33 o'clock (GMT +2) Attachment: "Report(G26CrMo4).pptx".

Afkhami, S., Björk, T., & Larkiola, J. (2019). Weldability of cold-formed high strength and ultra-high strength steels. Journal of Constructional Steel Research, 158: Pp. 86–98. https://doi.org/10.1016/J.JCSR.2019.03.017

Ahola, A., Skriko, T., Lipiäinen, K., & Björk, T. (2021). On the weld root fatigue strength and improvement techniques for non-load-carrying transverse attachment joints with single-sided fillet welds and made of mild and ultra-high-strength steels. Engineering Structures, 249: 11 p. https://doi.org/10.1016/j.engstruct.2021.113373

Amraei, M., Afkhami, S., Javaheri, V., Larkiola, J., Skriko, T., Björk, T., & Zhao, X. L. (2020). Mechanical properties and microstructural evaluation of the heat-affected zone in ultra-high strength steels. Thin-Walled Structures, 157: 11 p. https://doi.org/10.1016/j.tws.2020.107072

Amraei, M., Ahola, A., Afkhami, S., Björk, T., Heidarpour, A., & Zhao, X.-L. (2019). Effects of heat input on the mechanical properties of butt-welded high and ultra-high strength steels. Engineering Structures, 198(June): 15 p. https://doi.org/10.1016/j.engstruct.2019.109460

Amraei, M., Skriko, T., Björk, T., & Zhao, X. L. (2016). Plastic strain characteristics of butt-welded ultra-high strength steel (UHSS). Thin-Walled Structures, 109: Pp. 227–241. https://doi.org/10.1016/j.tws.2016.09.024

Baumgartner, J., & Bruder, T. (2013). An efficient meshing approach for the calculation of notch stresses. Welding in the World, 57(1): Pp. 137–145. https://doi.org/10.1007/s40194-012-0005-3

Björk, T. (2022). FOSSA, Fossil-free Steel and Applications. Research plan. LUT-University, Not public.

Fricke, W. (2010). IIW Recommendations for the Fatigue Assessment by Notch Stress Analysis for Welded Structures. IIW-Doc. XIII-2240r2-08/XV-1289r2-08, 38 p.

Fricke, W. (2013). IIW guideline for the assessment of weld root fatigue. Welding in the World, 57(6): Pp. 753–791. https://doi.org/10.1007/s40194-013-0066-y

Guo, W., Li, L., Dong, S., Crowther, D., & Thompson, A. (2017). Comparison of microstructure and mechanical properties of ultra-narrow gap laser and gas-metal-arc welded S960 high strength steel. Optics and Lasers in Engineering, 91(April 2016): Pp. 1–15. https://doi.org/10.1016/j.optlaseng.2016.11.011

Hobbacher, A. F. (2016). Recommendations for Fatigue Design of Welded Joints and Components (2nd ed.). Springer Switzerland. 143 p. ISBN 978-3-319-23756-5 https://doi.org/10.1007/978-3-319-23757-2_8

Javidan, F., Heidarpour, A., Zhao, X. L., Hutchinson, C. R., & Minkkinen, J. (2016). Effect of weld on the mechanical properties of high strength and ultra-high strength steel tubes in fabricated hybrid sections. Engineering Structures, 118: Pp. 16–27. https://doi.org/10.1016/J.ENGSTRUCT.2016.03.046

Jonsson, B., Dobmann, G., Hobbacher, A., Kassner, M., & Marquis, G. (2016). IIW guidelines on weld quality in relationship to fatigue strength (1st ed.). Springer Switzerland. 115 p. ISBN 978-3-319-19197-3, https://doi.org/10.1007/978-3-319-19198-0

LePage, W. (2022). A Practical guide to DIC [web document]. [Referred: 22.12.2022]. Available: https://digitalimagecorrelation.org/#fundamentals

Lindqvist, A., & Nilsson, H. (2016). Effective notch stress analysis of transverse attachments in steel bridges. A parametric fatigue life assessment [web document]. [Referred: 5.10.2022] Master's Thesis, Göteborg, Sweden, Chalmers University of technology, Department of Civil and Enviromental Engineering. 62 p. Available: https://publications.lib.chalmers.se/records/fulltext/240080/240080.pdf

Lipiäinen, K., Ahola, A., Virolainen, E., Hirvi, A., & Björk, T. (2022). Fatigue strength of hot-dip galvanized S960 cut edges and longitudinal welds. Journal of Constructional Steel Research, 189(September): 11 p. https://doi.org/10.1016/j.jcsr.2021.107083

Lukkari, J., Kyröläinen, A., & Kauppi, T. (2016). Hitsauksen Materiaalioppi, Osa 2. Metallit ja niiden hitsattavuus, [In Finnish]. Suomen hitsausteknillinen yhdistys ry. 364 p. ISBN 978-951-98212-5-2

Mikkonen, P., Björk, T., & Skriko, T. (2017). Ultralujien terästen ominaisuudet lopputuotteeseen osaavan suunnittelun ja valmistuksen avulla, [In Finnish]. Hitsaustekniikka, 1/2017, Pp. 26–30.

Radaj, D., Sonsino, C. M., & Fricke, W. (2006). Fatigue assesment of welded joints by local approaches (2nd ed.). Woodhead publishing Ltd. 639 p. ISBN 978-1-84569-188-2

Scopus. (2023). Scopus - Analyze search results, search sentence "Ultra-high-strenght steel." [web database]. [Referred: 4.1.2023] Avabaile: https://www.scopus.com/term/analyzer.uri?sid=fb81e310671ff21d47fa18eddcb249f3 &origin=resultslist&src=s&s=TITLE-ABS-KEY%252528%252522Ultra-high-strength+steel%252522%252529&sort=plf-f&sdt=cl&sot=b&sl=42&count=2090&analyzeResults=Analyze+results&cluster=sco subtype%25

SFS-EN 10025-2. (2019). Hot rolled products of structural steels. Part 2: Technical delivery conditions for non-alloy structural steels (2nd ed.). Finnish Standards Association SFS. 40 p.

SFS-EN 1011-2. (2001). Welding – Recommendations for welding of metallic materials. Part 2: Arc welding of ferritic steels (1st ed.). Finnish Standards Association SFS. 59 p.

SFS-EN 10149-2. (2013). Hot rolled flat products made of high yield strength steels for cold forming. Part 2: Technical delivery conditions for thermomechanically rolled steels (2nd ed.). Finnish Standards Association SFS. 14 p.

SFS-EN 10293. (2015). Steel castings – Steel castings for general engineering uses (2nd ed.). Finnish Standards Association SFS. 20 p.

SFS-EN 1993-1-9. (2005). Eurocode 3 – Design of steel structures – Fatigue (1st ed.). Finnish Standards Association SFS. 37 p.

SFS-EN ISO 15614-1 + A1. (2019). Specification and qualification of welding procedures for metallic materials – Welding procedure test. Part 1: Arc and gas welding of steels and arc welding of nickel and nickel alloys (1st ed.). Finnish Standards Association SFS. 9 p.

Siltanen, J., Skriko, T., & Björk, T. (2016). Eggect of the welding process and filler material on the fatigue behavior of 960 MPa structural steel at a butt joint configuration. Journal of Laser Applications, 28(2), Pp.1–9. https://doi.org/https://doi.org/10.2351/1.4943993

Skriko, T. (2018). Dependence of manufacturing parameters on the performance quality of welded joints made of direct quenched ultra-high-strength steel. Lappeenranta University of technology. 121 p. ISBN 978-952-335-267-4. https://lutpub.lut.fi/handle/10024/158538

Skriko, T., Lipiäinen, K., Ahola, A., Mettänen, H., & Björk, T. (2021). Fatigue strength of longitudinal load-carrying welds in beams made of ultra-high-strength steel. Journal of Constructional Steel Research, 179: 10 p. https://doi.org/10.1016/j.jcsr.2021.106563

Sperle, J.-O. (2012). Environmental Advantages of using Advanced High Strength Steel in Steel Constructions. Oslo, Norway. 5-7.9.2012. Nordic Steel Construction Conference, 11 p. https://www.researchgate.net/publication/267664666

SSAB. (2022). Strong finish to a record year. In Year-end report 2021 [web document]. [Referred: 1.8.2022]. PDF Available: https://mb.cision.com/Main/980/3494110/1526446.pdf

Steimbreger, C., Gubeljak, N., Vuherer, T., Enzinger, N., Ernst, W., & Chapetti, M. (2022). Effect of welding processes on the fatigue behaviour of ultra-high strength steel butt-welded joints. Engineering Fracture Mechanics, 275(October): 22 p. https://doi.org/10.1016/j.engfracmech.2022.108845

Tümer, M., Schneider-Bröskamp, C., & Enzinger, N. (2022). Fusion welding of ultra-high strength structural steels – A review. Journal of Manufacturing Processes, 82(May): Pp. 203–229. https://doi.org/10.1016/j.jmapro.2022.07.049

Van Vlack, L., Riegger, O., & Warrick, R. (1958). Sulphite Inclusions in Steel [web document]. [Referred: 7.12.2022] PDF Available: https://old.foundrygate.com/upload/artigos/Sulphite Inclusions in Steel.pdf

Appendices

Appendix I: G26CrMo4 material analysis

LUT Kone Hitsaustekniikka

Sample Identification

Quality   SampleNo G26CrMo4   Customer

	C	Si	Mn	P	S	Cr	Mo	Ni	Cu	Al
	%	%	%	%	%	%	%	%	%	%
1.	0.264	0.350	0.831	<0.0050	<0.150	0.953	0.176	0.037	0.015	0.074
2.	0.257	0.331	0.836	<0.0050	<0.150	0.948	0.178	0.021	0.013	0.068
3.	0.262	0.321	0.825	<0.0050	<0.150	0.946	0.177	0.017	0.012	0.065
4.	0.260	0.315	0.819	<0.0050	<0.150	0.939	0.178	0.016	0.012	0.065
Ø	**0.261**	**0.329**	**0.828**	**<0.0050**	**<0.150**	**0.946**	**0.177**	**0.023**	**0.013**	**0.068**
σ	0.0030	0.015	0.0074			0.0058	0.0010	0.0097	0.0014	0.0042
υ	1.149	4.559	0.894			0.613	0.565	42.17	10.77	6.176

	As	B	Bi	Ce	Co	Mg	N	Nb	Pb	Sb
	%	%	%	%	%	%	%	%	%	%
1.	0.0097	<0.0010	<0.010	<0.0050	<0.0050	<0.0050	0.078	0.0079	0.012	<0.010
2.	0.0095	<0.0010	<0.010	<0.0050	<0.0050	<0.0050	0.079	0.0081	<0.010	<0.010
3.	0.0093	<0.0010	<0.010	<0.0050	<0.0050	<0.0050	0.079	0.0078	<0.010	<0.010
4.	0.0097	<0.0010	<0.010	<0.0050	<0.0050	<0.0050	0.075	0.0084	<0.010	<0.010
Ø	**0.0095**	**<0.0010**	**<0.010**	**<0.0050**	**<0.0050**	**<0.0050**	**0.078**	**0.0080**	**0.011**	**<0.010**
σ	0.00020						0.0019	0.00027	0.0012	
υ	2.105						2.436	3.375	10.91	

	Sn	Ta	La	Ti	V	W	Zn	Zr	Se	Fe
	%	%	%	%	%	%	%	%	%	%
1.	<0.0050	<0.030	0.0044	0.0035	0.0057	<0.010	<0.0020	<0.0020	<0.0050	96.93
2.	<0.0050	<0.030	0.0046	0.0033	0.0055	<0.010	<0.0020	<0.0020	<0.0050	96.98
3.	<0.0050	<0.030	0.0039	0.0032	0.0055	<0.010	<0.0020	<0.0020	<0.0050	97.01
4.	<0.0050	<0.030	0.0041	0.0033	0.0056	<0.010	<0.0020	<0.0020	<0.0050	97.04
Ø	**<0.0050**	**<0.030**	**0.0043**	**0.0033**	**0.0056**	**<0.010**	**<0.0020**	**<0.0020**	**<0.0050**	**96.99**
σ			0.00032	0.00013	0.00010					0.047
υ			7.442	3.939	1.786					0.048

Appendix II: G20Mn5 material analysis
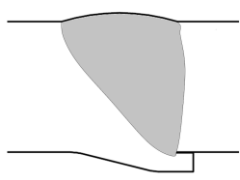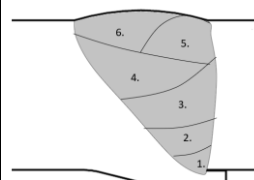
LUT Kone Hitsaustekniikka

	Sample Identification								
Quality				SampleNo G20Mn5			Customer		

	C %	Si %	Mn %	P %	S %	Cr %	Mo %	Ni %	Cu %	Al %
1.	0.189	0.382	1.188	<0.0050	<0.150	0.087	0.025	0.060	0.016	0.032
2.	0.178	0.354	1.192	<0.0050	<0.150	0.077	0.024	0.024	0.014	0.030
3.	0.179	0.353	1.192	<0.0050	<0.150	0.074	0.024	0.018	0.014	0.029
4.	0.175	0.353	1.192	<0.0050	<0.150	0.072	0.023	0.013	0.014	0.027
Ø	0.180	0.360	1.191	<0.0050	<0.150	0.077	0.024	0.029	0.014	0.029
σ	0.0061	0.014	0.0020			0.0067	0.00082	0.021	0.0012	0.0022
υ	3.389	3.889	0.168			8.701	3.417	72.41	8.571	7.586

	As %	B %	Bi %	Ce %	Co %	Mg %	N %	Nb %	Pb %	Sb %
1.	0.011	0.0011	<0.010	<0.0050	<0.0050	<0.0050	0.085	0.0079	<0.010	<0.010
2.	0.0095	<0.0010	<0.010	<0.0050	<0.0050	<0.0050	0.058	0.0078	<0.010	<0.010
3.	0.010	<0.0010	<0.010	<0.0050	<0.0050	<0.0050	0.052	0.0089	<0.010	<0.010
4.	0.0096	<0.0010	<0.010	<0.0050	<0.0050	<0.0050	0.049	0.0078	<0.010	<0.010
Ø	0.010	<0.0010	<0.010	<0.0050	<0.0050	<0.0050	0.061	0.0081	<0.010	<0.010
σ	0.00069	0.00006					0.016	0.00054		
υ	6.900	6.000					26.23	6.667		

	Sn %	Ta %	La %	Ti %	V %	W %	Zn %	Zr %	Se %	Fe %
1.	<0.0050	<0.030	0.0045	0.0051	<0.0050	<0.010	<0.0020	<0.0020	<0.0050	97.65
2.	<0.0050	<0.030	0.0040	0.0040	<0.0050	<0.010	<0.0020	<0.0020	<0.0050	97.76
3.	<0.0050	<0.030	0.0044	0.0042	<0.0050	<0.010	<0.0020	<0.0020	<0.0050	97.78
4.	<0.0050	<0.030	0.0036	0.0037	<0.0050	<0.010	<0.0020	<0.0020	<0.0050	97.80
Ø	<0.0050	<0.030	0.0041	0.0043	<0.0050	<0.010	<0.0020	<0.0020	<0.0050	97.75
σ			0.00041	0.00061						0.067
υ			10.00	14.19						0.069

Appendix III: Used WPS documents
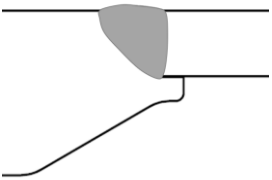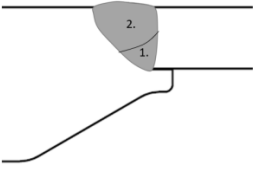
pre Welding Procedure Specification pWPS

Parent material	G26CrMo4/S355		
Material thickness	20mm/20mm	Joint type	Welding sequences
Outside diameter	-		
Welding process	135		
Welding position	PA		
Groove preparation	Machined		
Groove cleaning	Pickling		
Workpiece fixturing	Clamped		
Tack welding	-		
Back gouging	-		
Backing	Root support		

	Designation of consumables and trade name	Torch angle	1. 20° 2.-6. 0°
Filler material classification	ISO 14341-A-G 46 3M G 4Si1	Inclination angle	5°
		Distance contact tube to workpiece	1. 21 mm 2-6. 18 mm
		Preheating and interpass temperature	
Filler material trade name	OK Autorod 12.63 Esab	Preheat temperature	20°C room temperature
		Interpass temperature	100°C
Flux	-	Preheating method	-
Shielding gas	Awomix 8	Temperature measurement	Digital pyrometer
Flow rate	15 l/min	Post-weld heat treatment	
Plasma gas	-	Method	-
Flow rate	-	Heating rate	-
Backing gas	-	Temperature	-
Flow rate	-	Time	-
Type of current	DC+	Cooling rate	-
Polarity		Post-weld treatment	-

Remarks: Date and name:

Run	Process	Size of filler metal Ø (mm)	Current (A)	Voltage (V)	Travel speed (mm/s)	Wire feed rate (m/min)	Heat input (kJ/mm)	Run-out length (mm)	Weaving frequency (Hz)	Amplitude (mm)	Remarks
1.	135	1	220-225	24.3	7	10	0.66				
2.	135	1	255-265	25.4	3	11.5	1.87				
3.	135	1	250-255	25.4	2,7	11.5	1.04				
4-6	135	1	235-250	25.4	3.8	11.5	1.42				

Customer   Approved
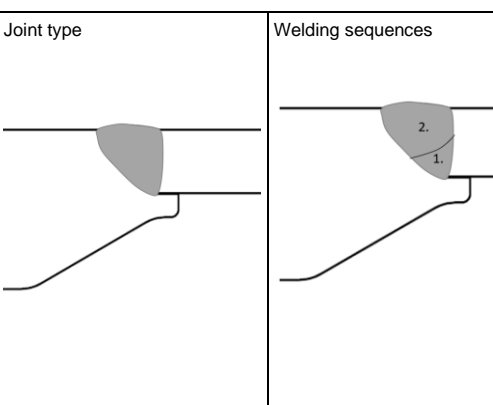
Appendix III: Used WPS documents

pre Welding Procedure Specification   pWPS

Parent material	(G26CrMo4/G20Mn5) S700		
Material thickness	20mm/8mm	Joint type	Welding sequences
Outside diameter	-		
Welding process	135		
Welding position	PA		
Groove preparation	Machined		
Groove cleaning	Pickled		
Workpiece fixturing	Clamped		
Tack welding	-		
Back gouging	-		
Backing	Root support		

	Designation of consumables and trade name	Torch angle	1. 25° 2. 0°
Filler material classification	ISO 16834-A-G 69 4 M Mn3NiCrMo	Inclination angle	5°
		Distance contact tube to workpiece	16 mm
		Preheating and interpass temperature	
Filler material trade name	OK AristoRod 69	Preheat temperature	20°C Room temperature
		Interpass temperature	50°C
Flux	-	Preheating method	-
Shielding gas	Awomix 8	Temperature measurement	Digital pyrometer
Flow rate	15 l/min	Post-weld heat treatment	
Plasma gas	-	Method	-
Flow rate	-	Heating rate	-
Backing gas	-	Temperature	-
Flow rate	-	Time	-
Type of current	DC+	Cooling rate	-
Polarity		Post-weld treatment	-

Remarks:	Date and name:

Run	Process	Size of filler metal Ø (mm)	Current (A)	Voltage (V)	Travel speed (mm/s)	Wire feed rate (m/min)	Heat input (kJ/mm)	Run-out length (mm)	Weaving frequency (Hz)	Amplitude (mm)	Remarks
1.	135	1	270-280	25.4	8.5	11.5	0.66				Torch 25°
2.	135	1	270-280	25.4	5	12	1.11				Torch 0°

Customer	Approved

Appendix III: Used WPS documents

pre Welding Procedure Specification   pWPS

Parent material	G26CrMo4, S960 & S1100		
Material thickness	20mm/6mm	Joint type	Welding sequences
Outside diameter	-		
Welding process	135		
Welding position	PA		
Groove preparation	Machined		
Groove cleaning	Pickled		
Workpiece fixturing	Clamped		
Tack welding	-		
Back gouging	-		
Backing	Root support		

	Designation of consumables and trade name	Torch angle	1. 25° 2. 0°
Filler material classification	EN ISO 16834-A : G 89 4 M Mn4Ni2CrMo	Inclination angle	5°
		Distance contact tube to workpiece	16 mm
		Preheating and interpass temperature	
Filler material trade name	OK Aristorod 89	Preheat temperature	20°C Room temperature
		Interpass temperature	50°C
Flux	-	Preheating method	-
Shielding gas	Awomix 8	Temperature measurement	Digital pyrometer
Flow rate	15 l/min	Post-weld heat treatment	
Plasma gas	-	Method	-
Flow rate	-	Heating rate	-
Backing gas	-	Temperature	-
Flow rate	-	Time	-
Type of current	DC+	Cooling rate	-
Polarity	-	Post-weld treatment	-

Remarks:

Date and name:

Run	Process	Size of filler metal Ø (mm)	Current (A)	Voltage (V)	Travel speed (mm/s	Wire feed rate (m/min)	Heat input (kJ/mm)	Run-out length (mm)	Weaving frequency (Hz)	Amplitude (mm)	Remarks
1	135	1	230-240	24.1	7.3	10	0.7	25			Torch 25°
2	135	1	250-260	25.8	6.5	12	0.88	25			Torch 0°

Customer

Approved

Appendix IV: Hardness measurements from quasi-static tensile test specimens
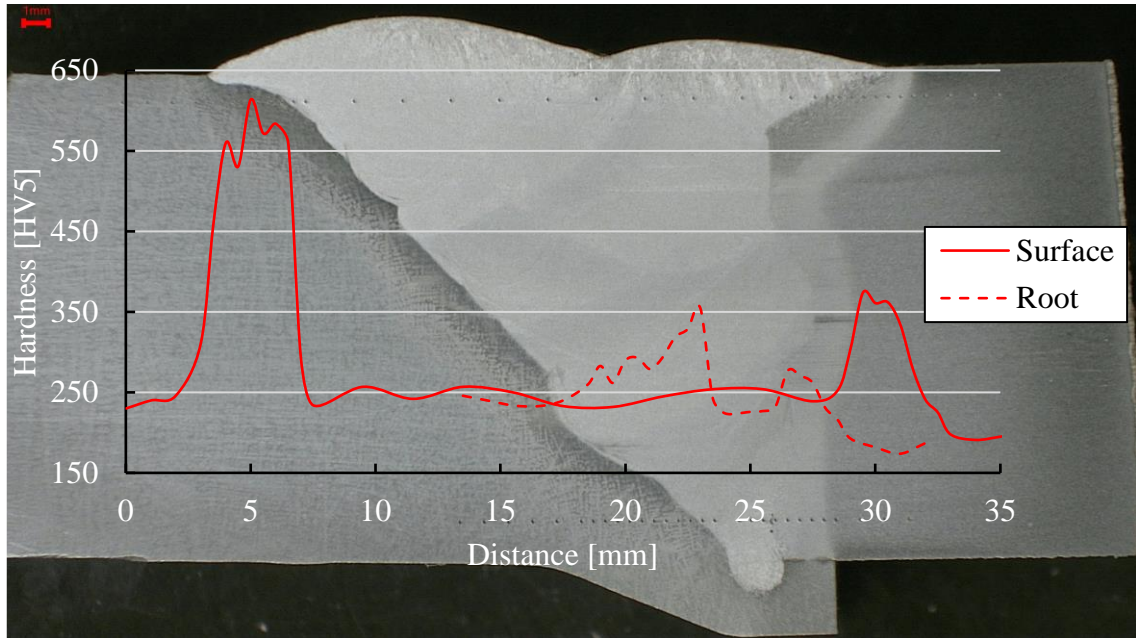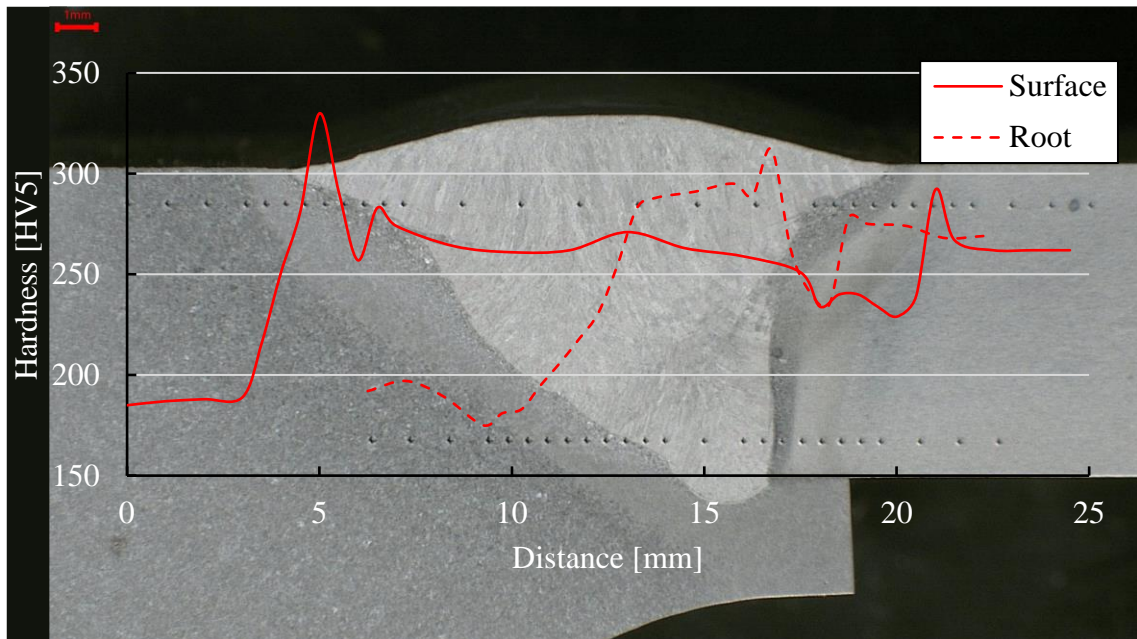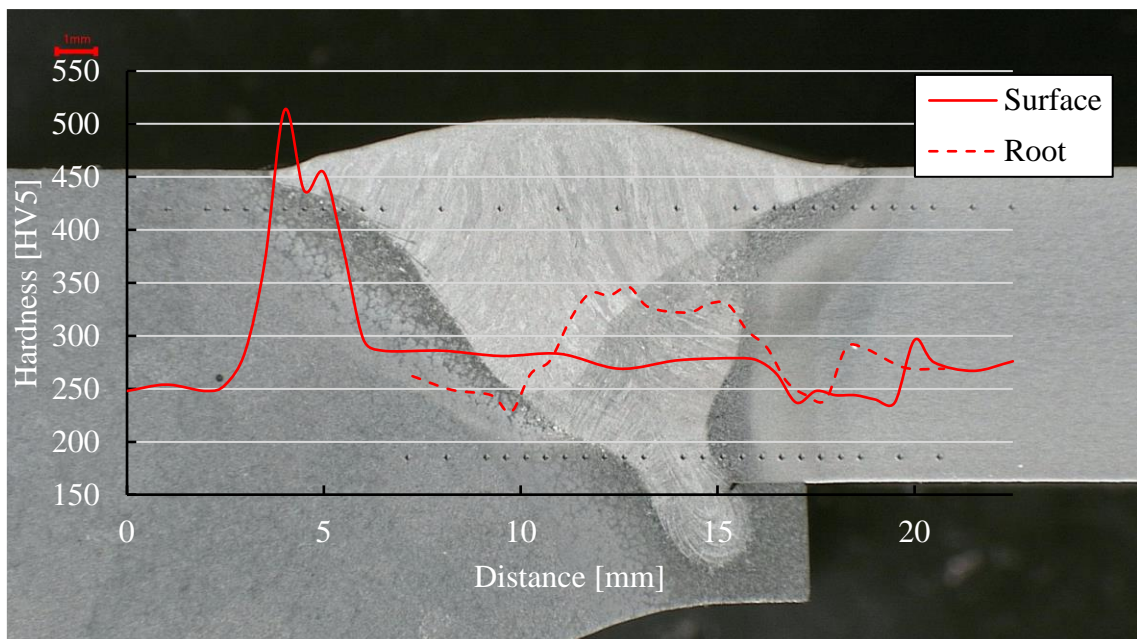

Hardness curves from 35G26_S1 specimen.
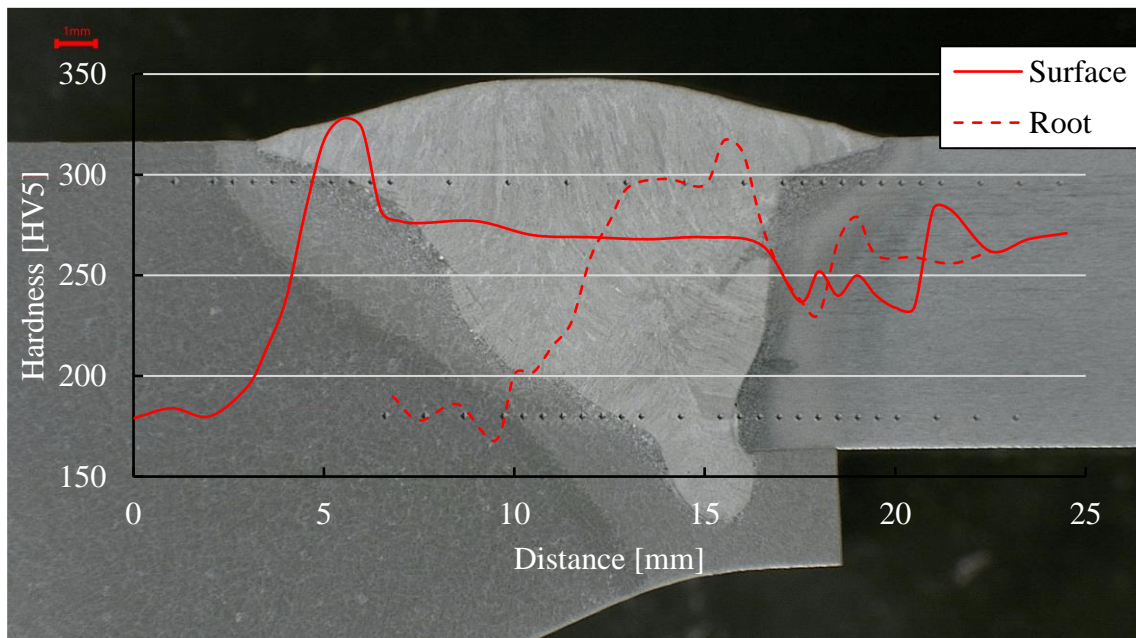
Hardness curves from 70G20_S1 specimen.

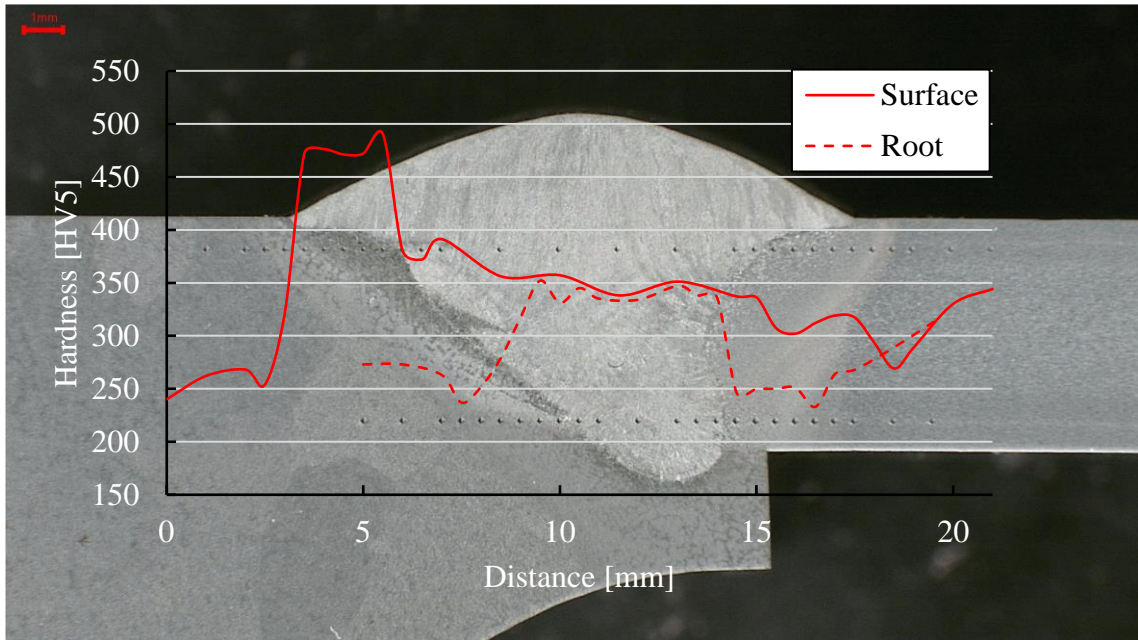Appendix IV: Hardness measurements from quasi-static tensile test specimens
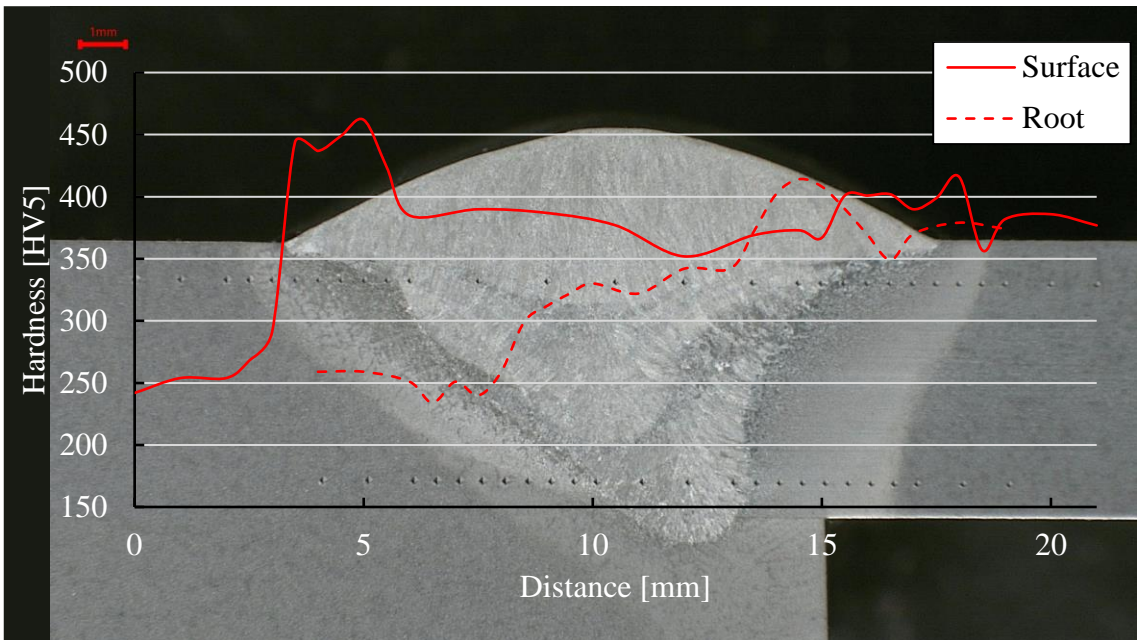

Hardness curves from 70G20_S2 specimen.

Hardness curves from 70G26_S1 specimen.

Appendix IV: Hardness measurements from quasi-static tensile test specimens
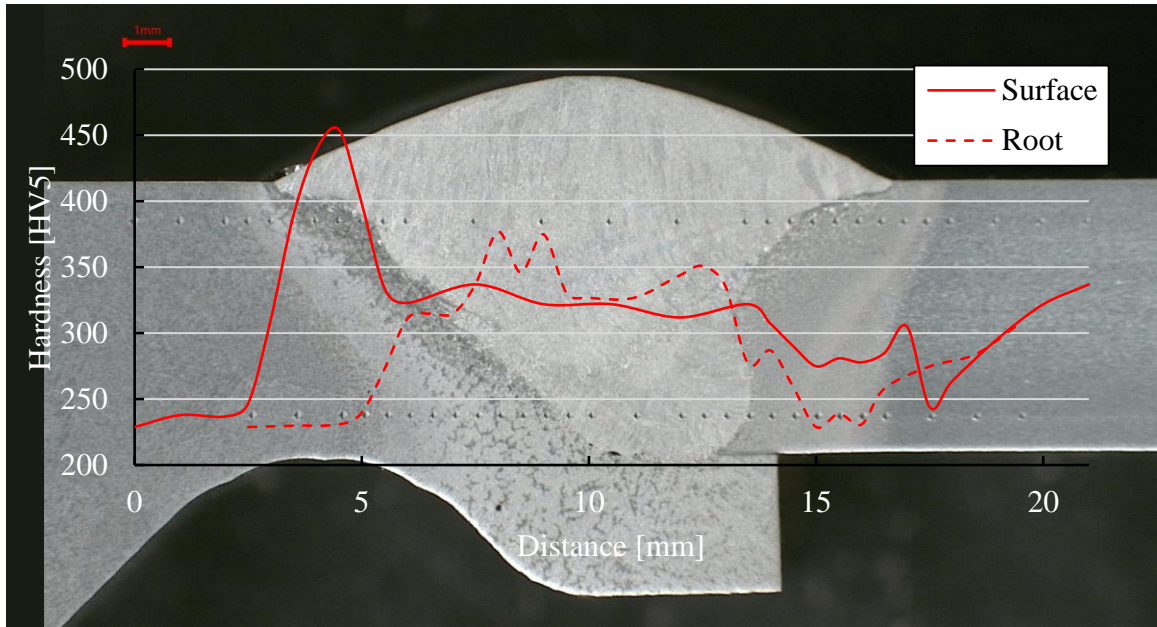

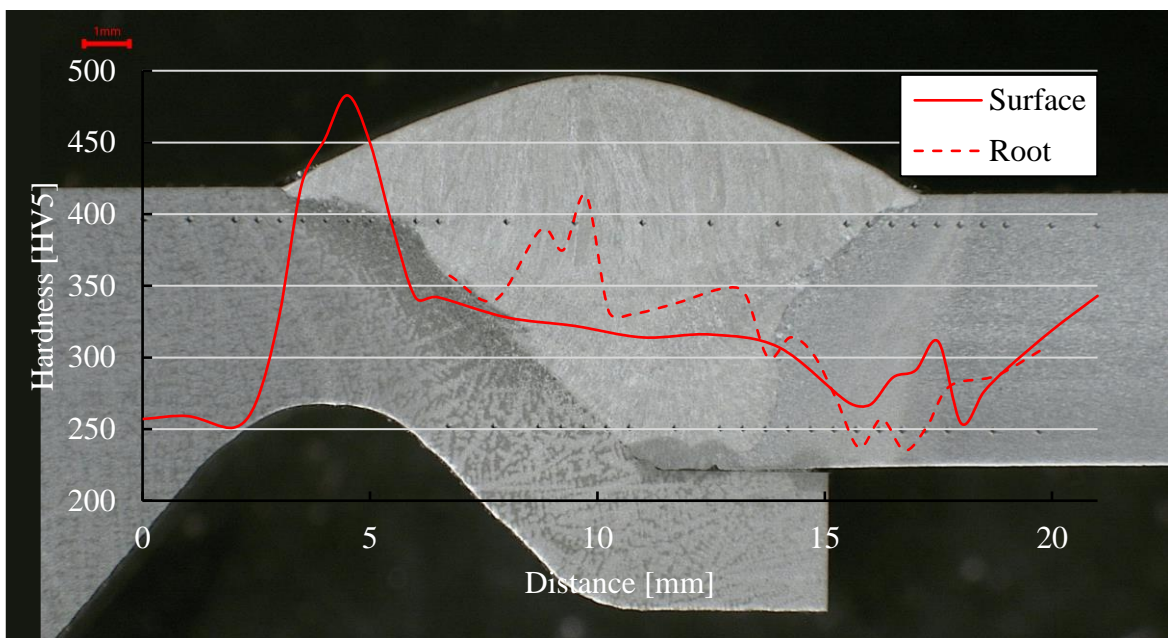Hardness curves from 96G26_S1 specimen.

Hardness curves from 11G26_S1 specimen.

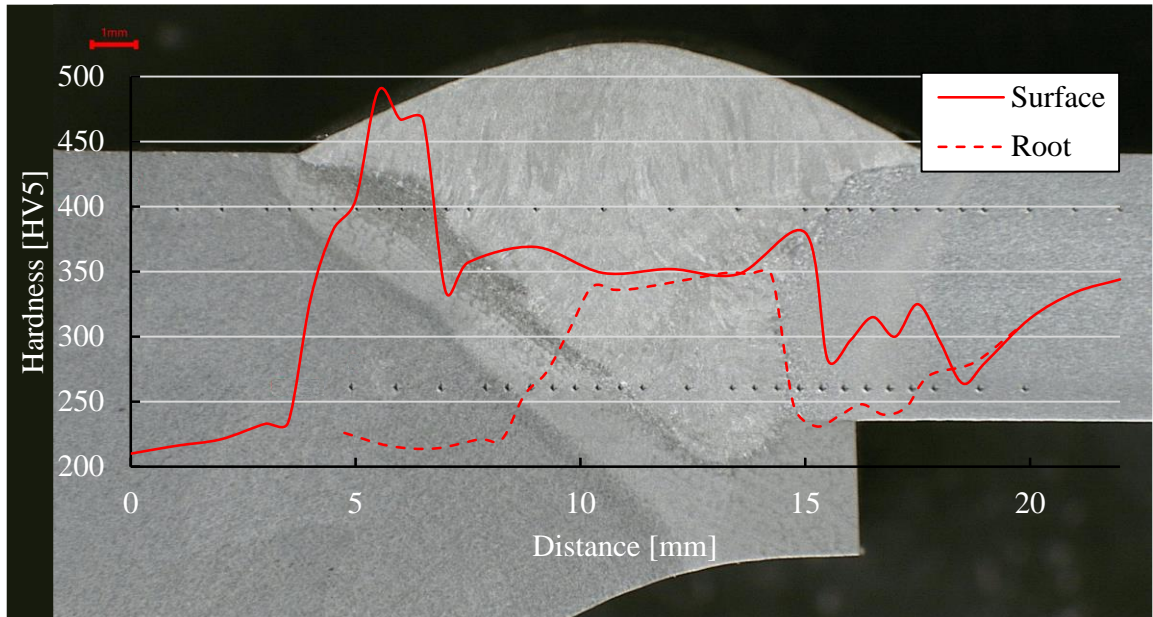Appendix V: Hardness measurements from fatigue test series
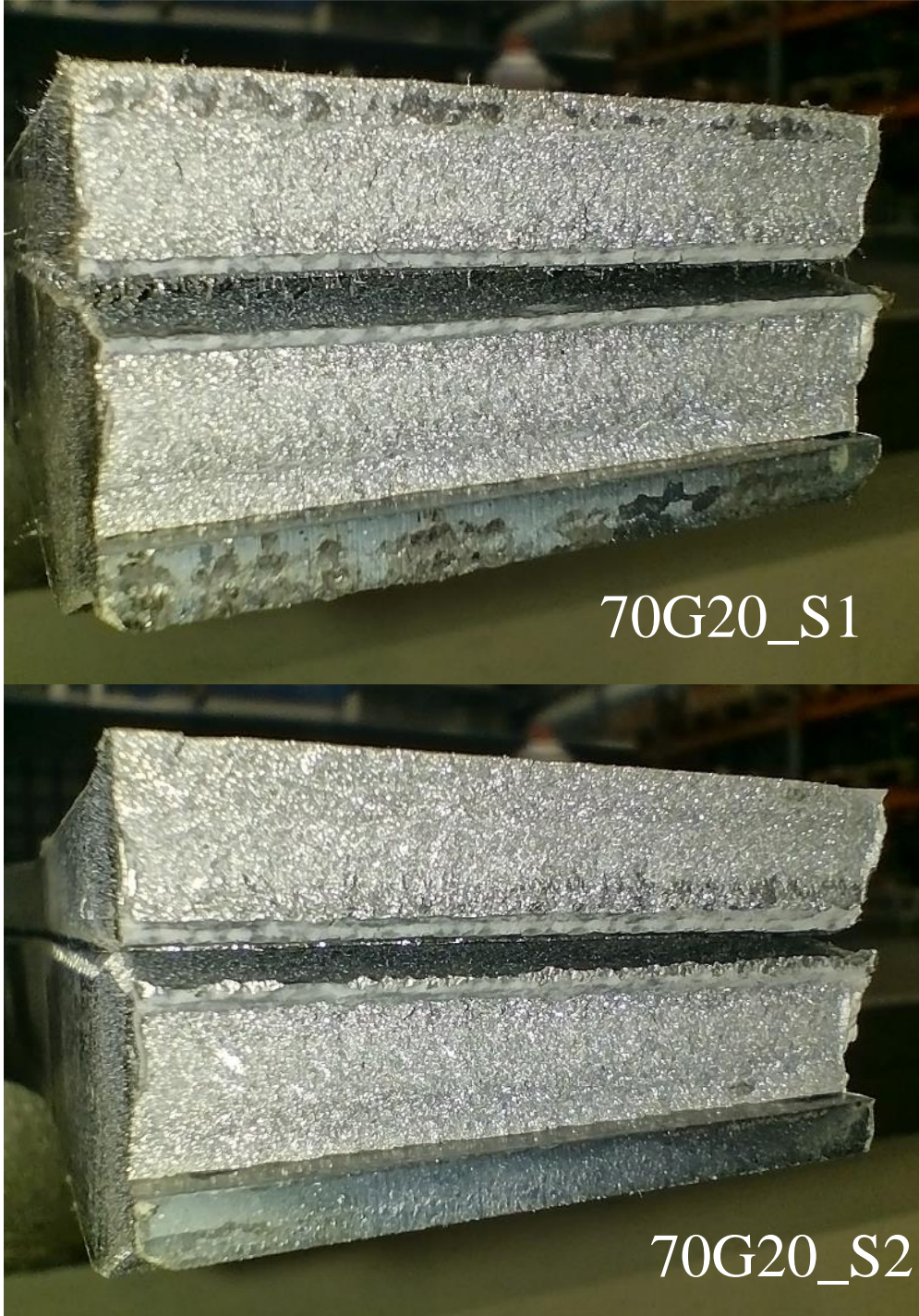

Hardness curves from 96G26_FA1 specimen.

Hardness curves from 96G26_FB2 specimen.

Appendix V: Hardness measurements from fatigue test series

Hardness curves from 96G26_FC1 specimen.

Appendix VI: Fracture surfaces of the 70G20_S1 and 70G20_S2

70G20_S1

70G20_S2

Appendix VII: Numerical values of the FEM notch optimization

| Reference Figure | ID. in the Figure | Fictitious radius [mm] | Position of the groove | | $K_{t,\mathrm{n}}$ | $K_{t,\mathrm{m}}$ | $K_{t,\mathrm{b}}$ |
			x [mm]	y [mm]			
Figure 35	Ctrl	Fillet $\rho_f = 1$	-	-	0	2.1757	1.7286
	F1	Fillet $\rho_f = 1$	-4.5	-2	2.0642	1.8994	1.5613
	F2	Fillet $\rho_f = 1$	-5.5	-2	2.2253	1.9111	1.5729
	F3	Fillet $\rho_f = 1$	-6.5	-2	2.3631	1.9333	1.5887
	F4	Fillet $\rho_f = 1$	-7.5	-2	2.4738	1.9592	1.605
	F5	Fillet $\rho_f = 1$	-4.5	-1	2.9389	1.6324	1.4009
	F6	Fillet $\rho_f = 1$	-5.5	-1	3.0559	1.7097	1.4613
	F7	Fillet $\rho_f = 1$	-6.5	-1	3.1617	1.7764	1.5102
	F8	Fillet $\rho_f = 1$	-7.5	-1	3.2485	1.8329	1.5491
	F9	Fillet $\rho_f = 1$	-4.5	0	4.07	1.2482	1.161
Figure 36	Ctrl	Keyhole $\rho_f = 1$	-	-	0	3.5786	2.5515
	K1	Keyhole $\rho_f = 1$	-4.5	-2	1.8734	3.5043	2.5302
	K2	Keyhole $\rho_f = 1$	-4.5	-1	2.771	3.3833	2.4806
	K3	Keyhole $\rho_f = 1$	-5.5	-1	2.9526	3.3974	2.491
	K4	Keyhole $\rho_f = 1$	-6.5	-1	3.0781	3.4174	2.5033
	K5	Keyhole $\rho_f = 1$	-4.5	0	3.9468	3.1672	2.3927
	K6	Keyhole $\rho_f = 1$	-4.5	1	5.4845	2.8545	2.2395
Figure 37	Ctrl	U-notch $\rho_f = 0.05$	-	-	0	7.1337	5.9165
	U1	U-notch $\rho_f = 0.05$	-4.5	-2	2.1006	5.6035	4.751
	U2	U-notch $\rho_f = 0.05$	-4.5	-1	2.9511	4.4257	3.9794
	U3	U-notch $\rho_f = 0.05$	-5.5	-1	3.0705	4.775	4.3014
	U4	U-notch $\rho_f = 0.05$	-4.5	0	4.0413	3.1008	3.0906
	U5	U-notch $\rho_f = 0.05$	-5.5	0	4.1204	3.7611	3.6496
	U6	U-notch $\rho_f = 0.05$	-5.5	1	5.5104	2.7921	3.0442
	U7	U-notch $\rho_f = 0.05$	-4.5	1	5.5163	1.9324	2.2832
Figure 39	Ctrl	U-notch $\rho_f = 0.05$	-	-	0	5.2916	7.0609
	1	U-notch $\rho_f = 0.05$	-4	-2	1.0947	5.1164	5.2496
	2	U-notch $\rho_f = 0.05$	-4.5	-2	1.1316	5.1351	5.3077
	3	U-notch $\rho_f = 0.05$	-4	-1.5	1.5418	4.7163	4.7237
	4	U-notch $\rho_f = 0.05$	-4.5	-1.5	1.5723	4.7919	4.855
	5	U-notch $\rho_f = 0.05$	-4	-1	2.0698	4.181	4.1209
	6	U-notch $\rho_f = 0.05$	-4.5	-1	2.0879	4.3375	4.343
	7	U-notch $\rho_f = 0.05$	-4	0	3.4006	2.8393	2.8924

Appendix VII: Numerical values of the FEM notch optimization

Reference Figure	ID. in the Figure	Fictitious radius [mm]	Position of the groove		$K_{t,n}$	$K_{t,m}$	$K_{t,b}$
			x [mm]	y [mm]			
Figure 41	1	U-notch $\rho_f = 0.05$	-4	-1	2.0698	4.181	4.1209
	2	U-notch $\rho_f = 0.05$	-	-	1.5495	4.2584	4.2414
	3	U-notch $\rho_f = 0.05$	-	-	1.5767	4.5244	4.8623
	4	U-notch $\rho_f = 0.05$	-	-	1.4082	4.2602	4.2562
	5	U-notch $\rho_f = 0.05$	-	-	1.3787	4.4856	4.5206
	6	U-notch $\rho_f = 0.05$	-	-	1.3339	4.3237	4.2967

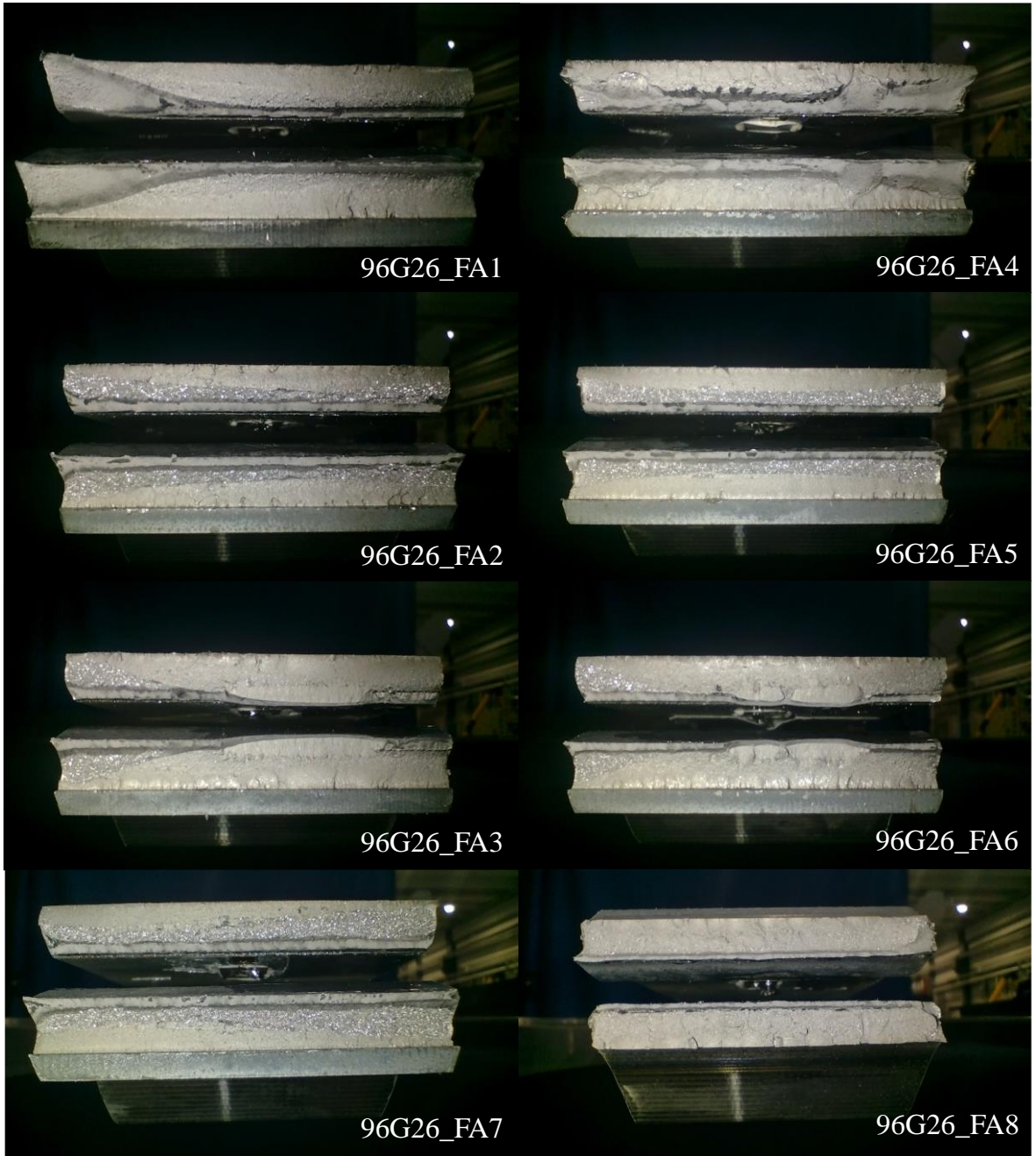Appendix VIII: Optimized geometry of the weld root relief groove
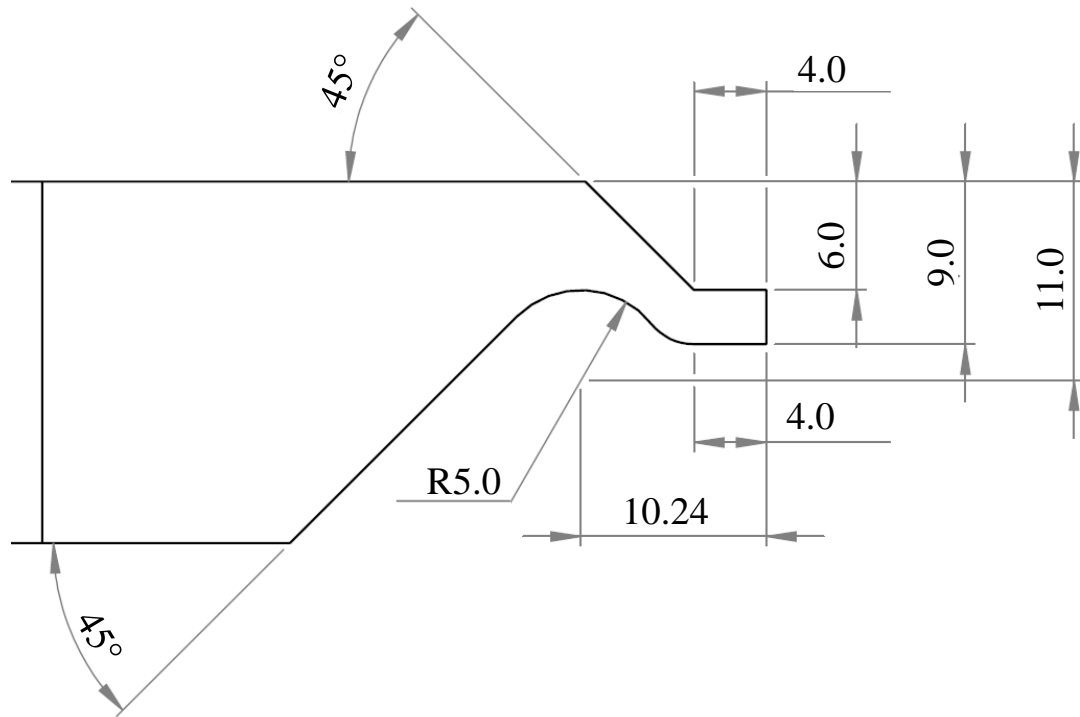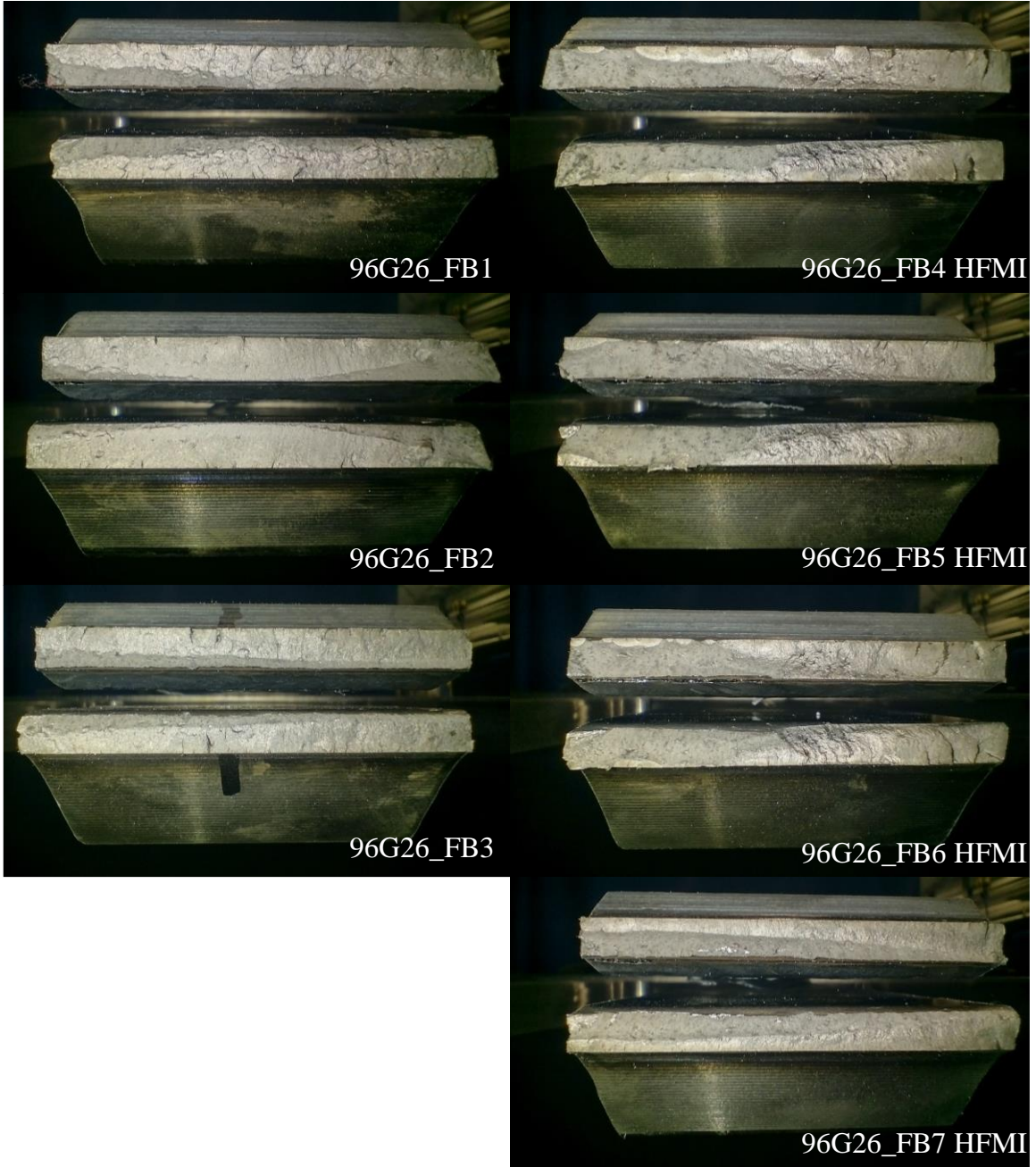
Appendix IX: Fatigue test results

Test ID	Condition	R	ΔF [kN]	DOB	$\Delta\sigma_{nom,plate}$ [MPa]	$\Delta\sigma_{hs,root}$ [MPa]	$\Delta\sigma_{hs,groove}$ [MPA]	Nf [cycles]	Frequency [Hz]	Location of the failure
35G26_FD1	AW	0.1	175.5	0	175.5	175.5	-	371218	100.4	Weld root
35G26_FD2	AW	0.1	157.5	0	157.5	157.5	-	508513	100.1	Weld root
35G26_FD3	AW	0.1	207	0	207	207	-	169600	100	Weld root
35G26_FD4	AW	0.1	189	0	189	189	-	333576	100.1	Weld root
96G26_FA1*	AW	0.1	90	0.352	300	462.85	462.85	39180	0.8	Weld root
96G26_FA2	AW	0.1	135	0.316	450	658.17	658.17	7117	0.5	Weld root
96G26_FA3	AW	0.1	54	0.388	180	293.92	293.92	131925	-	Weld root
96G26_FA4	AW	0.1	135	0.317	450	659.07	659.07	5762	0.6	Weld root
96G26_FA5	AW	0.1	90	0.371	300	476.99	476.99	14944	0.7	Weld root
96G26_FA6	AW	0.1	54	0.373	180	286.93	286.93	75326	0.7	Weld root
96G26_FA7	AW	0.5	54	0.338	180	271.99	271.99	82126	0.9	Weld root
96G26_FA8	AW	0.5	72	0.319	240	352.52	352.52	41281	0.7	Groove
96G26_FB1	AW	0.1	72	0.227	240	310.46	445.26	17472	0.7	Groove
96G26_FB2	AW	0.1	45	0.281	150	208.55	304.10	124019	0.8	Groove
96G26_FB3	AW	0.1	54	0.262	180	243.81	335.45	47281	0.8	Groove
96G26_FB4	HFMI	0.1	72	0.100	240	266.69	367.44	130633	0.7	Groove
96G26_FB5	HFMI	0.1	81	0.150	270	317.78	444.94	54100	0.7	Groove
96G26_FB6	HFMI	0.1	76.5	0.188	255	313.92	444.75	63394	0.6	Groove
96G26_FB7	HFMI	0.1	85.5	0.211	285	361.04	515.17	26782	0.6	Groove
96G26_FC1	AW	0.1	90	0.438	300	534.17	-	16700	0.7	Weld root
96G26_FC2	AW	0.1	135	0.431	450	791.5	-	3523	0.5	Weld root
96G26_FC3	AW	0.1	54	0.467	180	337.87	-	36534	0.9	Weld root
96G26_FC4	AW	0.1	40	0.443	133.33	239.41	-	97857	0.9	Weld root
96G26_FC5	AW	0.1	90	0.46	300	555.18	-	12130	0.7	Weld root
96G26_FC6	AW	0.1	54	0.458	180	332.05	-	56905	0.9	Weld root
96G26_FC7	AW	0.5	54	0.454	180	329.48	-	43536	0.8	Weld root
96G26_FC8	AW	0.5	72	0.441	240	429.69	-	22720	0.7	Weld root

*Overload case

Appendix X: Fatigue specimen's fracture surfaces

96G26_FA1

96G26_FA4

96G26_FA2

96G26_FA5

96G26_FA3

96G26_FA6

96G26_FA7

96G26_FA8

Appendix X: Fatigue specimen's fracture surfaces

96G26_FB1

96G26_FB4 HFMI

96G26_FB2

96G26_FB5 HFMI

96G26_FB3

96G26_FB6 HFMI

96G26_FB7 HFMI

Appendix X: Fatigue specimen's fracture surfaces

96G26_FC1

96G26_FC4

96G26_FC2

96G26_FC5

96G26_FC3

96G26_FC6

96G26_FC7

96G26_FC8

Appendix X: Fatigue specimen's fracture surfaces

35G26_FD2
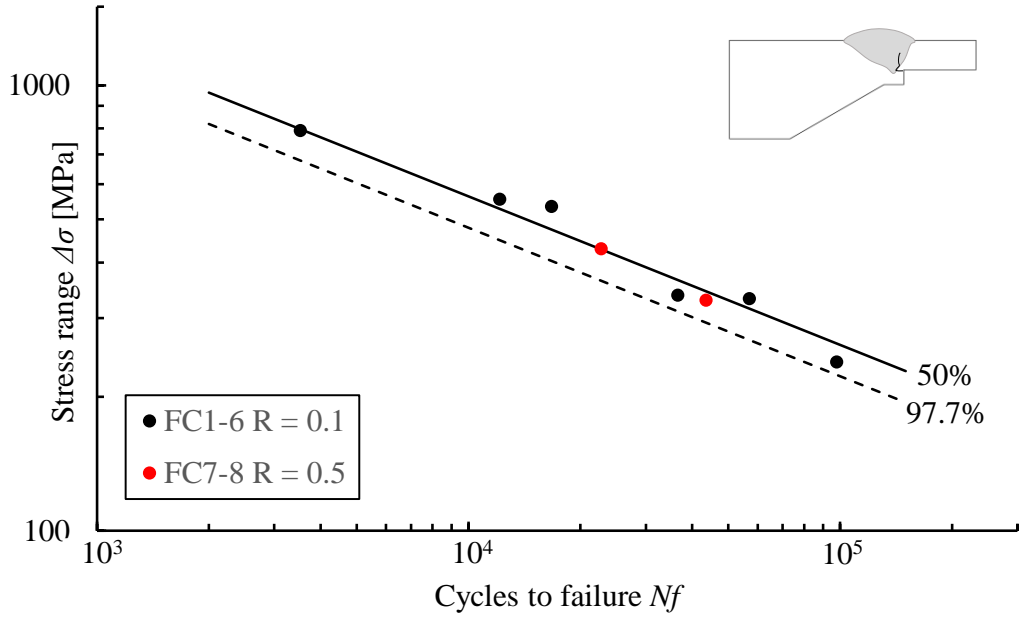
35G26_FD3

35G26_FD4
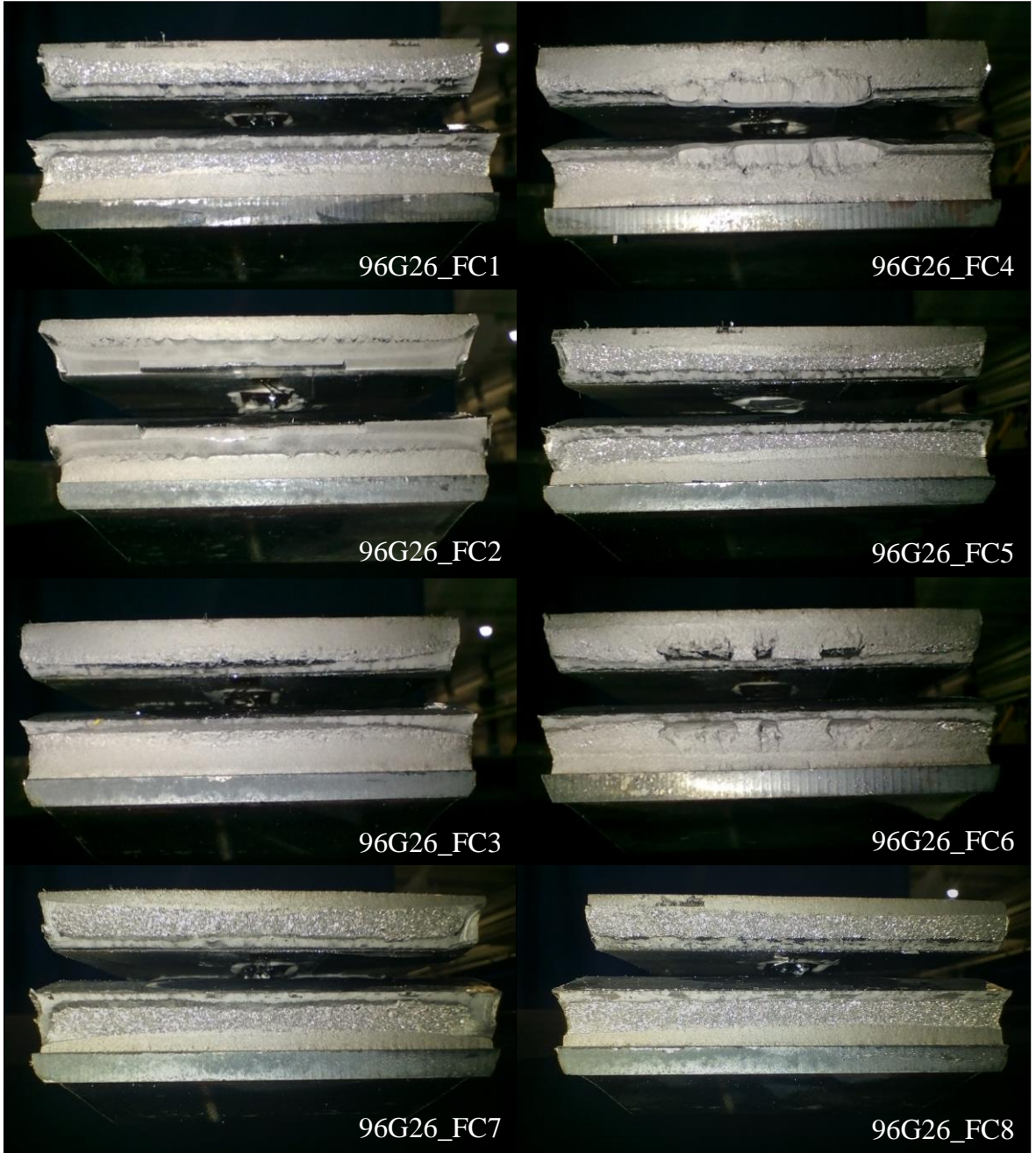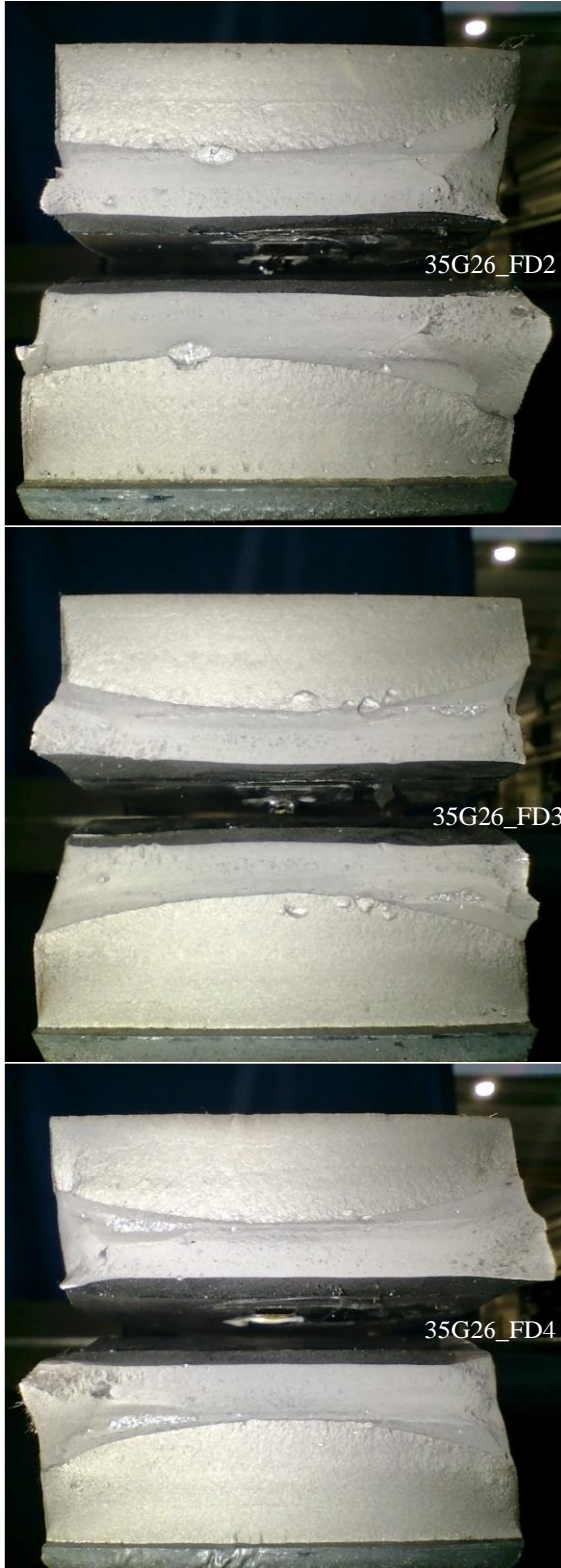
Appendix XI: Graphs from each individual fatigue test series and fitted curves
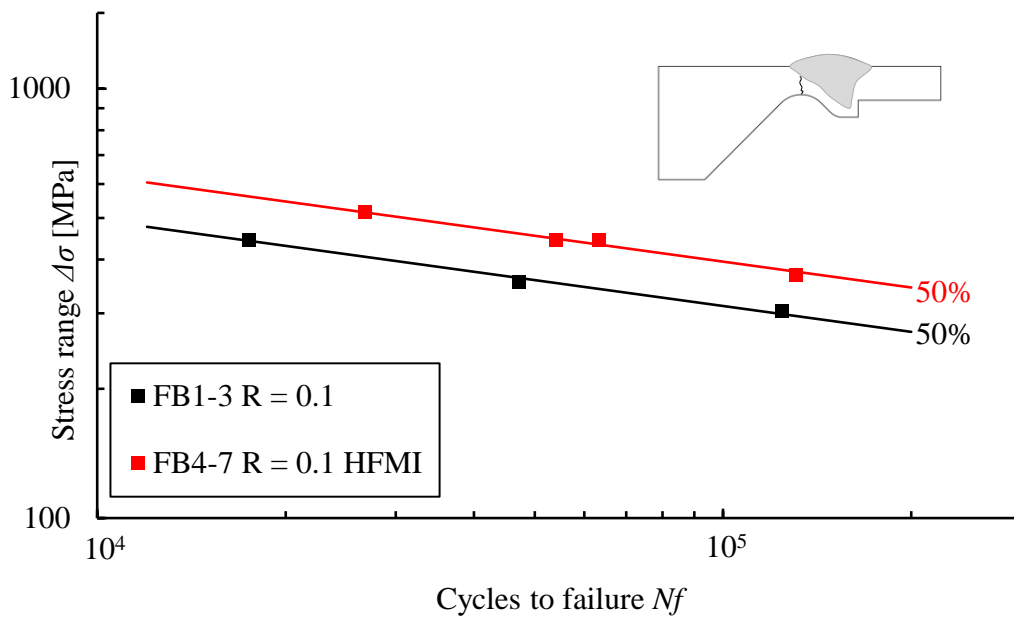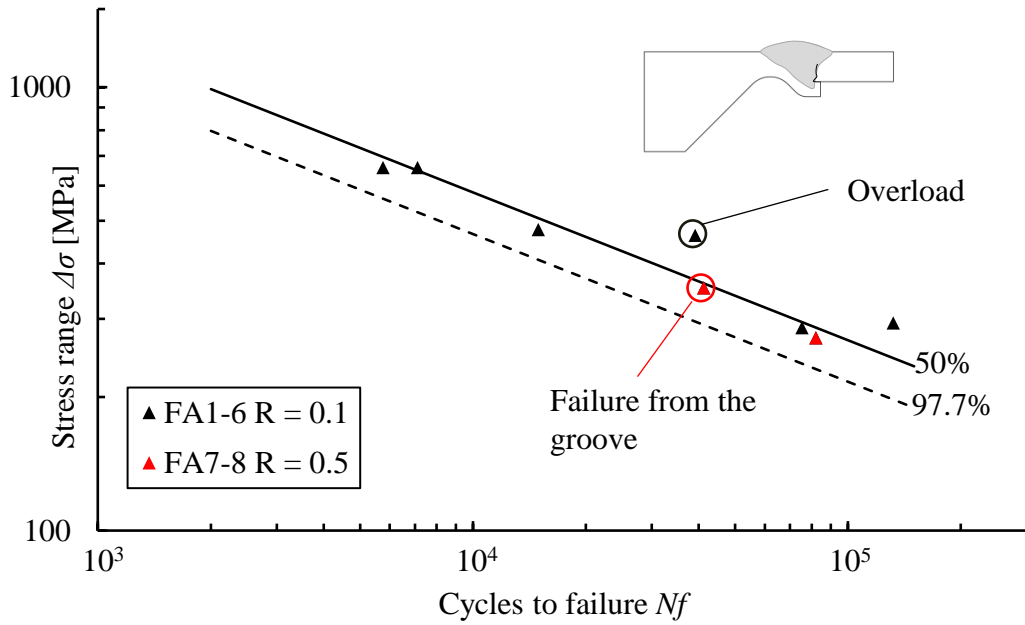
Appendix XI: Graphs from each individual fatigue test series and fitted curves
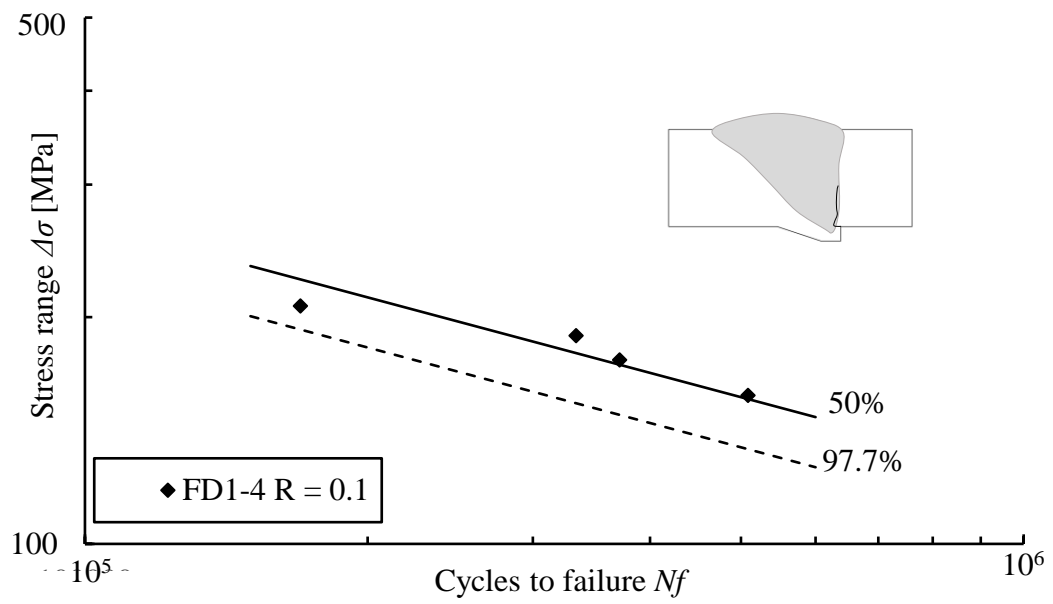
Appendix XII: Graph with every successful fatigue specimen with S-N curves.